

Retention and Release of *Banksia* Seeds

Functionalization of Plant Fibers in a Matter of Reproduction

vorgelegt von
M. Sc.
Friedrich Johannes Reppe

an der Fakultät III – Prozesswissenschaften
der Technischen Universität Berlin
zur Erlangung des akademischen Grades

Doktor der Naturwissenschaften
– Dr. rer. nat. –

genehmigte Dissertation

Promotionsausschuss:

Vorsitzender	Prof. Dr.–Ing. Dietmar Auhl
Gutachterin	Prof. Dr.–Ing. Claudia Fleck
Gutachter	Prof. Dr. Dr.hc Peter Fratzl
Gutachterin	Dr. Michaela Eder

Tag der wissenschaftlichen Aussprache: 13. Dezember 2021

Berlin 2022

“More than cleverness we need kindness and gentleness”

— Charles Spencer Chaplin

Acknowledgments and Preface

Throughout the preparation of this dissertation, I received a lot of support that I am grateful for. I would like to thank my direct supervisor, Dr. Michaela Eder, who inspired and challenged me commensurately. Her passion for plant research, her candor, and her trust pushed me forward and motivated me. Moreover, I want to thank Prof. Dr. Dr.hc Peter Fratzl for his guidance, for many valuable thoughts, and not least for the excellent research atmosphere he promotes in his department. I am also thankful for Prof. Dr.-Ing. Claudia Fleck's supervision of this work and the large freedom she made possible.

I especially appreciate the experimental support and the intense discussions with Prof. Rivka Elbaum, who hosted me in her lab in Rehovot, Dr. Peter Werner, who performed the TEM measurements and gave many helpful advices, Klaus Bienert, who helped me to develop the conditioned tensile experiment, Dr. Clemens Schmitt, who gave me useful hints for the Raman evaluation, and Petra Leibner, who supported me with the micromechanical experiments. Moreover, I am thankful for all the other assistance I received at the Max Planck Institute of Colloids and Interfaces.

I am grateful to my friends, who supported me and cheered me up. Together we share glamorous moments, and we survived a worldwide health crises. I acknowledge the support of Lukas, Maria, Nina, Sinja, Trez, and Zack, who eliminated many typing errors. Finally, I would like to thank my family—my parents, who always supported me and were confident about my way, and also my sister and her family—a source of happiness.

The present work is part of an ongoing project in the group “Adaptive Fibrous Materials” at the Max Planck Institute of Colloids and Interfaces and the excellence cluster Matters of Activity. The funding of the project is highly appreciated. Preliminary tests on the hygroscopic behavior and the tensile stiffness of the *B. attenuata* pericarp were already carried out for the author's Master thesis in 2017. The here presented extensive experiments on composition, structure, and mechanics of the pericarp were exclusively performed in the context of the present dissertation.

Abstract

Plants of the Australian *Banksia* genus can retain mature seeds for more than a decade and release them after bushfire and rain. Their mechanism of reproduction evolved according to the conditions of their habitats: nutrient-poor soils and Mediterranean climate with hot summers, seasonal rainfalls, and frequently occurring bushfires. Despite the hostile environment, life in these regions is highly diverse and so are the strategies plants developed to prevail in evolution. The seed dispersal of *Banksia* is only one out of many fascinating examples.

Throughout the long-term seed retention, *Banksia's* seed pods (“follicles”) ensure stability and protectiveness. At the same time, they maintain their motion potential for the delayed seed release after a heat trigger and subsequent rainfall. The cause for these contrary properties, stability and movability, lies in the material of the follicle valves (“pericarp”) itself, as the infructescence remains without metabolism on the plant after maturation. The present work reveals sophisticated interactions between chemical composition, structure, and physical properties of the pericarp layers, based on detailed histological, spectroscopic, microscopic, and micro-mechanical investigation.

The thick middle layer of the pericarp, the “mesocarp”, shows a continuous cellulose tilt angle perpendicular to the longitudinal fiber axis, which leads to remarkable swelling and shrinkage upon wetting and drying. A gradient in lignification causes more pronounced dimensional changes towards the outside of the follicle. Shrinkage of the mesocarp fibers upon maturation is restrained in closed follicles by the sealed junction of the pericarp valves, by the stiffness of the endocarp, and possibly by the resistance of the brittle yet hard exocarp. In consequence, mesocarp fibers develop drying stresses, as measured by a newly designed experimental setup. These stresses increase further when heat-dried. During the first fire-triggered opening step of the seed pods, the largest proportion of the mesocarp shrinkage potential is still retained. Subsequent wetting leads to pronounced swelling, while stiffness and hardness of the follicle tissue diminish to a larger extent than for wood fibers of trees. This “flexibilization” and “softening” increases towards outer mesocarp regions. In comparison, dry mesocarp shows homogeneous mechanical properties over the layer thickness. Alternation of wetting states, of the related mechanical properties, and of the hygroscopic deformation in accumulating moistening cycles increases the drying shrinkage of the mesocarp against the resistant endocarp. It leads to progressing deflection of the follicle valves for seed release.

Gradual transitions of chemical composition in the mesocarp and variable cellulose tilt angles in the endocarp cause successive changes of the physical behavior over the thicknesses of the layers. On the opposed edges of meso- and endocarp high deformability or high stiffness is reached, respectively. At the same time, stresses towards the interface of the layers are reduced, so the valves remain intact throughout bending. Based on the measurements, a comprehensive picture can be drawn of the principles underlying the *Banksia* seed retention and release. The insights can moreover serve as an inspiration for biomimetic applications, requiring both motion and long-term stability.

Zusammenfassung

Australische *Banksia* Arten können reife Samen für mehr als zehn Jahre zurückbehalten. Erst in der Hitze eines Buschbrandes öffnen sich die Samenkapseln („Follikel“); nachfolgende Regenfälle führen zur Samenfreisetzung. Die Fortpflanzungsstrategie der *Banksia* ist auf die Umgebungsbedingungen der Pflanzen angepasst: Die Böden ihrer Habitate sind nährstoffarm und das mediterrane Klima dieser Gebiete ist von heißen Sommern, saisonaler Wasserverfügbarkeit und regelmäßigen Buschbränden geprägt.

Diese unwirtlichen Erdregionen zeichnen sich durch eine erstaunliche Artenvielfalt mit zahlreichen faszinierenden Überlebensstrategien aus. *Banksias* Fortpflanzungsmechanismus ist eines dieser Beispiele. Während die Follikel über Jahre hinweg den Schutz der Samen gewährleisten, erhalten sie ihren Öffnungsmechanismus ohne jeglichen Metabolismus der Pflanze aufrecht. Sowohl die Stabilität als auch ihre Bewegungsfunktion für die Samenfreisetzung beruhen allein auf den Materialeigenschaften der Follikelhälften („Perikarp“). Diese Eigenschaften werden in der vorliegenden Arbeit anhand detaillierter histologischer, spektroskopischer, mikroskopischer und mikromechanischer Methoden untersucht. Die Ergebnisse offenbaren den Wirkmechanismus hinter der Follikelöffnung: Eine komplexe Interaktion zwischen chemischer Zusammensetzung, Zellwandstruktur und physikalischen Eigenschaften der Perikarp-Schichten.

Im Mesokarp, der dominanten mittleren Schicht des Perikarps, ist die Cellulose gleichmäßig quer zur Längsachse der Fasern orientiert. Dieses Strukturmerkmal verursacht eine deutliche hygroskopische Verformung. Zur Außenseite des Mesokarps

nimmt die Lignifizierung des Gewebes ab, während Quell- und Schwindverhalten zunehmen. In geschlossenen Follikeln ist diese Trocknungsverformung eingeschränkt. Die versiegelte Verbindungszone der Perikarp-Hälften, das steife Endokarp und möglicherweise auch das spröde und harte Exokarp wirken der Verformung entgegen. Es entstehen Trocknungsspannungen, die in einem neu entwickelten Experiment anhand von Einzelfasern präzise bestimmt werden konnten.

Eine anschließende Benetzung führt zur Quellung der Fasern und senkt ihre Steifigkeit und Härte weiter herab, als es für Holzfasern der Bäume bekannt ist. Besonders die äußeren Mesokarp-Faserbündel sind von dieser „Flexibilisierung“ und „Erweichung“ betroffen. Im trockenen Zustand dagegen sind die mechanischen Eigenschaften über die Dicke des Mesokarps hinweg konstant. Zyklische Wechsel der Benetzungszustände und der entsprechenden Materialeigenschaften führen im zweiten Öffnungsschritt der Follikel zu fortschreitendem Mesokarp-Schwund gegen das resistente Endokarp. Diese Deformation bewirkt die Auslenkung der Perikarp-Hälften und führt schließlich zur Samenfreisetzung.

Graduelle Wechsel der chemischen Zusammensetzung bzw. der Celluloseorientierung führen zu Veränderungen des Materialverhaltens innerhalb des Mesokarps und des Endokarps. An den entgegengesetzten Kanten der Schichten herrschen einerseits hohe Verformbarkeit, andererseits hohe Steifigkeit vor. Gleichzeitig werden Spannungen am Übergang der Schichten vermindert, sodass die Follikelhälften auch bei Biegung intakt bleiben. Auf Grundlage umfangreicher Experimente können die Prinzipien hinter der Samenrückhaltung und -freisetzung von *Banksia* schlüssig erklärt werden. Die gewonnenen Erkenntnisse können außerdem als Ausgangspunkt für biomimetische Anwendungen dienen, die sowohl Beweglichkeit als auch Langzeitbeständigkeit erfordern.

Contents

1	Introduction	1
1.1	Background and Motivation	1
1.2	Objective and Outline	3
2	State of Research	4
2.1	Environment and Biology of <i>Banksia</i>	4
2.2	Plant Cell Walls in Relation to <i>Banksia</i> Serotiny	7
2.2.1	Components and Structure of Plant Cell Walls	7
2.2.2	Interaction Between Cell Wall and Water	9
2.3	Follicle Anatomy and Opening of <i>B. attenuata</i>	10
2.4	Experimental Background	12
2.4.1	Histology	13
2.4.2	Raman Microspectroscopy	13
2.4.3	Polarized Light Microscopy / LC-PolScope	14
2.4.4	Transmission Electron Microscopy	15
2.4.5	Determination of Hygroscopic Deformation	16
2.4.6	Tensile Test	16
2.4.7	Nanoindentation	17
3	Material and Methods	18
3.1	Origin of the Sample Material	18
3.2	Compositional and Ultrastructural Investigations	18
3.2.1	Histology	18
3.2.2	Raman Microspectroscopy	19
3.2.3	Polarized Light Microscopy / LC-PolScope	20
3.2.4	Transmission Electron Microscopy	20
3.3	Physical Tests	21
3.3.1	Hygroscopic Behavior	21
3.3.2	Tensile Test of Tissue Strips	22
3.3.3	Nanoindentation	24
3.4	Novel Experiment to Determine Fiber Contraction Forces	25
3.4.1	Requirements for Precise Fiber Tests in Variable Climate	25
3.4.2	Sample Holders and Fiber Specimens	26
3.4.3	Precision Enhancement of the Tensile Test Stage	27
3.4.4	Assembly for Fiber Wetting	29
3.4.5	Experimental Sequence	30

3.4.6	Test of <i>P. abies</i> Fibers for the Assessment of the Setup	33
3.5	Numerical Modeling of a Bilayer System	40
4	Results and Discussion	41
4.1	Chemical Composition and Ultrastructure	41
4.2	Hygromechanical Properties	46
4.2.1	Hygroscopic Deformation	46
4.2.2	Tensile Stiffness	51
4.2.3	Indentation Modulus and Hardness	53
4.2.4	Stress Generation and Strain Recovery	58
4.3	Numerical Modeling of the Pericarp Deformation	62
4.4	Follicle Opening Explained by Pericarp Mechanics	63
5	Conclusion	66
	References	68
	Figures	85
	Tables	86
	Equations	86

Abbreviations

H p-hydroxyphenyl

G guaiacyl

S syringyl

KMnO₄ potassium permanganate

Tris tris(hydroxymethyl)aminomethan

HCl hydrochloric acid

LC-PolScope liquid crystal-based polarizing light microscope

TEM transmission electron microscope

Symbols

r radius of the curvature of the strip

a layer thickness

ε coefficient of expansion

T temperature

h thickness of the strip

E elastic modulus

I initial valve deflection

II complete valve deflection

1 Introduction

1.1 Background and Motivation

Plants are essential for life on earth, still, despite its ubiquitous diversity flora is rather inconspicuous to the human perception.[1–3] Apparently, we perceive plants more as a static background and pay greater attention to vertebrates, manifold in their appearances and motions.[1] Considering the flora immobile, however, is a misconception. Entire plant populations are able to change places over time in favor of new habitats, like after the glaciation of Northern Europe or due to declining water availability during the last three decades in eastern regions of North America.[4–6] Also individually living plants, stationary by nature, show perceivable motions, for example in shoots or leaves.[7] Already in 1880 Charles Darwin dedicated an entire book to the movement of living plant organs.[8] Retrospectively, botanic work of this time shows an increasing awareness for the relation of function and anatomy. Plant cells, the principal (living) building blocks of the entire flora, were newly thought in a mechanical manner, like the construction elements of a building.[9] This understanding promoted a variety of investigations. Plant organ motions gained particular scientific interest at this time and many examples were found in floral reproductive systems.[9–12] Such preferred research on drastic paradigms is common in biology, as their pronounced relations have also a bearing for less drastic ones.[13] One particular focus was laid on the motion of dead plant organs.[10–12] Although many of these investigated mechanisms differed in function and structure, they can be traced back to one fundamental principle: the arrangement of functionalized cells, which deform in layers against each other due to changing water content.[11, 12, 14] These mechanisms and their related organ motions were early found to be specifically evolved to the plants’ environmental conditions [15, 16]

One example for a well investigated plant motion can be found in *Ruellia* L. fruits. *Ruellia* is widely distributed in temperate, subtropical, and tropical habitats of the world and shows an interesting seed dispersal mechanism.[17] The seeds are protected by an outer shell, called the pericarp, which consists of two valves.[18, 19] Upon drying, the valves split explosively due to anisotropic shrinkage between specifically structured pericarp layers and prestressed outgrowths of the seeds.[18] In consequence, the seeds are catapulted into the environment.[18, 20] Their dispersal, however, can be delayed beyond seed maturity, and linked to spontaneous wetting.[18] As water weakens the junction of the valves, the seeds spread in wet conditions—particularly advantageous for germination in dry ecosystems.[15, 18]

Another well described and often mentioned mechanism is the cone opening of some *Pinus* L. species. Pine cone scales show a similar structure–function relationship like the *Ruellia* pericarp. An “active” tissue layer shrinks upon drying against a dimensionally stable “resistance layer”. [21–24] The resulting bending moment causes the scales to flex and leads to seed release. [21–25] Some pines growing in regions of Mediterranean climate inhibit cone opening upon maturation. [26] They store the seeds inside the cones for more than one year for a delayed mass release after a heat trigger, a phenomenon referred to as “serotiny”. [26, 27] It is the result of evolutionary selection in an environment characterized by moist and cold winters, dry and hot summers, and frequent, yet unpredictable bushfires. [28–32] The function behind this mechanism relies upon a high water content in the tissue even after seed maturation, on thicker, insulating scales, and on a higher amount of resin, sealing the scales. [33–37]

Both cases illustrate a plant’s capability for elaborate reproduction strategies, evolved to the environmental conditions of their ecosystems by responsive mechanisms. The background of these mechanisms was investigated in numerous studies through the decades, each era with its specific state of methods and with different approaches. While early investigations focused particularly on fundamental relations, studies became more detailed over the years, as the literature on the *Ruellia* and the *Pinus* seed release shows. Concurrently, hygroscopic layered systems, which cause metabolism–independent motion in various plant examples [38–42], became a fundamental principle in biomimetic engineering and for technical applications on a variety of length scales. At present, biomimetic examples range from the molecular level of light–sensitive micro robots [43] over humidity–sensitive nanocellulose layers [44], anisotropically swellable 3D–printed structures [45] up to the construction level of wood building elements [46].

Compared to the natural examples described above, the current biomimetic approaches include only few aspects of the phenomena found in nature. Namely, they all follow a one–step process, where a single trigger causes a certain response of the structure. Moreover, they mostly achieve deformation by thin layers, even construction elements show a high ratio between length and thickness. [47, 48] Their motion is the result of two combined layers, each responding differently to the trigger. The examples of delayed seed release among *Ruellia* and serotinous pines, which inhibit the immediate response by the link to an initial trigger event, broaden this view. These processes comprise both stability for seed protection, and functionality

for seed release. The causes for these sophisticated strategies lie in structure and composition of the fruit or cone material, however, these principles have not yet been translated into technical application. Certainly, comprehensive insights into the tissue properties used by plants to combine aspects of stability and functionality, could improve biomimetic approaches. Such holistic incorporation of natural paradigms prevailed in evolution can diversify and specify material design.[49]

To understand how nature achieves structures, which are initially stable, but able to move upon environmental triggers, *Banksia* seed pods are interesting objects of research. Like serotinous pines, many *Banksia* species, endemic to Australia, grow in the heath- and shrublands of Mediterranean climate. They are part of astonishing habitats, where more than 15 % of the world’s known vascular plant species are accumulated on less than 3 % of the land area.[28, 32, 50] The elaborated serotiny, which evolved among *Banksia* species in these competitive regions, has been researched for decades, mainly related to plant conservation, but also from a materials science perspective.[51–54]

The pericarp of the *Banksia* seed pods (so-called “follicles”) can ensure stability for more than ten years, not only protecting the seeds, but preserving the inherent function—a sophisticated sequence of motions for a two-step seed release after bushfire and rain.[53, 55] The underlying tissue properties, however, are assumptions based on ultrastructural insights and there is only little information on how the material of the follicle achieves the refined adaptations of the reproductive system to the harsh environment.[52, 54] Detailed knowledge about the mechanical background of this biological phenomenon, however, is relevant for biomimetic approaches comprising long-term stability and functionality. Furthermore, profound understanding of *Banksia*’s seed dispersal strategy in fire-prone regions can contribute to the preservation of the ecosystem in times of climate change.

1.2 Objective and Outline

The material properties of various layers of *Banksia attenuata* follicles will be investigated in detail in the present work. It aims to understand the serotiny of *Banksia*, in particular the follicles’ capability to retain the seeds inside during, and directly after fire. Moreover, it explores the deflection of the thick follicle valves upon water exposure which leads to seed release. This knowledge is not only essential for an explanation of the opening mechanism. It also provides inspiration for the design of thick, autonomously bending structures.

In a first step, the follicle valves will be investigated with regard to compositional and ultrastructural features to gain insights into the tissue arrangement and potential regions of interest. Based on these findings, the physical behavior of the tissue involved in the opening process will be characterized. Particular consideration applies to the interaction between mechanical properties and hygroscopicity, as follicle stability and moisture responsiveness are essential for *Banksia*'s continuation. Experiments and evaluation techniques will be adapted and combined to enable for comparisons on different hierarchical levels, from single fiber layers up to tissue regions. Technical setups will be specifically developed to precisely determine the mechanical response of fibers to changing moistening states.

The findings will be contextualized with the respective follicle opening steps to draw a comprehensive mechanical explanation of the motion sequence leading to retention and release of *Banksia* seeds. The data basis of the investigation will be laid out as a suitable framework for biomimetic modeling of a stable layer structure without fatigue due to internal stresses. Ultimately, such simulations are fundamental for the development of novel materials on a multitude of length scales, incorporating advantageous structure–function relations found in nature.[25, 43, 44, 47, 48, 56, 57]

2 State of Research

2.1 Environment and Biology of *Banksia*

The genus *Banksia* L.F. comprises approx. 170 species, including the former *Dryandra* genus.[50] Their main habitats are close to the coastal regions in eastern Australia and the biodiversity hotspot southwest of Western Australia, where approx. 75 % of all *Banksia* species can be found.[50, 58, 59] While some species only occur in small areas, for example *B. brownii*, others like *B. attenuata* show a wide distribution range: from the south of Western Australia almost up to Shark Bay (approx. 1000 km).[60] Plants of the genus are indeciduous shrubs and trees of moderate height.[59, 61] They normally grow on nutrient poor grounds in regions where rainfalls mainly occur in the colder months of the year.[62, 63] In the dry summers, temperatures frequently exceed 40 °C and periodic bushfires are a natural component of the ecosystem.[61, 63, 64]

During the species–dependent flowering period *Banksia* plants develop conspicuous inflorescences of characteristic shape and color (Fig. 1 A).[55, 61] Floral units of two sessile protandrous flowers are tightly arranged perpendicularly around the

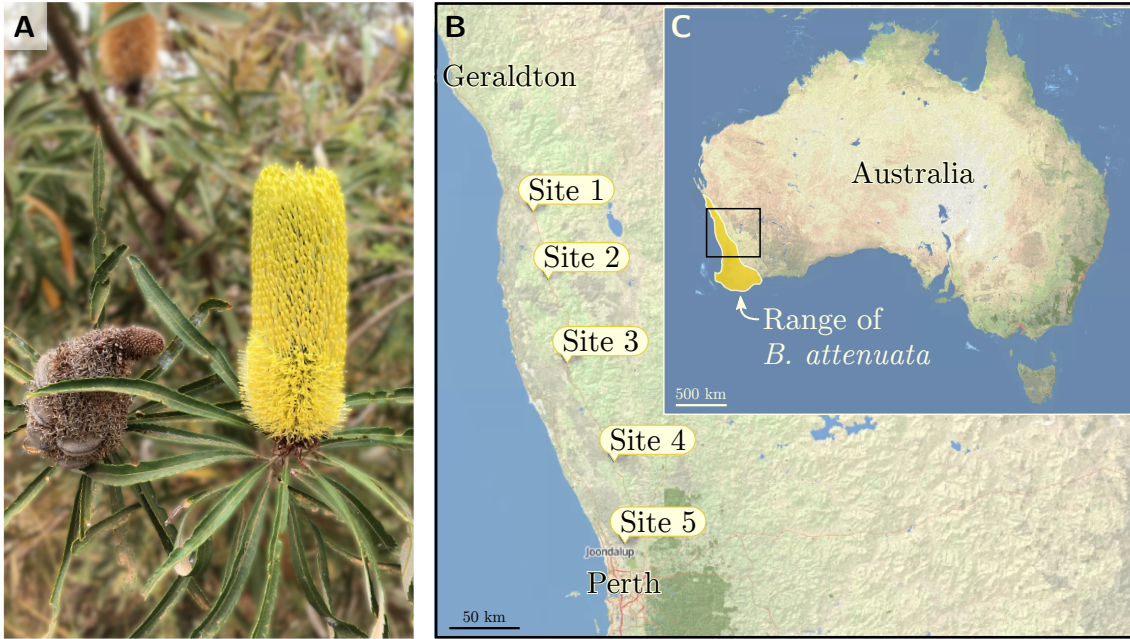


Fig. 1: Specifics of *Banksia attenuata* R.Br. A: inflorescence and infructescence (picture by Michaela Eder). B: sample sites of infructescences [54]. C: distribution range [65]. Map material from <http://umap.openstreetmap.fr>, accessed on 2021-08-21.

rachis; each flower as well as every floral unit is subtended by a floral or a common bract, respectively.[55, 66] After pollination by birds, small mammals, or insects, floral and common bracts elongate and harden while involucral bracts are often deciduous.[55, 61, 66] Only a small number of flowers are pollinated and develop into follicles [55], “dehiscent simple dry fruits”, which are “derived from a single carpel that splits along one side” after the maturation of the seeds.[29] The outer encapsulation of a fruit is called the pericarp.[29] For *Banksia* follicles it consists of two resistant valves which form ahead of the seeds and serve early as a mechanical protection against predators.[55, 67] Within two years, up to two winged seeds mature in the back of the follicle, where the pericarp is embedded in the rachis of the infructescence (Fig. 2 B–D, bottom).[51, 55, 61] They are held in place by a porous separator, which fills the space towards the outer edge of the follicle and has an insulating effect.[51, 55, 68] Enclosing seeds and separator, the pericarp valves converge in a wax-sealed junction zone, more or less asymmetrically, depending on the species.[51, 54, 61, 69] The anatomy of the follicle and the structure of the pericarp will be elaborated upon and illustrated in section 2.3.

In the fire prone bushlands of Australia two fundamental mechanisms ensure the continuation of the *Banksias*. Some species are fire tolerant.[61, 70] Their plants

survive fire events and resprout from resistant stems or underground organs even after excessive heat exposure.[61, 70] Their follicles are dehiscent, seeds are generally released in specific seasons after maturation.[61] In comparison, the plants of fire-killed species do not survive excessive heat exposure.[61, 70] They show the phenomenon of serotiny; the seeds are retained for the delayed release, after a heat trigger initiated the opening process of the follicles.[70] Although the trigger of heat is the same for all serotinous *Banksia* plants, the temperatures required for follicle opening depend on species and growing site [53, 54, 71] The propensity of long-term seed retention increases as plant height decreases in harsh climatic conditions.[53, 54] In cooler and wetter regions some *Banksia* species release several mature seeds spontaneously and retain others for several years on the plant to establish a canopy seed bank.[53, 54] In hotter regions, more seeds are retained for longer periods up to more than a decade and the elevated temperatures of bushfires become an important trigger for follicle opening.[53, 54]

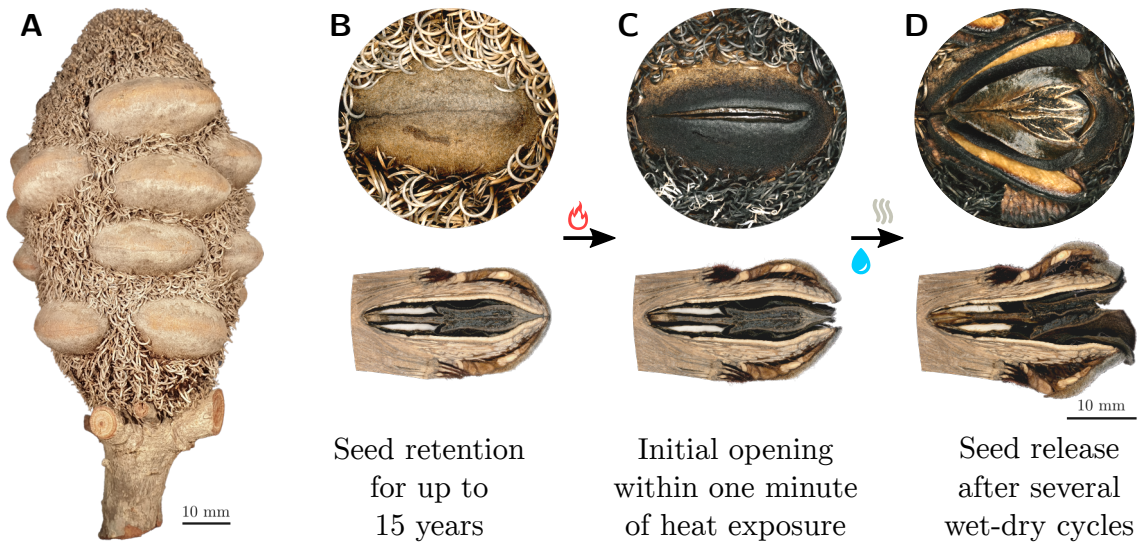


Fig. 2: Reproduction system of *B. attenuata*. A: infructescence with closed follicles. B–D: opening sequence of a follicle from the closed state (B), over the initially opened state after heat exposure (C), to the completely opened follicle after wet-dry cycles (D). Top: front view. Bottom: longitudinal cutting plane, left sides show embedment in the rachis.

This initial opening due to heat, however, is only the first of two steps leading to seed release.[72] Several subsequent cycles of wetting and drying are necessary to deflect the pericarp valves to the extent in which the seeds can fall down onto cold ground.[72] Interestingly, the entire storage period of mature seeds and the opening process of the *Banksia* follicles is independent of the plant's metabolism.[52] The

serotinous reproduction completely relies on a sophisticated arrangement of meso-, micro-, and ultrastructural features, “programmed” into the pericarp material to ensure the species’ survival.[52, 54, 68]

2.2 Plant Cell Walls in Relation to *Banksia* Serotiny

Important structural building blocks of the *Banksia* pericarp are fibrous cells with thick cell wall layers.[52, 73] These fibers show similarities with other plant cells like those found in the stems of trees (xylem), which are well investigated.[7, 74] In the following a brief overview of composition, structure and properties of plant cells is given, with a focus on the thick secondary cell wall layer.

2.2.1 Components and Structure of Plant Cell Walls

Plant cell walls contain large proportions of cellulose, a polysaccharide of 1–4-linked β -D-glucose molecules.[7, 75, 76] These cellulose chains form microfibrils by hydrogen bonds, approx. 2 nm to 3 nm in diameter and approx. 30 nm in length.[7, 75–78] Highly ordered crystalline regions are connected and surrounded by less ordered chains, the amorphous regions of a microfibril.[7] The spaces between crystalline regions, approx. 1 nm large, are sufficient for water molecules to penetrate the cell wall on this level.[79–81]

Several microfibrils agglomerate to form a macrofibril (diameter approx. 20 nm), while the non-cellulosic compounds hemicelluloses and lignin fill the approx. 10 nm large gaps in between as a linking matrix.[7, 79, 82] Hemicelluloses are non-crystalline glycans, which comprise different pentosanes and hexosanes; they form heteropolymeric structures.[7, 75, 76] Hemicellulose chains are much shorter than cellulose, to which they attach closely.[7, 75] After the synthesis and arrangement of the polysaccharides cellulose and hemicelluloses, the second group of matrix compounds—the lignin—is deposited into the interfibrillar spaces.[75, 79] Lignin basically consists of three phenolic compounds (Fig. 3), which are enzymatically synthesized from monosaccharides.[83] When incorporated into the lignin network they build specific units: p-coumaryl alcohol forms p-hydroxyphenyl (H), coniferyl alcohol produces guaiacyl (G), and sinapyl alcohol develops into syringyl (S).[7, 74, 75, 84] The lignin composition out of these principal building blocks is not only different among gymnosperms, lignified angiosperms, and lignified grasses.[7, 75, 76, 85] Variations occur also between and within species, and even for different parts of a single plant.[7, 86–88] Lignin attaches to the hemicelluloses; it is the last component built into the

developing wall of a living cell and leads to cell death at some stage.[7, 74, 76, 79, 89] Due to the rather hydrophobic character of this compound, lignification reduces the hydrophilicity of the polysaccharide structure.[76, 90, 91]

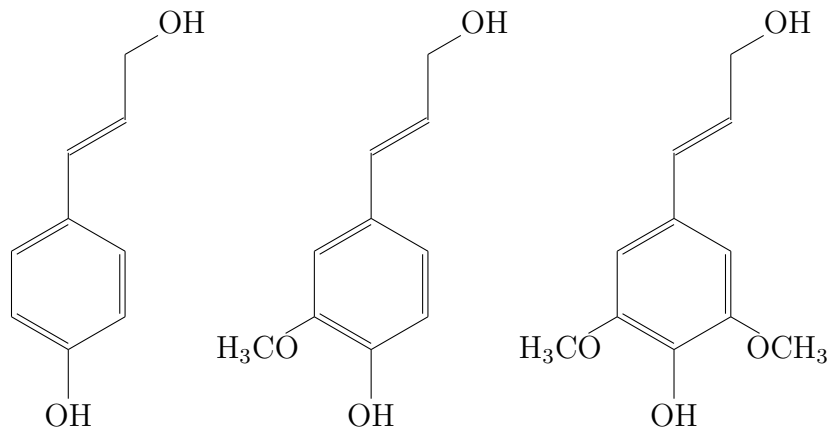


Fig. 3: Structural formulae of the lignin building blocks. Left: p-coumaryl alcohol (basis of H-unit). Middle: coniferyl alcohol (basis of G-unit). Right: sinapyl alcohol (basis of S-unit).[74, 75, 85]

During cell growth several characteristic layers form successively (Fig. 4 A).[7, 74–76] In the beginning, directly after cell division, the protoplast forms a primary wall.[7, 74] It is a thin layer, which stretches as the cell grows.[7, 74] The interspace between individual cells is filled by the middle lamella.[7, 74] As the cell reaches its final shape, primary wall synthesis and growth stop and a thicker secondary wall with two to multiple sub-layers forms.[7, 74, 75] All these cell wall layers are discernible by their chemical composition and by the orientation of the cellulose fibrils.[7, 92] The lignin content decreases from the middle lamella towards the cell lumen, while the share of cellulose increases.[7, 92] The orientation of the cellulose fibrils with regard to the cell longitudinal axis changes between cell wall layers.[7, 74, 75] As shown in Fig. 4 A, B for wood cells (xylem), the microfibrils of primary walls are variedly arranged, while secondary walls show a more parallel cellulose orientation with a distinct tilt angle in each sublayer.[7, 74, 75]

The shape of cells and the thickening of their walls depends on their function.[74] Ground tissue like parenchyma is rarely specialized and can fulfill various functions, like water and nutrient storage or gas exchange, due to the rather simple anisotropic cell shape and thin cell walls.[7, 30] Vascular cells, in comparison, are elongated for the transport of water and nutrients.[7, 30] Consolidation tissue, like fiber-tracheids and sclerenchyma fibers, stabilizes plant organs and develops largely thickened secondary walls to fulfill this function (Fig. 4 A).[7, 30, 74]

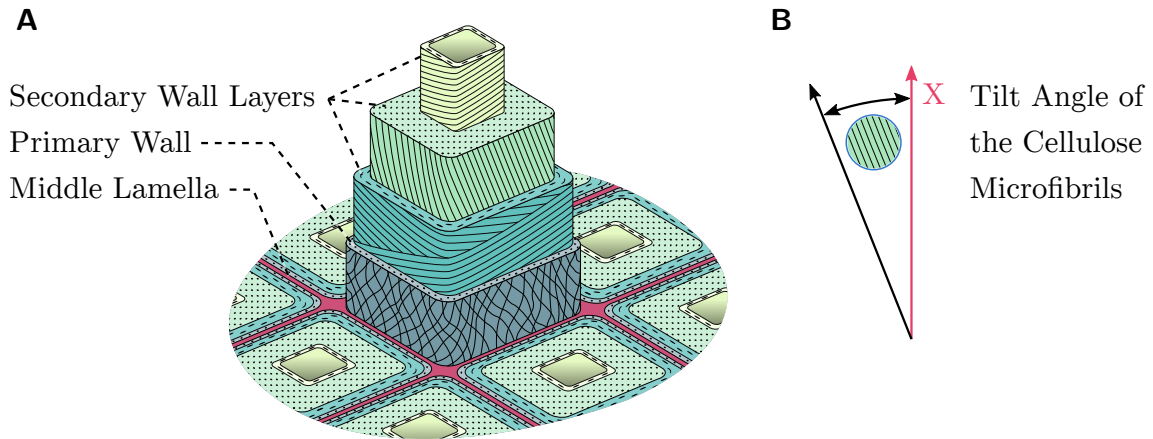


Fig. 4: Structure of lignified cells. A: cell wall layers [7, 75] (redrawn). B: predominant cellulose orientation of the thickest cell wall layer with regard to the longitudinal axis (X).

Characteristic for plant cell walls is the predominance of a particular cell wall layer, or multiple layers with similar structure and composition, which determines the performance of fibrous plant cells.[7, 30, 74] The relation between cell wall architecture and physical properties of fibrous cells and tissues is comparably well studied for wood, due to the ecologic and economic value of trees.[75, 93–97] Their mechanical performance is controlled to a large extent by the stiff and strong cellulose. Elastic moduli of the crystalline cellulose regions are estimated to be approx. 130 GPa.[92, 98–100] In comparison, the matrix components are more flexible with elastic moduli of less than 10 GPa for both lignin and hemicelluloses.[92, 97, 100–103] Consequently, the cellulose–matrix composite in the lignified cell wall shows a strong anisotropy, with high mechanical resilience along the cellulose polymer chains, and low mechanical resilience in the lateral directions.[104] While fibers with low cellulose tilt angles can reach a longitudinal tensile stiffness of more than 30 GPa, large cellulose tilt leads to fiber stiffnesses between 0.5 GPa and 5 GPa.[94, 97] These pronounced differences in mechanical properties are mainly achieved by structure, since the cell wall components—cellulose, hemicelluloses and lignin—remain the same, only with slight variations in their proportions.[94, 97, 105, 106]

2.2.2 Interaction Between Cell Wall and Water

In addition to structure, the water content of cell walls is important for the mechanical but also the swelling properties.[97, 107] During their development plant cells are completely hydrated.[7] After cessation of cell growth and senescence of the organ or the entire plant, the cell wall dries and its inner structure collapses, however, remaining accessible for water beyond cell death.[7, 90, 91] The large number of hydroxy

groups of the principal components causes sorption of moisture.[90, 91] Hemicelluloses is the most hydrophilic of the three principal cell wall compounds, although amorphous cellulose and lignin have accessible binding sites as well.[91] Upon rising moistening levels in the environment, lignified cell walls take up water molecules until an equilibrium is reached.[108, 109] The occupation of free hydroxy groups bulks up the cell wall.[90, 91, 107, 110] It causes breakage of further hydroxy bonds within the matrix, in the amorphous cellulose regions, and at their interface.[110, 111] In consequence, the mechanical resilience diminishes as the environmental humidity level increases.[97, 110–112] Moreover the bulking effect of water molecules penetrating the cell wall can be recognized both microscopically and macroscopically.[107, 113–117] The hygroscopic deformation occurs perpendicular to the cellulose microfibrils, which are dimensionally stable upon humidification in the longitudinal direction of their polymer chains.[90, 112, 118, 119] Swelling upon adsorption and shrinking upon desorption mirrors this directionality on the level of lignified cell walls, tissue pieces, and entire construction elements.[47, 48, 87, 90, 109, 114, 115, 120] Like the mechanical properties, it depends on the angle of tilt of the cellulose microfibrils in the cell walls.[115, 118–121] Steep cellulose orientation causes larger hygroscopic deformation in the transverse plane of a fiber, whereas its longitudinal length remains largely stable, or even shows an inverse behavior.[115, 118–120] Increasing angles of tilt of the cellulose microfibrils lead to a more pronounced shrinking and swelling in the longitudinal direction; the transversal deformation coefficients decline, in comparison.[115, 118–120]

Plants use the anisotropy of the polysaccharide–lignin composite and the related directionality of physical properties to enhance their organs according to specific requirements.[104, 119] In trees, for example, it holds branches statically in position or corrects the gravitropic growth direction of the stem as a reaction to external impacts.[74, 97, 104, 122, 123] Moreover, dynamic structures can be found, specifically developed to perform motion related to seed dispersal.[18, 21, 23, 38, 40, 124] The interrelation between ultrastructure, chemical composition, mechanical resilience, and hygroscopic behavior opens up numerous possibilities for plants to customize tissue properties for specific scenarios, such as the serotinous seed retention and release of *Banksia*.

2.3 Follicle Anatomy and Opening of *B. attenuata*

The cells within the pericarp of the *Banksia* follicles are predominantly sclerenchyma fibers with largely thickened secondary cell walls, and parenchyma cells with thin

walls.[52] They build up three distinguishable layers—endocarp, mesocarp, and exocarp (Fig. 6).[52] The highly serotinous species *B. attenuata* R.Br. from Western Australia (Fig. 1 C) is likely to be the best investigated *Banksia* species with respect to follicle material properties and hence serves as research object for the present work.[52–54, 65] The fibrous tissue of mesocarp and endocarp is aligned from the cone rachis outwards the follicle (Fig. 6 E), tapering asymmetrically towards the junction zone of the pericarp valves and the fracture zone (Fig. 5 B). The mesocarp consists of largely thickened sclerenchyma fibers (Fig. 6 C), which arrange as bundles around vascular cells (Fig. 6 B). Tannin-rich parenchyma surrounds the strands of this branched network and separates it from the endocarp layer (Fig. 6 B). Towards the outside of the follicle, the thick ends of mesocarp fiber bundles form a hard, yet brittle exocarp, which provides protection for the inner parts of the closed follicle (Fig. 6 A). In comparison to the bundle structure of the mesocarp, the endocarp is a continuous layer of sclerenchymatic fibers (Fig. 6 D) with decreasing cell diameter towards the inner edge (Fig. 6 B).

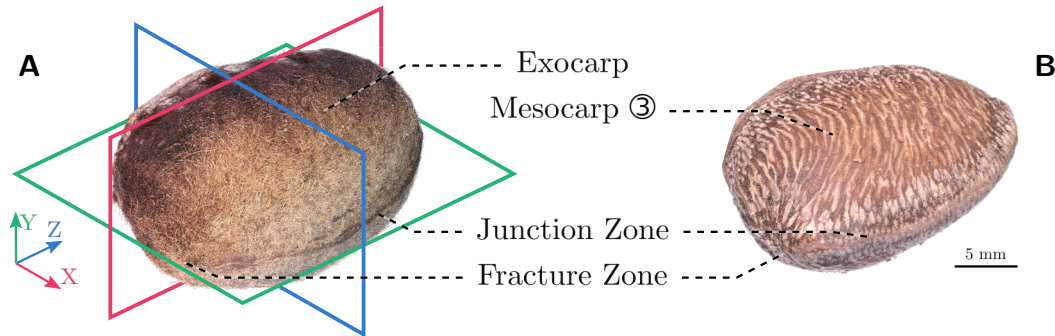


Fig. 5: The *B. attenuata* follicle. A: alignment of a follicle with longitudinal direction X, and transversal directions Y and Z. B: characteristic asymmetric fiber bundle directionality of the outer mesocarp shown on a follicle without exocarp.

Mesocarp and endocarp fibers are not only different in terms of their arrangement and their wall thickening. Their secondary cell walls show opposed cellulose orientation.[52, 54] Cellulose tilt angles of endocarp fibers are small, while the predominant cellulose orientation of mesocarp fibers is perpendicular to the longitudinal fiber axis.[52, 54] Based on the relation between the ultrastructure and the physical properties of lignified fibers, the *Banksia* pericarp can be classified a bi-layer system.[52, 54] Drying of the pericarp, at the end of metabolic activity in the follicle after maturation of the seeds, should induce a higher longitudinal shrinkage for mesocarp than for endocarp fibers.[52, 54]

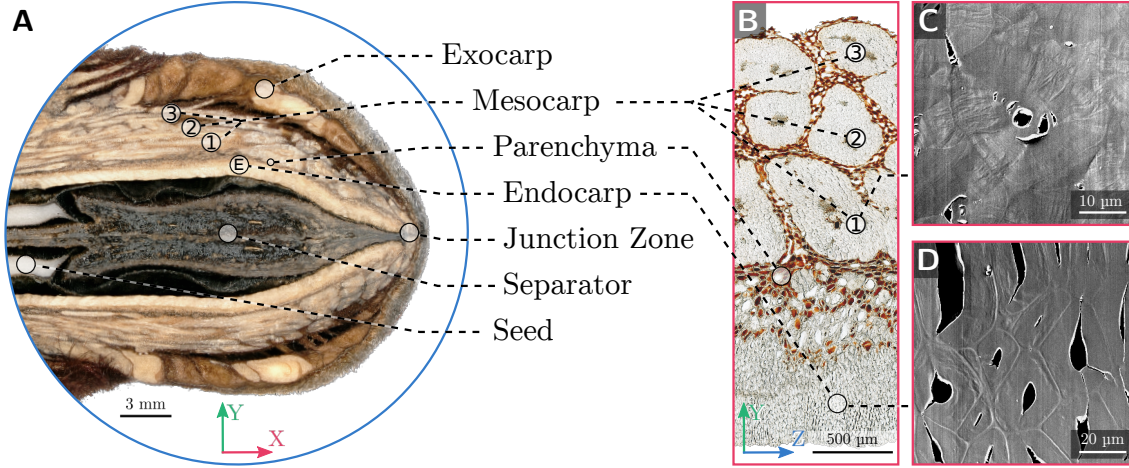


Fig. 6: Anatomy of *B. attenuata* follicles. A: longitudinal cutting plane trough a follicle. B: transverse thin section of mesocarp and endocarp. C: transverse SEM-micrograph of a mesocarp sclerenchyma fiber. D: transverse SEM-micrograph of endocarp sclerenchyma fibers.

For the two-step opening process of *B. attenuata* follicles the different longitudinal shrinkage capacity of mesocarp and endocarp is crucial. During the time of seed retention, the deflection of the pericarp is inhibited by a high bending modulus in the endocarp and the wax-sealed interdigitating junction of the valves (Fig. 6).[52, 54] In consequence, stresses are expected to develop within the pericarp.[52, 54] In regions of harsher climate, a more pronounced biaxial curvature of the pericarp counteracts the stresses more than in colder regions for *B. attenuata*. [54] During the time of seed retention, the waxes in the junction are likely to re-seal small fissures, as they melt at temperatures below 55 °C.[54, 69] Upon heating above 60 °C the endocarp reduces its resistance against the stresses, caused by the mesocarp, by a loss in stiffness, and the waxes in the junction zone melt completely.[54] The prestresses are released by a fracture in the junction zone, leading to partial deflection of the pericarp valves.[52, 54] Subsequently, the valves deflect completely during several cycles of wetting and drying and enable for seed release.[54, 72]

2.4 Experimental Background

The chemical, structural, and physical properties of lignified tissue, as found in the *Banksia* pericarp, can be characterized by manifold methods. In the following section, a selection particularly relevant for the present work will be briefly explained.

2.4.1 Histology

Histological methods were largely developed within the past two centuries, to visualize structures of (plant) tissue which are hardly or not recognizable in the native state of the sample under the microscope.[125] Chemical compounds of staining solutions bind to components of the cell walls.[125, 126] They cause a distinct visually perceptible coloring, which enables for the identification of available binding sites in a simple manner.[126] Lignin, the second most common organic polymer on earth [84], can be identified within a plant cell wall by several histological techniques.[127]

One common method to investigate the lignin distribution in plant tissue is the Wiesner staining.[128] The protocol comprises treatment with phloroglucinol and hydrochloric acid (HCl).[128, 129] Rose coloring indicates for G and S lignin units, while S units alone only lead to slight staining.[128–130] Moreover, this method accounts for endgroups of cinnamaldehyde, a derivative of the lignin biosynthesis, present in the cell wall in smaller amounts.[76, 124, 130]

Another histological method targeting lignin is the Mäule staining which originally required treatment with potassium permanganate (KMnO_4) and aqueous ammonia.[131] In an improved version, this method still uses KMnO_4 , but replaces aqueous ammonia with a buffer, prepared out of tris(hydroxymethyl)aminomethan (Tris) and HCl, to enhance the permanence of the staining.[132] The strong red coloring of the Mäule method specifically indicates for lignin S units.[131, 133, 134]

Both the Wiesner staining and the improved Mäule method have the potential to reveal insights into the chemical composition of *Banksia* pericarp tissue. General information about the distribution of the principal cell wall components are beneficial to specify the further investigations.

2.4.2 Raman Microspectroscopy

Detailed insights into the chemical structure of lignin and ratios of the principal components can be obtained with Raman microspectroscopy.[135–138] This method is based on the inelastic scattering of light upon interaction with matter.[139, 140] Depending on molecular vibrations of a material, the energy of the scattered photons changes, manifesting in a shift of the light’s wavelength towards red (“Stokes”) or blue (“anti-Stokes”).[139–141] These shifts are characteristic for bond vibrations in chemical structures. Moreover, they are sensitive to changes of such vibrations due to varying constraints of chemical structures in their vicinity. For chemical analysis,

this physical principle is applied, using polarized light of a specific wavelength, and the stronger Stokes bands are evaluated.[139, 141] While a single spectra gives information about chemical bonds and their orientation at one particular measurement spot, scanning maps provide insights about their spatial distribution over larger areas of a material.[139–141]

For the chemical and structural characterization of lignified cells and tissues many Raman shifts are of particular interest.[142, 143] The bands relevant for the present work are related to the respective chemical structures in the following: the Raman shift of 1095 cm^{-1} is related to the C–O–C stretching of carbohydrate glycosidic links and depends on the cellulose orientation, 1334 cm^{-1} indicates for the CH_2 bending in lignin, and bands around 1598 cm^{-1} are assigned to the C=C stretching of the aromatic ring of lignin.[138, 142–145] Bands around 901 cm^{-1} correspond to the C–H bending of cellulose and hemicelluloses [142, 146], as well as aromatic ring deformation of lignin.[142] These bands show a low dependency on the cellulose orientation.[147, 148]

For the investigation of the *Banksia* follicle opening, Raman microspectroscopy can give detailed information about the principal components of the pericarp tissue. Especially the proportion of lignin units can be measured and conclusions about the composition of the entire matrix are possible, based on this method.

2.4.3 Polarized Light Microscopy / LC–PolScope

The properties of plant cells are not only determined by compositional characteristics like the lignin content, analyzed by histology and Raman microspectroscopy.[149, 150] The tilt angle of the cellulose microfibrils has a major impact on the mechanical and hygroscopic behavior of the cell wall, too.[97, 114] Crystalline cellulose regions within plant cells lead to birefringence of polarized light—a relation which might be one of the first used for ultrastructural investigations of plant tissue.[7, 14]

Depending on the cellulose orientation, polarized light transmitted through thin sections of plant tissue is retarded.[151] In the liquid crystal–based polarizing light microscope (LC–PolScope), for example, this retardation due to birefringence is calculated based on four images taken of a material at different polarization angles.[151, 152] It allows for qualitative ultrastructural comparisons between tissue regions, or even for the determination of the cellulose tilt angle of plant fibers, considering the crystallinity of the microfibrils.[151, 153, 154]

This method can be applied on low light-microscopic magnifications and is therefore suitable to gain information about the overall distribution of cellulose tilt angles present within *B. attenuata* pericarp fibers. It enables for comparison between tissue regions in one and the same measurement.

2.4.4 Transmission Electron Microscopy

More detailed information about the ultrastructure of lignified cells can be obtained by electron microscopy. Tilt angles of cellulose microfibrils and the distribution of principal components can be quantified down to the level of plant cell wall layers in a transmission electron microscope (TEM).[155–158]

Electron microscopy was invented in the 1930s with the TEM being the first microscope to exceed the resolution limit of light microscopy, due to the short wavelength of electrons compared to light.[126, 159] For that, the electrons are emitted from a source and accelerated by high voltage into a beam.[126, 160] Focused by electromagnetic lenses, they pass through thin specimens.[126, 160] Upon Coulomb interactions with nuclei and with the electron shells of this matter, the beam electrons are mainly elastically scattered at different angles.[126, 160] Widely scattered electrons are blocked out by the objective aperture.[126, 159, 160] Regions in the sample which cause a stronger scattering into larger angles show less intensity on the fluorescence screen or camera.[126, 159, 160]

This specific contrast mechanism is referred to as “amplitude contrast”.[161] In this case elements with higher atomic numbers in the specimen scatter more electrons and therefore produce more contrast.[159] The components of plant cell walls, however, consist to the largest proportion of light organic elements—carbon, oxygen, nitrogen—hardly distinguishable in the TEM.[7, 30] Deposition of heavier elements, like lead citrate, uranyl acetate, or osmium tetroxide, to specific chemical bonds of such a component can improve the contrast of the image and enable for structural differentiation on small length scales, similar to the approaches for light microscopy described in section 3.2.1.[162–164]

For contrastation of lignified cells, KMnO_4 staining is an often used ultrahistological technique.[155, 156, 165–167] Although lighter than the other common stains osmium tetroxide, lead citrate, and uranyl acetate, the atomic numbers of potassium and manganese still exceed those of the organic elements. Such a negative

staining of lignin by KMnO_4 leads to a visibility of cellulose microfibrils in TEM micrographs.[165] When used as post-staining, KMnO_4 leaves interfering artifacts on ultrathin sections which can be removed only partially while the staining effect declines.[168, 169]

Fine periodic structures, like alternating regions of matrix and cellulose in a lignified cell wall, are optically hardly recognizable in TEM images. Such spatial intensity patterns can also be displayed as frequency distributions in reciprocal space—a fundamental relation in crystallography, but also for the beam alignment in the TEM.[160, 161, 170] Furthermore, cellulose tilt angles can be evaluated from TEM images, using for example the Fast Fourier Transformation.[158] This technique allows for a detailed investigation of the ultrastructure in specific regions of the *B. attenuata* pericarp.

2.4.5 Determination of Hygroscopic Deformation

Deformation of lignified cells due to water sorption was not only brought into relation with plant organ motion, like described in section 1.1. This essential property of wood materials is also economically relevant, as it has a major impact on craft processing and industrial engineering of timber and wood products.[171]

Accordingly, numerous methods are available for the determination of hygroscopic deformation, commencing on the level of the cellulose microfibrils, over thin cell wall sections and tissue blocks, up to the level of tree trunks.[80, 107, 114, 116, 172] Irrespective of the various length scales, all these techniques are based on measurements of length, area, or volume.

Experiments on the hygroscopic deformation of *B. attenuata* pericarp can give valuable information about how water affects the tissue dimensions, as the opening mechanism is not only related to heat exposure, but also to subsequent wetting and drying.[72]

2.4.6 Tensile Test

The tensile test is a destructive method commonly used to determine physical properties of materials on a multitude of length scales.[173] Defined specimens, clamped at their outer edges, are incrementally loaded until material failure, while force and displacement values are recorded (Fig. 9 C, D).[174] For the investigation of biological fibers, special preparation techniques and customized instruments were

developed. They allow for precise measurements, even at small length scales and potentially in controlled environmental conditions.[175–177]

A feasible way of single fiber preparation for tensile tests is their manual isolation with fine tweezers.[178] As the clamping of small specimens is particularly challenging, fiber samples are often glued over frames made of plastic, which provide stability throughout the mounting process.[179, 180] Another approach is the grip-mounting of fibers with epoxy drops in small metal grooves.[181, 182] For precise alignment of the specimens, adjustment stages are used, or fibers can be oriented by the capillary forces of a water bridge between the mounting edges, directly inside the machine.[183, 184] During the experiment, the optical determination of the sample strain allows for high accuracy, compared to the error-prone strain measurement via the test stage mechanics.[179] In general it can be observed, that the experimental effort for tensile tests increases as sample size decreases, and elaborate solutions become necessary to reach a sufficient precision of the instruments for measurements at the small scales.[185, 186]

Tensile tests of *B. attenuata* pericarp tissue allow for a mechanical characterization of the follicle material. The detailed approaches described above illustrate the potential of this method for experiments on small scales. Moreover, custom-built instruments can be enhanced and modified to specific test requirements, such as humidification of the samples or automatized procedures.

2.4.7 Nanoindentation

Nanoindentation allows for the characterization of lignified cells at even higher spatial resolution.[94, 187] A diamond indenter tip pushes into the material, down to the resolution of single areas within a cell wall (Fig. 10 C).[94, 187] Among others, the flat Berkovich pyramid is one of the most common nanoindenter shapes, not only for plant materials.[188] During the experiment the mechanical response of the sample to a specific load scenario of the indenter is recorded (Fig. 10 D).[188] The resulting load–displacement curve allows for the determination of the “reduced modulus”, taking into account the stiffness upon unloading (Fig. 10 D) and the contact area with the indenter tip.[187–189] The material’s hardness can be calculated by the maximum load and the contact area.[187–189]

Nanoindentation is also suitable to investigate material properties in variable moistening regimes. The specimens can be tested at defined relative humidity levels

or at a specific temperature.[188, 190] This possibility is particularly interesting for lignified cell walls like found in the *B. attenuata* pericarp, as the mechanical relevance of their single layers depends on moistening state, and structure and composition of the principal components.[190–192]

3 Material and Methods

3.1 Origin of the Sample Material

Cones of *Banksia attenuata* R.Br. plants, growing in their natural habitat, were collected along a climatic gradient in Western Australia by Jessica Huss in 2014 and in 2016 (Fig. 1 B).[54] Single follicles were cut out of the cones from the geographic locations “site 1” (29.62080 °S, 115.21177 °E), “site 2” (30.04438 °S, 115.32618 °E), and “site 5” (31.69048 °S, 115.87981 °E) [54] with a hand saw, and the exocarp was removed by means of a firmer chisel prior to the experiment-specific sample preparation (Fig. 5 B).

3.2 Compositional and Ultrastructural Investigations

3.2.1 Histology

Thin transverse sections (thickness: 5 µm) were cut with a cryo-microtome (HM 560 M, Microm, Walldorf, Germany) from a *B. attenuata* (site 2) pericarp block, containing mesocarp and endocarp. The sections were stored in water overnight before they were histologically stained following two different protocols from the literature.[129, 132]

One set of sections was stained according to the Wiesner method, using phloroglucinol and HCl.[128, 129] The sections were placed in a droplet of 1 % phloroglucinol, solved in HCl-ethanol (1:3) [129] on a glass slide, covered with a cover slip, and sealed with nail polish, before microscopic images were taken with a digital light microscope (VHX 5000, Keyence, Osaka, Japan, objective: VH-U100UR).

Another set of sections was stained with the improved Mäule method, using KMnO₄, Tris, and HCl.[132] The sections were placed in a droplet of 1 % KMnO₄ aqueous solution on a spot plate for 5 min. Subsequently, the sections were rinsed three times with distilled water, before placed in 1 N HCl for 30 min.[132] The stained sections, mounted on glass slides, covered with a coverslip, and sealed with nail polish, were imaged with a digital light microscope as explained above.

3.2.2 Raman Microspectroscopy

For the Raman investigation of the *B. attenuata* pericarp four small blocks from different follicles (site 2, block size: complete thickness over mesocarp and endocarp, 4 mm longitudinal, approx. 2 mm in width) were cut in the water-saturated state with a diamond wire saw (DWS 100, Diamond WireTec, Weinheim, Germany) and clamped between small aluminum screw-jaws. The transverse surfaces of the samples were cut plane in the frozen state with a diamond knife (cryoimmuno 45°, DIATOME, Nidau, Switzerland) using a cryo-ultramicrotome, cooled by liquid nitrogen to -140°C (PowerTome XL, RMC Boeckeler, Tucson, AZ, USA).

Within three consecutive mesocarp fiber bundles, cross-sections of single cell walls were scanned with a Confocal Raman Microscope (alpha300, WITec, Ulm, Germany), equipped with a $60\times$ water immersion objective (NIKON Corporation, Tokyo, Japan, $\text{NA} = 1.0$), using a frequency doubled linearly polarized Nd:YAG laser ($\lambda = 532\text{ nm}$, oxxius, France), and a piezo-scanner (P-500, Physik Instrumente, Karlsruhe, Germany). The measurement spots were exposed to a laser power of 22 mW, determined directly in the object area with an optical power meter. Spectra were acquired with a CCD detector cooled by a Peltier device (DU401A-BV, Andor, Belfast, North Ireland) after passing a spectrograph with a grating of 600 g mm^{-1} and a spectral resolution of 3 cm^{-1} (UHTS 300, WITec, Ulm, Germany). Two to three cell walls were scanned in each of the fiber bundles of all four samples. The measurements were conducted with the Witec Control FIVE software, and evaluated in Witec Project FIVE (Version 5.2, WITec, Ulm, Germany).

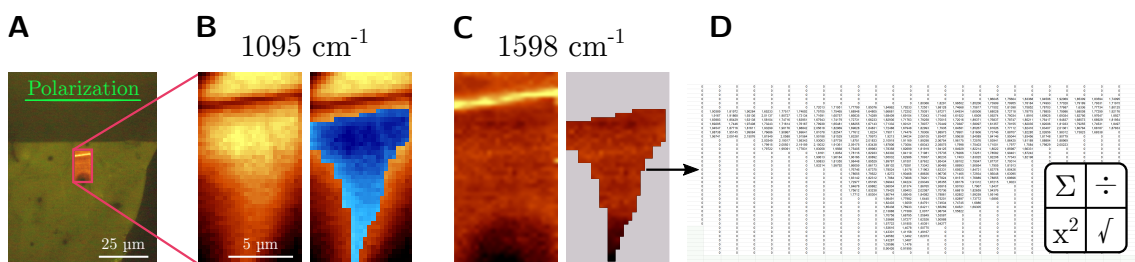


Fig. 7: Evaluation of the Raman results. A: overview, scan-measurement of a fiber cross-section area in the outer mesocarp. B: selection of the region of interest (blue) in an intensity map of a polarization-dependent peak, related to cellulose. C: transfer of the region of interest to an intensity map of a peak related to lignin. D: output of the intensities of the lignin-related peak within the region of interest for data analysis.

Cosmic ray peaks in the data were removed with a filter size of 2 and a dynamic factor of 4. The background of the spectra was subtracted by a third-order poly-

nomial function over five hand-chosen mask regions in the spectra, containing no Raman peaks. For better comparability, the spectra were normalized to the maximum height of the 901 cm^{-1} peak, which is apparently similarly pronounced in all the measurements.

Peak intensity maxima were detected with the WITec Project FIVE filter function for the peaks at approx. 1095 cm^{-1} , 1334 cm^{-1} , and 1598 cm^{-1} . Within 1095 cm^{-1} peak maps of each scan, the cell wall section of high intensity—where the horizontal laser polarization matches the cellulose orientation—was selected as region of interest (Fig. 7 A, B).[147] From the maps of each peak (1095 cm^{-1} , 1334 cm^{-1} , 1598 cm^{-1}), all the intensity values within the region of interest were exported and evaluated in OriginPro 2020b (Fig. 7 C, D).

3.2.3 Polarized Light Microscopy / LC-PolScope

Thin sections ($3\mu\text{m}$ thickness) were cut by means of a cryo microtome (CM1860, Leica, Wetzlar, Germany) from a *B. attenuata* (site 2) pericarp block, containing mesocarp and endocarp. They were stored in distilled water overnight, before they were brought onto glass slides and covered with a coverslip. The sections were investigated with a liquid crystal-based polarizing light microscope (Eclipse 80i, Nikon, Tokyo, Japan, in conjunction with the LC-PolScope-System, a cooled CCD camera, and the Software Abrio 1.4, CRi, Inc., Woburn, MA, USA). Images were taken in Retardance Mode for the qualitative evaluation of the cellulose orientation within the pericarp.

3.2.4 Transmission Electron Microscopy

Small blocks of inner and outer mesocarp fiber bundles of *B. attenuata* (site 2) were cut with a diamond wire saw (DWS 100, Diamond WireTec, Weinheim, Germany) and a razor blade into small strips (X and Y length $< 0.5\text{ mm}$, Z length several mm). These samples were fixed with 4 % paraformaldehyde and 2.5 % glutaraldehyde in a 100 mM cacodylate buffer (pH 6.9) for 24 hours at 4°C . Subsequently, they were prestained with 3 % KMnO_4 in acetate buffer (pH 5.6) for 2 hours and rinsed three times.[163, 165] The samples were dehydrated in an ethanol series, before they were infiltrated with Spurr's epoxy resin [193] and embedded for 16 hours at 70°C .

The blocks were sectioned with a diamond knife (ultra 35° , DIATOME, Nidau, Switzerland) by means of an ultramicrotome (PowerTome XL, RMC Boeckeler, Tucson, AZ, USA) at room temperature. Ultrathin longitudinal and transversal sections

(thickness 100 nm) were stretched on water with vapor of chloroform immediately after cutting, and collected on Formvar-coated 200 mesh copper grids.

These specimens of ultrathin sections were investigated with a TEM (JEM ARM-200F, JEOL, Akishima, Japan) at an acceleration voltage of 200 kV. Images were recorded by a CMOS-camera system and subsequently processed in Digital Micrograph (GATAN, Pleasanton, CA, USA). Overlapping detail images of a transverse section were stitched together in Inkscape (Version 1.0, Inkscape Project). For the investigation of the layer homogeneity over the entire cell wall thickness they were oriented in an overview image between distinct points, due to the image rotation for different magnifications and focus settings.[159] Accordingly, overlapping longitudinal detail images containing the turning point of tangential cell wall layers were stitched together for the determination of the cellulose microfibril angle related to the fiber longitudinal axis. These images were oriented between two pits of an overview image.

To visualize the periodic pattern of cellulose and matrix in longitudinal sections of *B. attenuata* mesocarp fibers, the images in the center of the region of interest were converted by the “Reduced Fast Fourier Transformation” process available in Digital Micrograph. Within these diffractograms the intensities of the first ring were azimuthally integrated in DPDAK (version 1.4.1, DESY / MPIKG, Germany) to determine the angular dependency of the pattern with regard to the longitudinal axis of the fiber.

3.3 Physical Tests

3.3.1 Hygroscopic Behavior

Thin longitudinal and transversal sections (20 μm thickness) of *B. attenuata* (site 1 and site 5) pericarp were cut with a rotary microtome (RM2255, Leica, Wetzlar, Germany). Sample areas, containing the intact endocarp layer and three visually distinguishable mesocarp fiber bundles, were isolated with a razor blade. The sections, nine specimens per site and anatomical direction, were individually placed under a digital light microscope (VHX 5000, Keyence, Osaka, Japan, objective: VH-U100UR) on a heated microscope slide, covered with a coverslip. The samples were heated from 30 $^{\circ}\text{C}$ to 90 $^{\circ}\text{C}$ in steps of 10 K with a heating gradient of 7 K min^{-1} . Images of the samples were taken for each step 180 s after reaching the temperature setpoint at room humidity (relative humidity between 41.5 % and 56.3 %). After

the 90 °C step, the setup was allowed to cool down again. The samples were completely moistened with distilled water as soon as the slide's temperature reached 30 °C again. Images in the wet state were taken 180 s after the moistening.

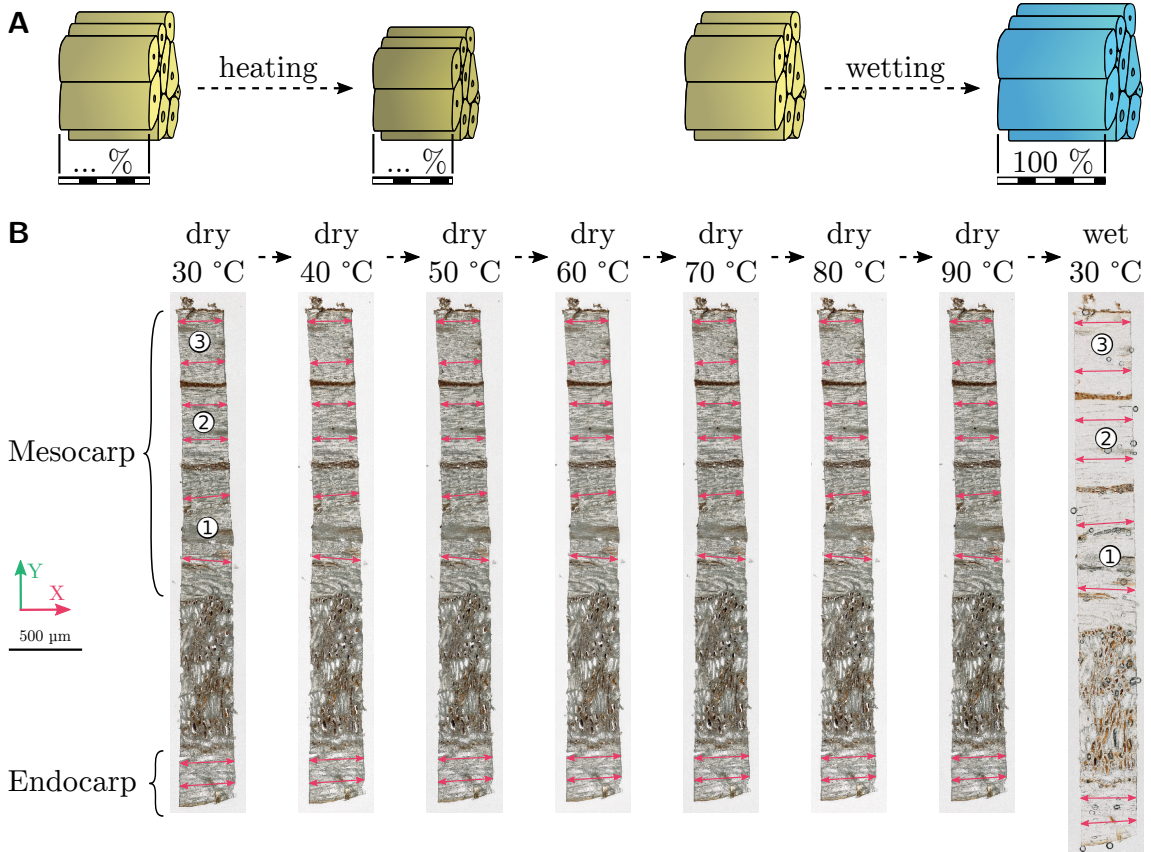


Fig. 8: Determination of the hygrothermal deformation on the example of the longitudinal direction (X). A: scheme of the experimental procedure and measurement acquisition. B: experimental sequence of one longitudinal section with measurement lines.

For the evaluation of the hygroscopic length changes of specific tissue directions, prominent points were defined in the endocarp and in each mesocarp fiber bundle. Line measurements to scale between these points were taken on images of each temperature and moistening state with ImageJ (version 1.51n)—two measurements per tissue region, per anatomical direction, and per sample. OriginPro 2015G was used to evaluate the data.

3.3.2 Tensile Test of Tissue Strips

Tissue strips of endocarp and three consecutive fiber-bundles from the inside, the center, and the outside of the mesocarp (Fig. 6 B) were isolated (width between

0.1 mm and 0.3 mm) with a razor blade from thin longitudinal pericarp sections (thickness: 50 μm) of *B. attenuata* (site 2). They served as specimens for the tensile tests, 10 to 14 samples per tissue region and wetting state. Two sets of samples were prepared: one set in the dry state at room conditions, and another in the wet state, immersed in 50 % glycerin. The samples' ends were glued to the edges of foliar frames (Fig. 9A, B) with super glue (Loctite 454, Henkel AG & Co. KGaA, Düsseldorf, Germany). The clamping lengths between the gluing points were determined by ImageJ line-measurements on images taken with a digital light microscope (VHX 5000, Keyence, Osaka, Japan, objective: VH-U100UR).

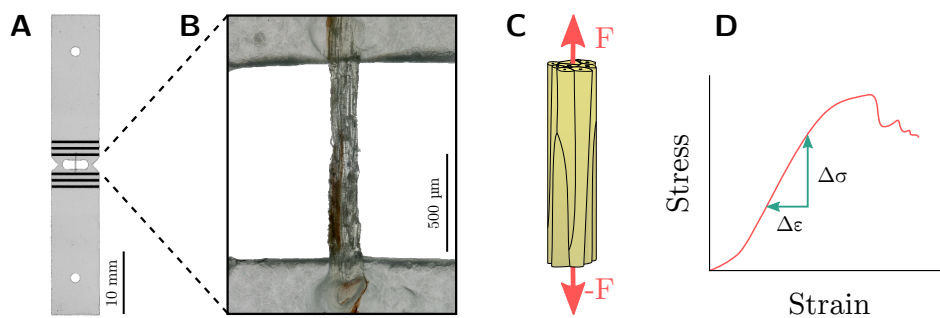


Fig. 9: Tensile test experimental background. A: sample holder. B: *B. attenuata* mesocarp tissue strip glued to the edges of the foliar frame. C: scheme of the experimental principal. D: stress-strain development and determination of the stiffness.

Tensile tests were conducted using an in-house built testing stage equipped with a 2.5 N load cell (model 31E, Honeywell, Columbus, OH, USA), controlled by a LabView-based program. The expansion was captured by videoextensometry at points of high contrast near the samples' gluing points, using a light microscope (SZX7, Olympus, Tokyo, Japan) equipped with a digital camera (A 102f, Basler AG, Ahrensburg, Germany).

One set of samples was tested in the dry state at room conditions (relative humidity between 23.1 % and 24.8 %, temperature between 21.6 °C and 23.1 °C). Another set of samples was tested in the wet state at room temperature (between 22.0 °C and 23.7 °C), moistened by a continuous stream of water steam provided by a vaporizer (BH-860E, Honeywell, Charlotte, NC, USA). The samples were stressed at a tensile feed rate of 5 $\mu\text{m s}^{-1}$ until material breakage (test span between 1.0 mm and 1.5 mm). The force values and the related extensions were recorded throughout the test. After the measurement, each sample was cut perpendicular to the grain with a razor blade. The transverse sample surfaces were imaged by means of an

environmental scanning electron microscope in the low vacuum mode at 0.75 Torr, using an acceleration voltage of 12.5 kV (ESEM Quanta 600 FEG, FEI, Hillsboro, OR, USA). The cross-section areas including inward cell lumina were measured with ImageJ (version 1.51n) for the calculation of the stress. Data was processed with OriginPro 2015G. For each sample, the stiffness was determined as the slope of the initial linear section of the stress-strain curve (Fig. 9 D).

3.3.3 Nanoindentation

For nanoindentation in wet and dry condition pieces of *B. attenuata* (site 2) pericarp were sawn from a follicle in the dry as well as in the wet state and screw-tightened between small aluminum clamping jaws (Fig. 10 A). Separate sample preparation for both moistening states was necessary because the pericarp tissue shows substantial deformation between dry and wet condition. It rules out nanoindentation measurements in both states on the same sample. The transverse sample surfaces (Fig. 10 B) were cut plane with a diamond knife (cryoimmuno 45°, DIATOME, Nidau, Switzerland) by means of an ultramicrotome (PowerTome XL, RMC Boeckeler, Tucson, AZ, USA). The dry samples were cut at room conditions. The wet samples were frozen in the water-saturated state in the chamber of the cryo-ultramicrotome at -140°C , before they were cut in these cryo conditions.

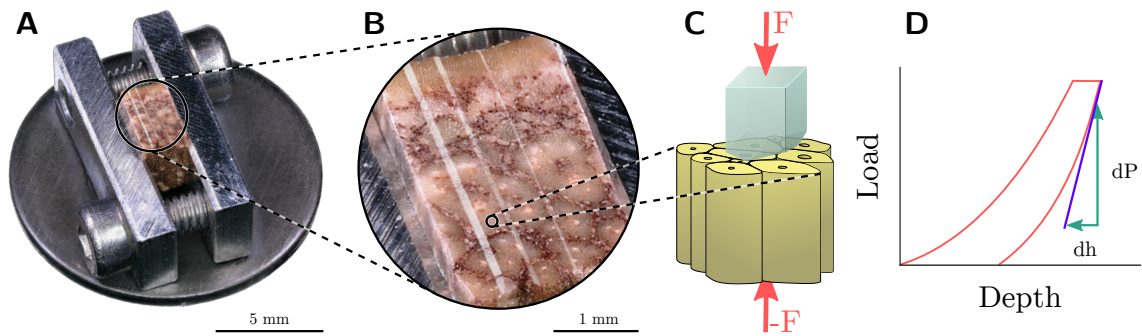


Fig. 10: Nanoindentation experimental background. A: clamped *B. attenuata* sample. B: sample surface for measurement. C: scheme of the experimental principal. D: load-depth development and determination of the reduced indentation modulus.

For nanoindentation a nanomechanical tester (Ubi-1, Hysitron Inc., Minneapolis, MN, USA) equipped with a Berkovich indenter was used. The dry samples, three specimens, were tested at room conditions. The wet samples, two specimens, were allowed to soak distilled water through a piece of tissue from a water storage. The load-function contains three segments: linear loading to $250\ \mu\text{N}$ over the time of 2.5 s, holding at $250\ \mu\text{N}$ for 15 s, and linear unloading to $0\ \mu\text{N}$ over the time of 2.5 s. The

regions for the tests were determined for the samples as adjacent cells throughout the endocarp and within three adjacent mesocarp fiber bundles, corresponding to those of the tensile-test samples and the measurement-areas for hygroscopic deformation. Cell walls within these regions were scanned with the indenter-tip before and after each measurement, to set the indentation points and to check the position of the indents subsequently. Data of indents, which clearly could be associated with the fiber cell wall, was evaluated in the Bruker-Hysitron testing program TriboScan and in OriginPro 2015G.

3.4 Novel Experiment to Determine Fiber Contraction Forces

3.4.1 Requirements for Precise Fiber Tests in Variable Climate

Drying-induced stresses in the mesocarp are considered the driving force behind the *Banksia* follicle opening (section 2.3) and the other mentioned examples of plant motion, like *Ruellia* fruits and *Pinus* cones (section 1.1), based on ultrastructural measurements and on swelling or shrinking experiments.[18, 23, 25, 52, 54] The actual forces, generated on the tissue or fiber level upon drying, however, are still unknown. Data about the moisture-induced stress generation is particularly relevant for the understanding of the overall opening mechanics. For the experimental determination, a common micro tensile test setup like described in section 3.3.2, combined with humidity control, is the groundwork, as the main forces are expected to be longitudinally generated by the fibers.

First tests with this setup, to determine the longitudinal drying stresses of *B. attenuata* mesocarp tissue strips from the wet state, led to breakage of the specimens, possibly due to flaws in the fibers, caused by microtome sectioning of the tissue. To overcome this limitation but also the difficulty of not knowing how many intact and how many cut cells a tissue strip contains, single fibers were mechanically isolated with fine tweezers [178], glued onto plastic foliar frames [179] and subsequently tested.

The initial results of the single fiber tests were difficult to reproduce and the measurement accuracy was not sufficient. Many fibers already broke during mounting, since the sample holders were too instable. During the experiments, the force offset of the load cell varied, depending on the temperature and the relative humidity in the chamber. Variations like this are first of all disadvantageous measurement errors. But even more importantly in terms of the experiment, force-related position

control is hardly possible in such conditions, where the relative humidity changes in cycles over a range of 50 % within three to four hours. For dynamic measurements of short single fibers over several cycles of changing moistening conditions, the experiment had to be enhanced, as will be described in the following sections.

3.4.2 Sample Holders and Fiber Specimens

For tensile tests of short specimens, like sclerenchyma fibers from *B. attenuata* mesocarp, common plastic sample holders are too pliable to provide stability for the transfer and in-axis test. Moreover, interactions between the plastic and moisture can have unfavorable effects on the results of tests in changing environmental conditions.[194, 195] To minimize these error sources, special sample holders were constructed for the determination of tensile parameters of single fibers upon changing moistening states. They were built out of a raw block of 40 % glass fiber reinforced polyphenylen sulfide (Tecatron GF40, Ensinger GmbH, Nufringen, Germany). This material is specifically designed to ensure high dimensional stability in changing climatic conditions. Moreover, its low heat conductivity compared to metals isolates the specimen thermally from the holder mounting, which is connected to the colder chamber housing. After drilling two 3 mm holes at a distance of 4 mm into the block, plane slices of approx. 1.3 mm thickness were cut by means of a water-cooled diamond wire saw (DWS 100, Diamond WireTec, Weinheim, Germany) to avoid fabrication stresses and variances due to surface processing like they can be observed in thin commercial sheets. The slices were numbered uniquely and separated centrically along the 1 mm bridge between the holes with the diamond wire saw. The outer bridges were cut back to a distance of approx. 2 mm. The inner bridge edges, which later carry the fiber specimen, were chamfered downwards with sanding paper. Both sides of one slice were fixed on a heating plate (Fig. 11 A) to a distance of 150 μ m to 200 μ m, measured under a macroscope (Z16 APO, Leica Camera AG, Wetzlar, Germany) with a measurement ocular. Small aluminum jaw pieces were attached with sealing wax to both sides in order to reversibly reassemble both pieces of one sample holder (Fig. 11 A, B).

Single fibers of *B. attenuata* (Site 2) outer mesocarp were used to test their behavior in different moistening conditions; eight samples in total were successfully tested. They were isolated manually under a binocular microscope (Steindorff, Berlin, Germany) with fine tweezers in the wet state.[178] The fibers were allowed to dry at room conditions before they were glued to the edges of the sample holders (Fig. 11 C) with super glue (Loctite 454, Henkel AG & Co. KGaA, Düsseldorf, Ger-

many). After the glue dried overnight, a sample holder was attached at its outer spaces with two-component epoxy resin (Plus Schnellfest, UHU GmbH & Co. KG, Bühl/Baden, Germany) to aluminum plates, screwed to the mountings of the tensile tester (Fig. 11 D). The epoxy fastening was chosen to reduce mounting stresses, which occur when screwing a sample holder directly to the mounting of the tester. Moreover, the resin can compensate for minor level differences between the mounts on both sides, which would lead to a misalignment of short fibers or even to breakage ahead of the test (Fig. 11 E). Within one hour the resin reached a sufficient hardness, so the aluminum jaw pieces could be removed prior to the experiment. They were heated with an annealing wire, pushed through small drilled holes, until the sealing wax melted.

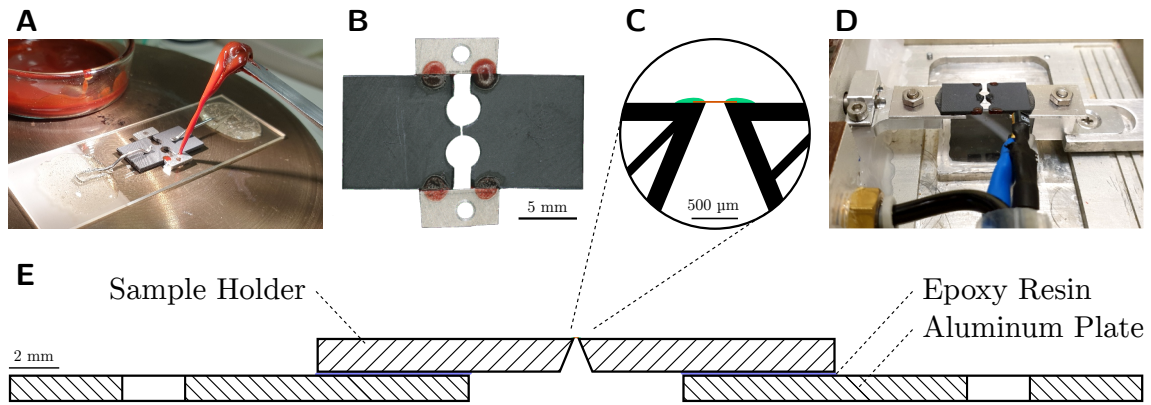


Fig. 11: Sample holder for hygro-tensile-cycles. A: assembly of the holder with sealing wax. B: complete sample holder. C: fiber gluing onto the holder (schematically). D: mounting of the sample in the test chamber. E: technical drawing of the holder mounting on aluminum plates in the test chamber.

3.4.3 Precision Enhancement of the Tensile Test Stage

The samples were tested inside an air-conditioned chamber (volume approx. 160 cm^3) at 20°C under changing humidity regimes. Water cooling of the top and bottom of the chamber through a circuit flow was provided by a thermostat (Ministat 125 cc3, Peter Huber Kältemaschinenbau AG, Offenburg, Germany) with temperature control close to the sample by a PT100 temperature sensor (precision checked with Testo 735 thermometer, Testo SE & Co. KGaA, Titisee-Neustadt, Germany, calibrated by Dr. Wernecke Feuchtemesstechnik, GmbH, Potsdam, Germany). Moistened air for the different levels of relative humidity was prepared by a humidity generator (HumiGen-04, Dr. Wernecke Feuchtemesstechnik GmbH, Potsdam, Germany) and brought into the chamber at a flow rate of 80 l h^{-1} . The climatic conditions in the chamber were measured at the vertical level of the sample with a horizontal off-

set of approx. 1 cm by means of a humidity–temperature sensor (SHT85, Sensirion AG, Stäfa, Switzerland, calibrated by Dr. Wernecke Feuchtemesstechnik GmbH, Potsdam, Germany).

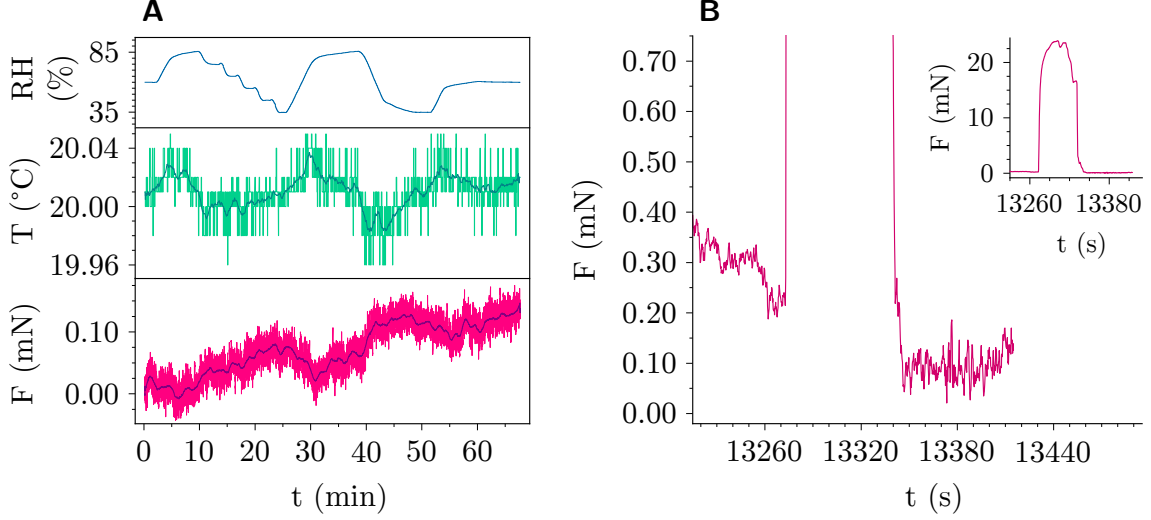


Fig. 12: Force offset. A: during two unloaded humidity cycles. B: after the final loading at the end of a complete experiment.

Isolated from the sample chamber the load cell (model 31E, range 0.5 N, Honeywell, Columbus, OH, USA) was climatized separately by a constant flow of dry air of $98\text{--}100\text{ ml min}^{-1}$ (measured by a red-y compact mass flow meter, Vögtlin Instruments GmbH, Muttenz, Switzerland) to minimize the force offset caused by changes of the air humidity. The dew point of the dry air varied cyclically between $-30\text{ }^{\circ}\text{C}$ and $-40\text{ }^{\circ}\text{C}$ for technical reasons in the supply system (measured by a dew point meter, DewMaster SPS5-HTS2, Edgetech Instruments, Hudson, MA, USA, calibrated by Dr. Wernecke Feuchtemesstechnik, GmbH, Potsdam, Germany). The shaft connecting load cell and sample holder, 5 mm in diameter, was contactlessly (gap size 0.5 mm) led through a hollow divider made of phenol high-pressure laminate. Mixed air of both chambers was soaked out of the divider's interstice at a flow rate of $135\text{--}145\text{ ml min}^{-1}$ (measured by a red-y compact mass flow meter, Vögtlin Instruments GmbH, Muttenz, Switzerland) by means of a Venturi nozzle (ZH 05B, SMC, Tokyo, Japan).

Prior to the measurement, the sample chamber was conditioned overnight at the average relative humidity of the whole experiment to minimize effects of cross-flow between the chambers on the load cell tare value. Throughout several hours of a single experiment and various cycles of humidity changes in the sample chamber, it was possible to keep the load cell drift below 1 mN (Fig. 12 B) due to a constant humidity

environment of $\pm 0.1\%$ relative humidity, measured with a humidity–temperature sensor (SHT25, Sensirion AG, Stäfa, Switzerland). Still, the load cell signal is affected (Fig. 12 A), possibly also by slight changes in temperature of the whole stage, due to its interaction with the relative humidity and the delayed response of the thermostat.

For the sample position displacement a precision translation stage (M–126.DG1, Physik Instrumente GmbH & Co. KG, Karlsruhe, Germany) was used. The motor itself was separated from the sample chamber by a solid aluminum divider, leaving out a feedthrough for the sample mounting.

3.4.4 Assembly for Fiber Wetting

For the wetting of the short *Banksia* mesocarp fibers moistened air was prepared by a humidity generator (Wetsys, Setaram Instrumentation, Caluire, France) at 30°C and $77\%–78\%$ relative humidity. Pumped at 50 ml min^{-1} through silicone tubes it was brought to the specimen with a pulled and partially grounded micropipette (1 mm borosilicate capillary: World Precision Instruments, Sarasota, FL, USA, tip diameter approx. $100\text{ }\mu\text{m}$; micropipette puller: Model P–97, Sutter Instrument Co., Novato, CA, USA; Micro Grinder EG–400, Narishige, Tokyo, Japan).

The micropipette was guided inside a glass Pasteur pipette, moved by a manually driven translation stage (OWIS GmbH, Staufen i. Br., Germany) through a hole in the top of the chamber. Surplus flow was allowed to exhaust through an outlet. All the tubes, junctions, and the Pasteur pipette were wrapped with polyurethane–isolated copper wire (0.1 mm diameter incl. insulation varnish, VEB Kabelwerk Adlershof, Berlin, East Germany) and coated with epoxy resin (Plus Schnellfest, UHU GmbH & Co. KG, Bühl/Baden, Germany). The wire was heated by the direct current of a 12 V, 0.5 mA transformer (RS Pro, Ansmann AG, Assamstadt, Germany) to avoid condensation of the transported moisture. The tube temperature was measured (USB–TC01, K–type thermocouple, NI, Austin, TX, USA) and adjusted to approx. 28°C by reducing the current with a potentiometer.

Approximately 2 mm of the micropipette’s tip protruded the end of the heated Pasteur pipette into the 20°C environment of the tensile test chamber. Inside the micropipette, water condensed to small drops along this unheated length. By increasing the pressure when closing the exhaust outlet, a single droplet was formed between the tip of the micropipette and the specimen fiber. After each wetting step

the outlet was opened again and the pipes were allowed to dry at a relative humidity $< 5\%$ for 2 min. The experimental setup is displayed as a schematic circuit diagram in Fig. 13.

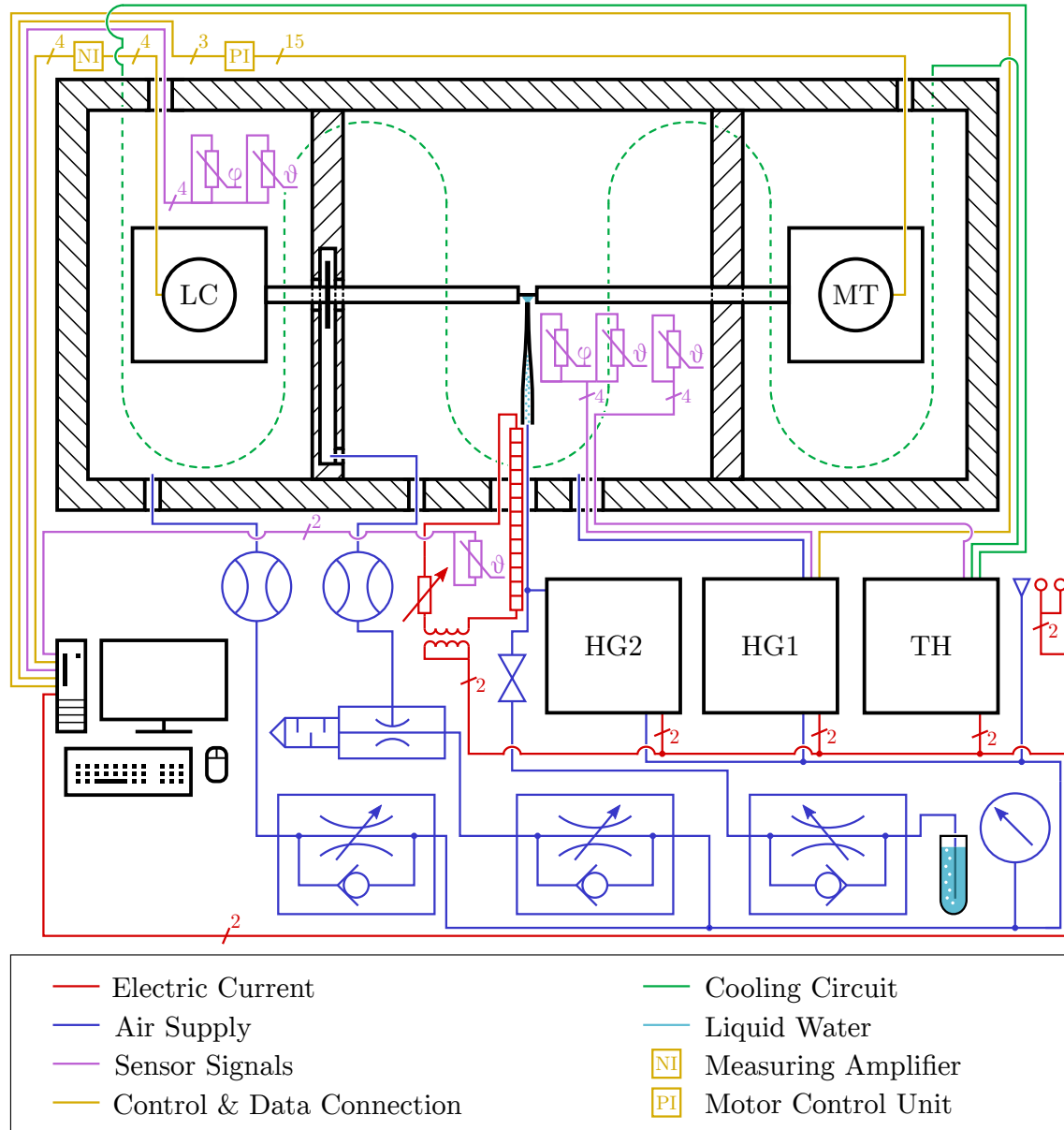


Fig. 13: Schematic circuit diagram of the conditioned tensile test setup. LC: load cell. MT: motor. TH: thermostat. HG1: HumiGen-04 humidity generator. HG2: Wetsys humidity generator.

3.4.5 Experimental Sequence

The experimental parameters were controlled by and logged in a Labview-based program (Labview, NI, Austin, TX, USA), running a semi-automatic test procedure. It contained five basic humidity cycles, including segments of force-controlled

position adjustment and one drying cycle of force recording at fixed position. The desorption and the adsorption process of lignified material shows a hysteresis—the water content of the material is higher upon desorption than upon adsorption at the same relative humidity.[107, 196] To compare hygroscopic deformation and hygroscopic stress generation of mesocarp fibers, the desorption process was found experimentally more relevant, as plant cell walls, like in the *B. attenuata* seed pod, develop in the wet state and dry when disconnected from the plant’s metabolism.[7]

In the experiment the relative humidity was regulated at a max. gradient of $10\% \text{ min}^{-1}$. Control forces were set to -0.2 mN or 0.0 mN for shrinkage and to 0.3 mN or 0.5 mN for swelling movement, respectively. The control parameters were set to a maximum velocity of $7 \mu\text{m s}^{-1}$ at a max. proportional gain of $0.05 \mu\text{m s}^{-1}$ and an in-range force limit of 0.5 mN . Images of the fiber specimens were recorded at the end of each step, at stable humidity, force, and position, with a digital microscope (VHX 5000, Keyence, Osaka, Japan, objective: VH-U100UR).

In cycle 1, the fibers were dried unimpededly from the wet state at a relative humidity of 85 %, then in steps of 10 % relative humidity down to 35 %. The relative humidity of 85 % was chosen the maximum to avoid condensation on colder parts of the test chamber and 35 % relative humidity represent minimum values in Southwest Australia on a dry day.[197] Throughout this first cycle, the motor displacement followed the longitudinal deformation of the fiber to determine the strain at the different moistening levels.

In cycle 2, the generation of drying forces of the fiber upon impeded shrinkage were determined. After wetting the fibers, the translational stage movement was stopped at the maximum displacement. The fibers were dried in the same steps as in cycle 1. After the end of cycle 2, at the relative humidity of 35 %, the force-controlled motor displacement was activated again so the shrinkage forces were released completely as the fibers retracted partially.

Subsequently, three more cycles of unimpeded deformation upon wetting and drying were implemented to determine the fibers’ capability of length regeneration after the impeded shrinkage. These cycles contained less humidity steps than before; the fibers were gradually moistened to 85 % relative humidity, completely humidified with water, allowed to dry at 85 % relative humidity, and gradually dried to 35 % relative humidity. After these three cycles the fibers were conditioned at 60 % rela-

tive humidity for 3 min, before the final tensile loading at steady stage velocity until breakage. After the tests, the transverse fiber sections were cut plane with a scalpel and imaged in an environmental scanning electron microscope in the low vacuum mode at a pressure of 0.75 Torr and an acceleration voltage of 5 kV or 10 kV (ESEM Quanta 600 FEG, FEI, Hillsboro, OR, USA) for subsequent determination of the cross-section area with ImageJ (version 1.53c).

3.4.6 Test of *P. abies* Fibers for the Assessment of the Setup

The experiment described above was specifically developed to determine the relation between hygroscopic shrinkage and drying forces in *B. attenuata* mesocarp fibers. Measurements at this precision level are to the author's knowledge completely new. It was therefore essential to test the capability of the setup with a material more intensively studied than fibers of the *Banksia* mesocarp. Fibers of adult normal wood, stem compression wood, and branch compression wood of *Picea abies* H.KARST. were selected as test material; three fiber specimens per wood type. Spruce wood is particularly suitable for this purpose. As the sclerenchyma fibers in *Banksia* follicles, spruce secondary cell walls are a composite of cellulose, hemicelluloses, and lignin. Moreover, many fundamental structure-function relationships have been investigated on the basis of this sample material in the past.[97, 198, 199]

Experimental Parameters of the *P. abies* Fiber Tests

For these tests sample holders made of aluminum were used, similar to the ones in Fig. 11, at fiber gluing distances up to 800 μm . Metal sample holders provide higher dimensional stability in changing climatic conditions than the ones used for *B. attenuata* mesocarp fibers. Minimized holder deformation is fundamental for measurements of spruce fibers, where only small longitudinal deformation can be expected.[198] Moreover, the thermal bridge towards the cooler chamber housing has a smaller effect on the local climate at the specimen, compared to mesocarp samples, due to the longer test span of spruce fibers.

These lengths moreover enabled for a simpler wetting assembly. Liquid water was pumped to the specimen by a 1 ml syringe through a thin glass capillary, glued to the tip of a metal cannula. Also, the lower magnification of a conventional stereomicroscope (SZX7, Olympus, Tokyo, Japan), equipped with a digital camera (A 102f, Basler AG, Ahrensburg, Germany), was sufficient to operate the wetting steps, which allows for continuous optical distance measurement (videoextensometry).[179]

Spruce fibers' low hygroscopic deformation along the fiber axis is also the reason, why drying stresses were expected to be less pronounced compared to *B. attenuata* mesocarp. For this reason, the test procedure was changed to a mechano-sorptive stress-creep experiment. The fibers were tested in the same moistening sequence as *B. attenuata* mesocarp fibers, except cycles of stepwise drying were replaced by gradual drying.

Like before, throughout the first cycle the motor followed the fiber deformation for unimpeded shrinking and swelling. At the end of this cycle, the fibers were loaded to 15 mN at 60 % relative humidity. This loading was implemented into the experimental procedure as an alternative to the segment of stress generation upon drying for *B. attenuata* mesocarp fibers. Spruce fibers did not generate such stresses, in fact, their deformation behavior upon wetting and drying is more complex, as will be shown later. Through the cycles 2 to 4 the fibers' longitudinal deformation upon changing moistening conditions when loaded was tested, while unloading segments were added before wetting at stable 85 % relative humidity, and after drying at stable 35 % relative humidity. These unloading steps enable to estimate the impact of wetting and drying on the zero-load deformation of the fiber after each cycle. In cycle 5 the fibers were allowed to deform unimpededly again, before the final loading until breakage at stable 60 % relative humidity. The cross sections of the fibers were cut plane with a scalpel after the experiment and imaged in an environmental scanning electron microscope, using the low vacuum mode at a pressure of 0.75 Torr and an acceleration voltage of 5 kV (ESEM Quanta 600 FEG, FEI, Hillsboro, OR, USA). For stress calculation, the cross-section area was measured with ImageJ (version 1.53c), excluding the cell lumen.

Results and Discussion of the *P. abies* Fiber Tests

The tests of spruce fibers in cyclically changing moistening conditions have fundamental explanatory value about the experimental setup used for *B. attenuata* mesocarp fibers. For this reason, and due to the main focus of the present work on the *Banksia* pericarp structure and function, their results will be presented and discussed within this method section, rather as an immediate assessment of the experiment than an anticipated reflection of measurements.

The strain measurements of wood fibers were performed both optically and by motor displacement to estimate differences between the two methods. Such an approach was not possible for the *B. attenuata* mesocarp fibers, where the strain was

solely calculated based on the motor displacement, since the high magnification of the digital microscope was necessary to operate the wetting setup. It only allowed to record single images at specific steps. Due to the differences in initial sample lengths between *B. attenuata* mesocarp (150 μm to 200 μm) and spruce compression wood fibers (up to 800 μm) the absolute motor displacements during a whole experiment were similar (Fig. 15, 16). The reason for the comparability of the longitudinal deformation of these different samples lies in the high cellulose tilt angles of spruce compression wood (between 25° and 50° [94, 97]), and their loading. Strain values of spruce compression wood fibers, based on the motor displacement, show only slight differences from the videoextensometry (Fig. 15, 16). The strain determination for *B. attenuata* mesocarp fibers, solely based on motor displacement data, is therefore maintainable.

In contrast, spruce normal wood fibers are known to possess small cellulose tilt angles and hence small longitudinal deformation is expected.[120] This is reflected in the diagrams of Fig. 17 A. Furthermore, the strain–time diagram shows pronounced differences between video– and motor–displacement based strains, due to an increasing effect of errors, like motor hysteresis, at small displacement.

Such variations rule out strain determination solely based on the motor displacement for short fibers with low deformation. For them it would be indispensable to combine high magnification optics, needed for the experimental operation, with precise videoextensometry as it is already available for lower magnifications. At higher absolute deformation, like found in *B. attenuata* mesocarp fibers and spruce compression wood, strain values based on motor displacement represent the material behavior with better approximation.

Spruce branch compression wood fibers, where the cellulose tilt angle can exceed 40° [94, 97], show pronounced longitudinal swelling upon humidification (Fig. 15). Constant loading of such fibers by 15 mN leads to increasing strain—a relation amplified by cyclically changing moistening states, as common for lignified fibers.[200] The 15 mN pre–load caused different stress levels in the fibers due to different cross–section areas. Interestingly, these specific stress levels caused distinct differences in the strain curves. The single fiber loaded to stresses below 40 MPa still contracts upon drying (Fig. 15 A). Two other fiber specimens each exhibiting a stress of more than 50 MPa lose their contraction potential upon drying (Fig. 15 B, representative).

A similar relation can be observed for spruce stem compression wood with a cellulose tilt angle of approx. 26° . [97] While two fibers are still able to contract upon drying (stress: 40 MPa, Fig. 16 A, representative), another one elongates further at a stress level of approx. 80 MPa (Fig. 16 B). This behavior indicates progressing breakage of chemical bonds in the amorphous cell matrix, called “stick–slip mechanism” [201], facilitated in changing sorption conditions. [200, 202, 203]

In contrast, all tested spruce normal wood fibers contracted upon decreasing relative humidity (17 A, representative), but to a smaller extent than compression wood, due to the small cellulose tilt angle. [204, 205] As seen before for the compression wood fibers, this behavior can be related to the low stress, which the 15 mN pre-loading caused in the larger fiber cross sections. Possibly, the “stick–slip mechanism” would be induced only at higher stress levels. [201, 206]

Independently of the stress level, the fibers’ response to wetting is different between normal and compression wood. When humidified by liquid water both branch and stem compression wood expand (Fig. 15,16). Normal wood, in comparison, contracts upon wetting when unloaded (Fig. 17). In the first loaded moistening cycle such fibers expand when brought in contact with water. Throughout the subsequent cycles the fiber contracts upon wetting again, both in loaded and unloaded condition. These findings are only partly in accordance with former findings and modeled relations which only cover the unimpeded deformation of the fiber. [118, 119]

After the loaded moistening cycles all samples recover their strain partially in one cycle of unloaded wetting and drying. The final continuous loading at 60 % relative humidity after the creep segments shows common stress–strain curves and stiffness values [97] for all the tested spruce fiber types (Fig. 17 B). Maintaining the stiffness throughout creep experiments is common for lignified cells. [201] The stiffnesses of the samples are 30.1 GPa, 31.1 GPa, and 40.1 GPa for normal wood, 10.0 GPa, 12.3 GPa, and 13.2 GPa for stem compression wood, and 2.2 GPa, 4.9 GPa, and 5.0 GPa for branch compression wood.

Detailed conclusions about the behavior of spruce fibers can hardly be drawn, based on the small number of tested samples. However, the measurements indicate the potential of the method, as intended. Precise loading, moistening, and strain determination of single wood fibers opens up an entire field of experimental possibilities, enabling to examine modeled fiber cell wall behavior on the basis

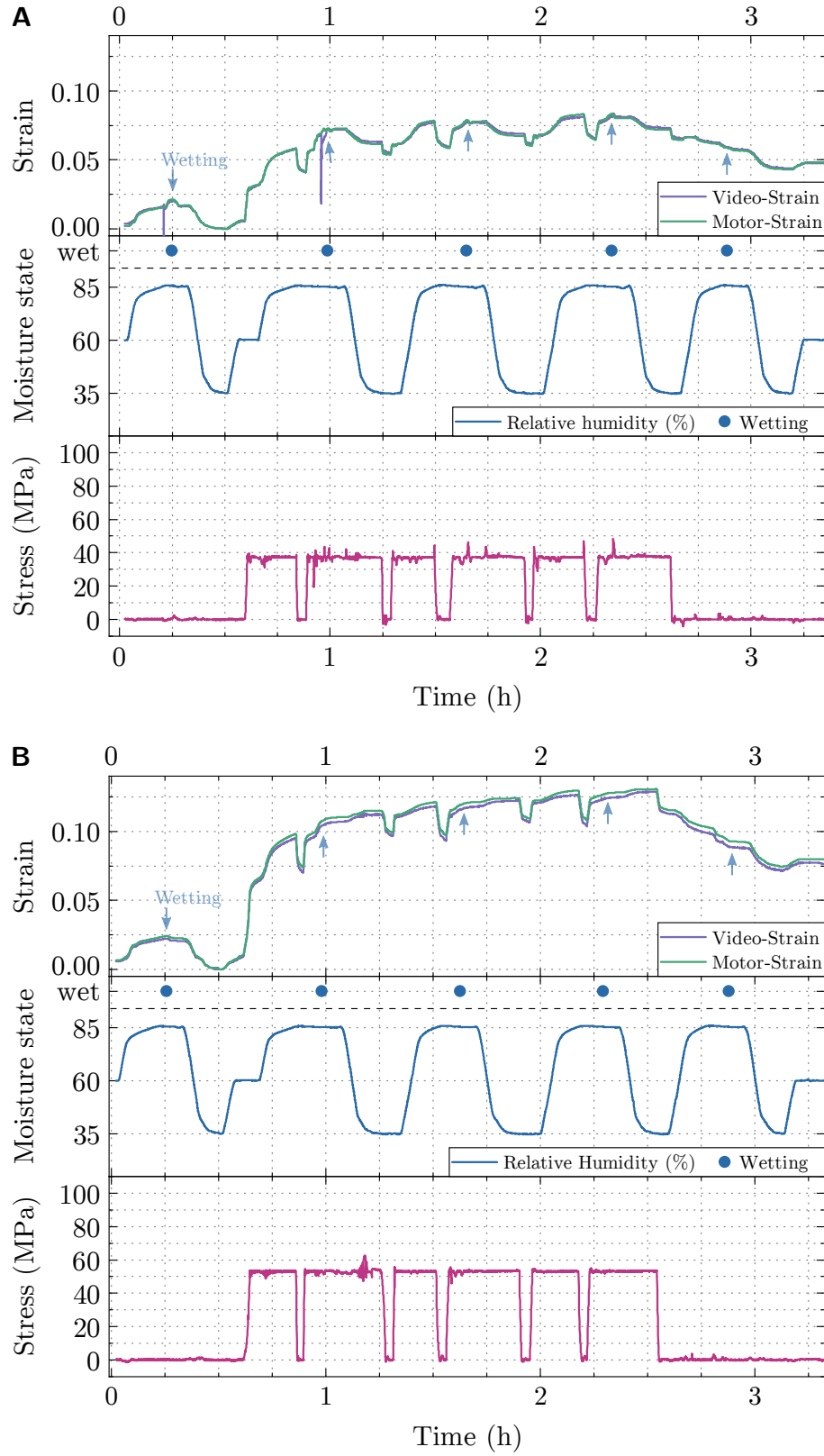


Fig. 15: Creep experiment of *Picea abies* single fibers. A and B: branch compression wood shows a different strain development at different stress levels.

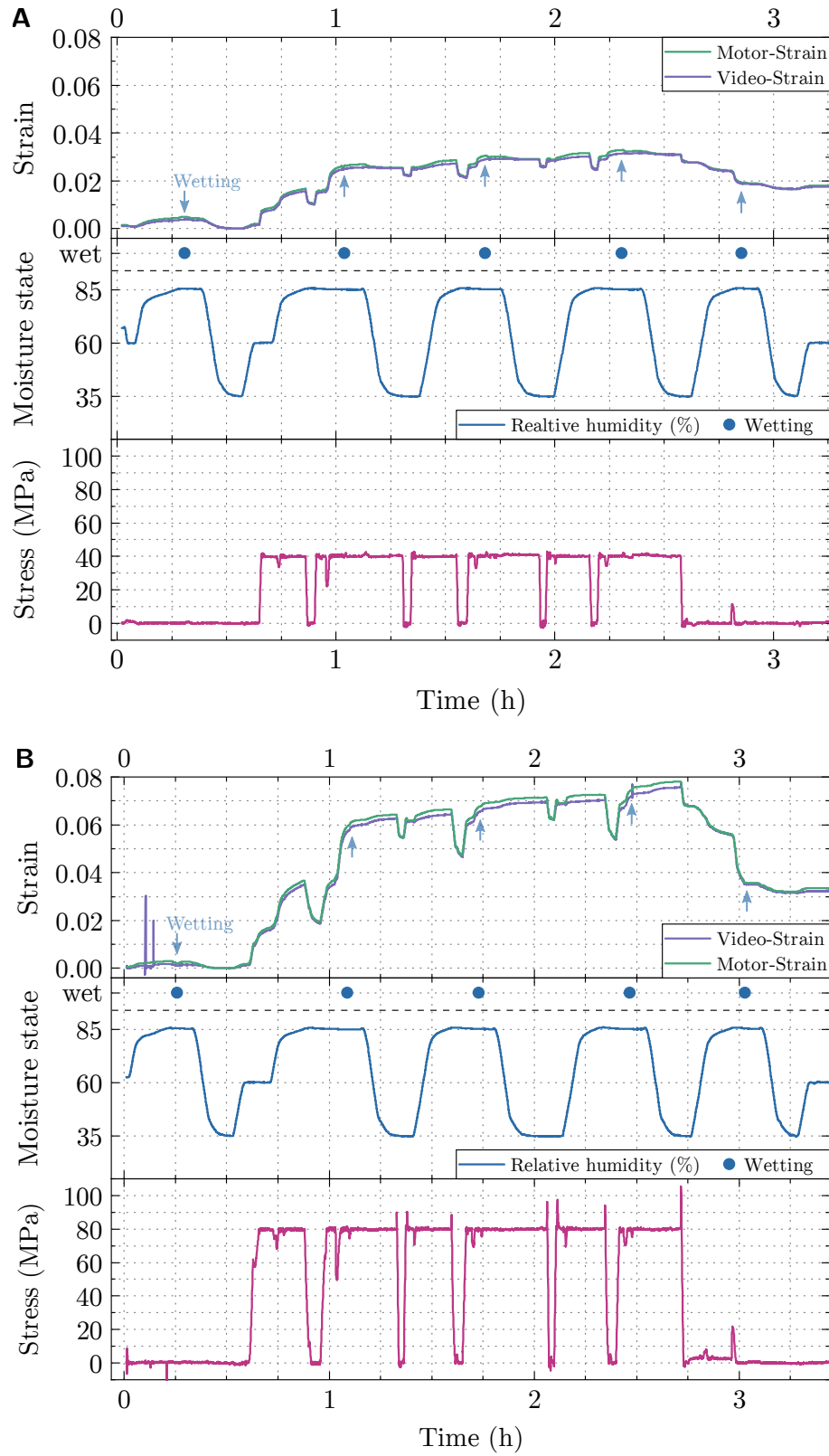


Fig. 16: Creep experiment of *P. abies* single fibers. A and B: stem compression wood shows a different strain development at different stress levels.

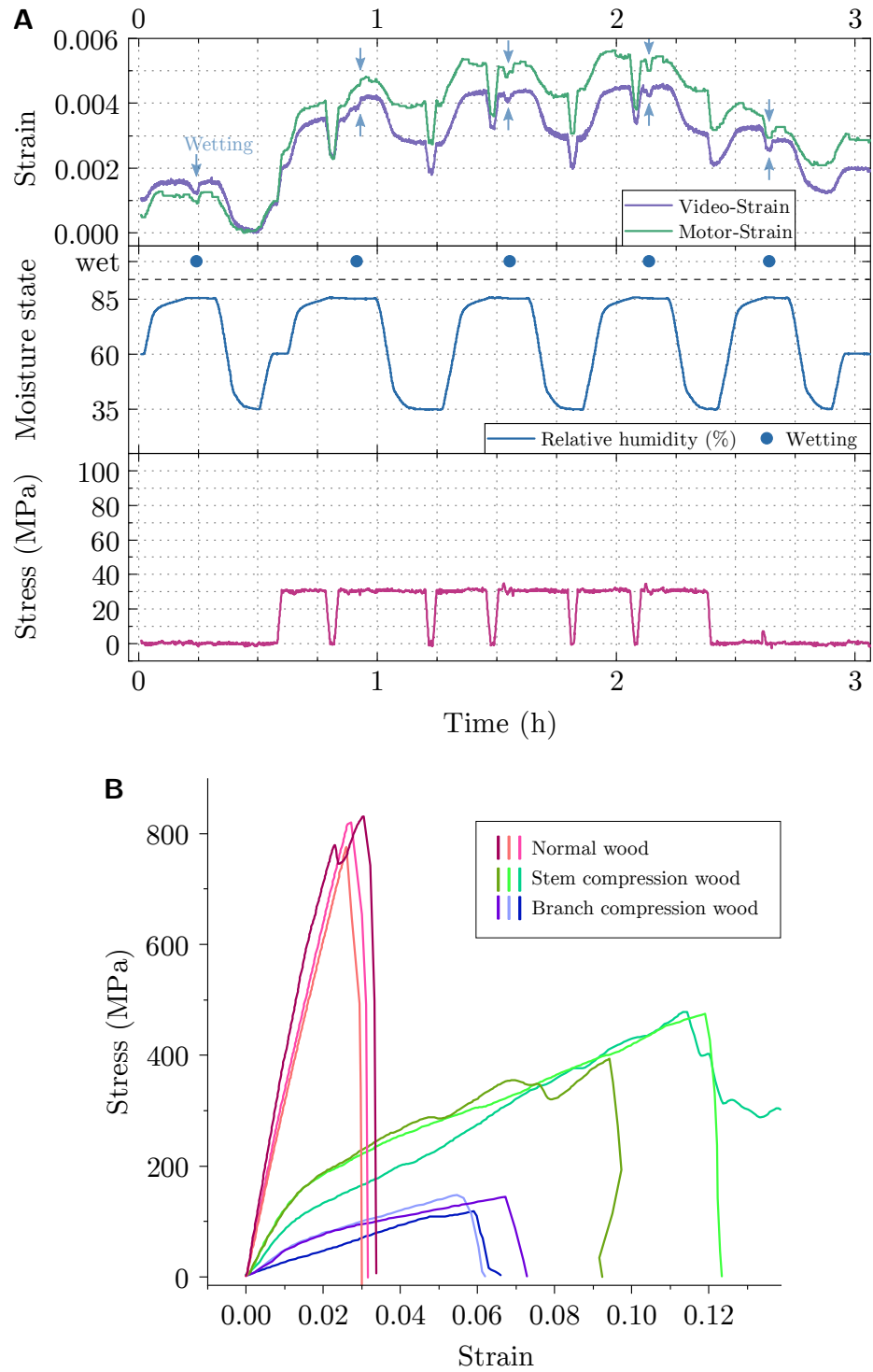


Fig. 17: Creep experiment of *P. abies* single fibers. A: representative measurement ($n = 3$) of normal wood. B: final loading of all spruce fiber samples.

of experimental results. Extensive investigation of several wood types in different loading scenarios and moistening regimes, however, entails significant experimental effort. The determination of control parameters requires patience and a sufficient number of pre-tests in the beginning. Later, the preparation and test of each actual fiber specimen takes more than one working day due to the multi-step mounting and long conditioning times ahead of the experiments. Moreover, it should also be mentioned that approx. one out of three to four measurements might fail at a point where the largest part of the work already had been done.

3.5 Numerical Modeling of a Bilayer System

The experimentally determined mechanical characteristics of the *B. attenuata* pericarp layers enable for a numerical modeling of the valve deflection in different scenarios. The basis of the model is a relation found for temperature sensitive metal bilayers.[207]

Their radius of the curvature of the strip (r) can be calculated by means of characteristic values of the material and its environmental conditions (Equ. 1) with the layer thickness (a), the coefficient of expansion (ε), and the elastic modulus (E), each for both layers 1 and 2, the thickness of the strip (h), increased temperature (T), and initial temperature (T_0).[207] Quotients are summarized to $\frac{a_1}{a_2} = j$ and $\frac{E_1}{E_2} = k$, respectively.[207]

$$\frac{1}{r} = \frac{6(\varepsilon_2 - \varepsilon_1)(T - T_0)(1 + j)^2}{h(3(1 + j)^2 + (1 + jk)(j^2 + (\frac{1}{jk})))} \quad (1)$$

Although the opening of the *B. attenuata* follicle is initiated by heat, the steps leading to seed release are driven by changes of the moistening conditions. For this reason the effect of temperature was excluded (Equ. 2).

$$\frac{1}{r} = \frac{6(\varepsilon_2 - \varepsilon_1)(1 + j^2)}{h(3(1 + j)^2 + (1 + jk)(j^2 + (\frac{1}{jk})))} \quad (2)$$

The calculation of the model beam curvature was based on the experimentally determined tissue properties within the *B. attenuata* pericarp. The properties of the outer mesocarp were implemented in the active layer 1 and, respectively, the properties of the endocarp in the resistance layer 2. The thickness of the two layers was determined by measurements on longitudinal sections of *B. attenuata* mesocarp and endocarp, formerly used for the investigation of the hygroscopic behavior. The interface between the model layers was set to the value of the center between endo-

carp and the inner mesocarp fiber bundle of these sections, resulting in an average thickness of $a_2 = 1.1$ mm for layer 2, an average thickness of $a_1 = 2.6$ mm for layer 1, giving an average total thickness $h = 3.7$ mm of the entire model beam.

For the partial deflection of the model beam, corresponding to the first opening step (*I*) of the follicle, the expansion coefficient of layer 1 was chosen from the experiment on stress generation and strain recovery (section 4.2.4) of outer mesocarp fibers from *B. attenuata*, as displayed in Fig. 24 B (dry length of mesocarp fibers as the difference between step 3 and step 5): $\varepsilon_{1I} = 0.94$. For the total deflection of the model, corresponding to the second opening step (*II*) of the follicle, the expansion coefficient of layer 1 was chosen analogously (dry length of mesocarp fibers as the difference between step 2 and step 3): $\varepsilon_{1II} = 0.79$. The expansion of layer 2 for both scenarios was rounded based on the experiment on hygroscopic deformation of *B. attenuata* pericarp tissue (section 4.2.1): $\varepsilon_2 = 1.00$. Results of the pericarp tensile stiffnesses served as elastic moduli (section 4.2.2, Fig. 22): $E_1 = 1.49$ GPa for layer 1 and $E_2 = 4.66$ GPa for layer 2.

4 Results and Discussion

4.1 Chemical Composition and Ultrastructure

Histological staining methods on thin pericarp cross sections were applied to reveal first details about endocarp and mesocarp, and the relation between layer structure and composition. Both staining protocols, the Wiesner and the Mäule method, result in gradually changing coloring between inner and outer mesocarp (Fig. 18 A, B). The Wiesner method with phloroglucinol–HCl shows a more pronounced staining of the inner mesocarp (Fig. 18 A). Outer fiber bundles show only little color. KMnO_4 –Tris–HCl staining of the improved Mäule method results in a strong coloring all over the mesocarp fiber bundles (Fig. 18 B), where outer mesocarp regions appear slightly pale, while the staining towards the inside of the follicle turns more into red. In comparison, the endocarp is rather homogeneously stained by both methods with a color comparable to the outer mesocarp fiber bundles. Only endocarp fibers close to the parenchymatic interface with the mesocarp show slightly intensified coloring.

Both the Wiesner and the Mäule method are related to lignin–units in plant cell walls.[76, 128, 129, 131, 132] The gradual coloring of the mesocarp due to these stainings makes compositional changes within the tissue likely. It particularly indicates for decreasing lignin S–unit proportions from inner to outer mesocarp regions.[129,

130, 132–134] Moreover, the Wiesner results can be related to diminishing amounts of G–units and cinnamaldehyde endgroups.[124, 129, 130] In the endocarp, the more pronounced staining of fibers towards the mesocarp indicate an increasing content of S units in this region.[129, 130, 132–134]

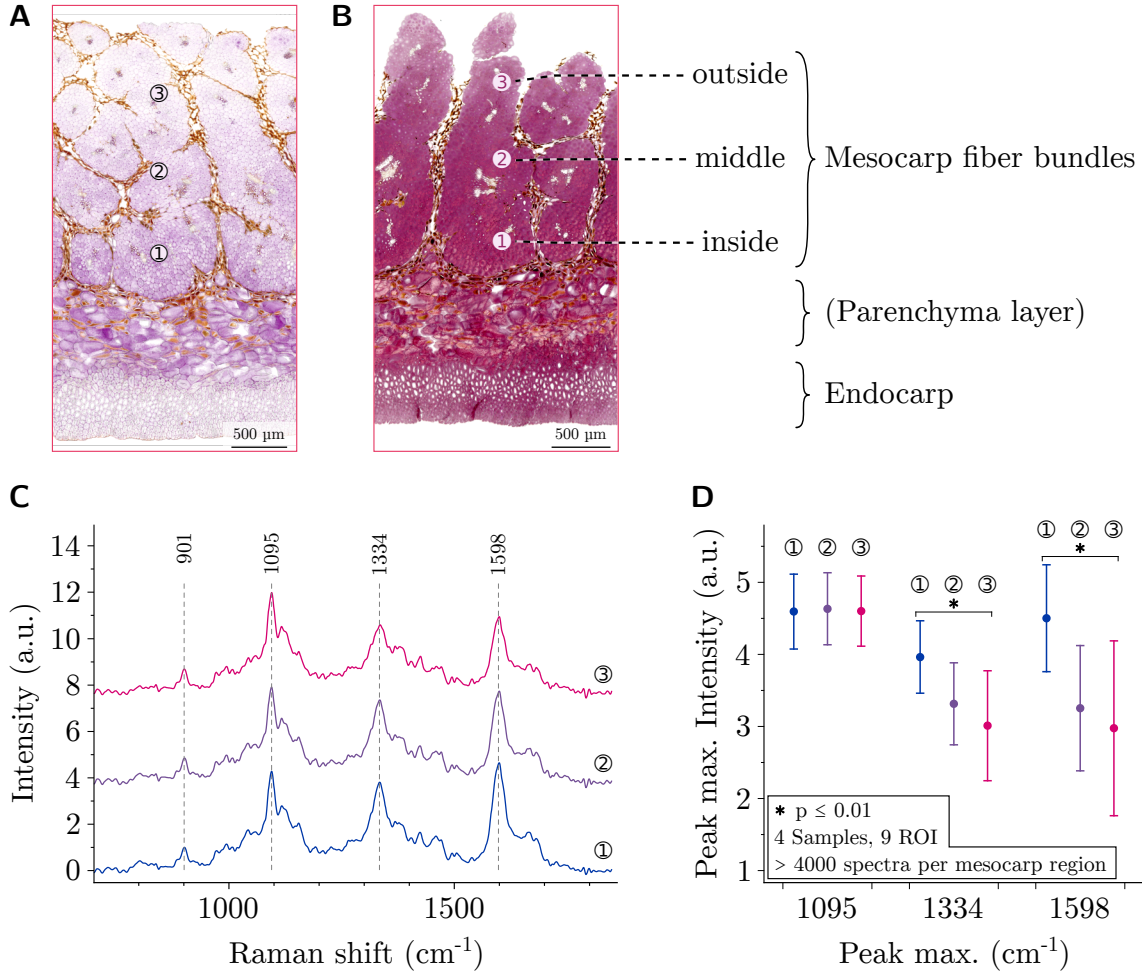


Fig. 18: Compositional changes within *B. attenuata* pericarp. A: transversal thin section, Wiesner staining. B: transversal thin section, Mäule-staining. C: representative Raman spectra of consecutive mesocarp fiber bundles. D: intensity differences of single peaks (arithmetic mean and standard deviation).

Raman spectroscopy indicates for differences in the amount of aromatic compounds over the thickness of the mesocarp as well (Fig. 18C, D, Tab. 1). The intensities particularly of the 1334cm^{-1} , and the 1598cm^{-1} peaks, decrease for fiber bundles towards the outside of the mesocarp (Fig. 18D; $p \leq 0.01$, Mood's Median Test, OriginPro 2021b). The 1598cm^{-1} peak is related to the aromatic ring stretching.[138, 142–145] Its intensity loss towards the outer mesocarp represents decreasing proportions of lignin units in general (Fig. 18D). The similar tendency

of the band at 1334 cm^{-1} confirms this observation and assigns the lignin loss particularly to the S units.[136, 137, 208] At the same time, the intensity of the strongly polarization-dependent cellulose-related peak at 1095 cm^{-1} does not show such a relation (Fig. 18 D; $p \leq 0.01$, Mood’s Median Test, OriginPro 2021b).[143, 147] It indicates consistent measurement and evaluation conditions—within the chosen regions of interest the transversal cellulose orientation is aligned with the polarization of the laser, set in the instrument.

Tab. 1: Raman peak intensities of *B. attenuata* (site 2) mesocarp ($n = 4$, arithmetic mean \pm standard deviation).

Peak position (cm ⁻¹)	Raman max. peak intensity (a.u)									n _{Spectra}
	Mesocarp inside (①)			Mesocarp middle (②)			Mesocarp outside (③)			
1095	4.59	±	0.52	4.63	±	0.50	4.60	±	0.49	4066
1334	3.98	±	0.50	3.33	±	0.57	3.02	±	0.76	4983
1598	4.50	±	0.74	3.25	±	0.87	2.98	±	1.21	4474

In comparison to changing relative intensities of peaks at 1334 cm^{-1} and 1598 cm^{-1} , no peak position shifts were detected between inner and outer mesocarp (Fig. 18 C). This indicates no changes in chemical conformation of the detected components over the mesocarp thickness. The chemical configurations of the related components, resulting in specific molecular vibrations detected by Raman spectroscopy, remain therefore constant over the mesocarp thickness.

Additionally to the experiments on the chemical composition, the tilt angle of cellulose microfibrils was investigated in detail within the *B. attenuata* pericarp, as endocarp and mesocarp were already found to be different in terms of their ultrastructure.[52, 54] Over the thickness of the mesocarp, consistent cellulose tilt angles can be observed, in contrast to compositional changes in the matrix of these lignified fibers. Polarized light, transmitted through the sample, is retarded similarly by all mesocarp fiber bundles along the microtome cutting lines (Y axis, Fig. 19 A). In comparison, the retardation of polarized light in the endocarp is smaller, resulting in a darker appearance (bottom of Fig. 19 A). There the retardation of polarized light is smaller than in the mesocarp. Provided that the cellulose crystallinity in mesocarp and endocarp is similar, it indicates for a strong shift of cellulose tilt angles between endocarp and mesocarp [151]—a result in accordance with former findings.[52, 54] Oval endocarp fibers towards the mesocarp appear slightly brighter

in Fig. 19 A and indicate larger cellulose tilt angles in this region compared to the inner edge of the pericarp.

These ultrastructural features were investigated in detail by TEM imaging of mesocarp tissue. The negative staining with KMnO_4 gives contrast between cellulose and lignin. Artifacts on the sections, largely found on post-stained sections [155, 166], could be avoided by a self-developed prestaining procedure, based on literature findings.[163, 165] The achieved contrast in *B. attenuata* mesocarp fibers was found to be lower than in spruce fibers, also investigated in the TEM, potentially due to different lignin binding sites. Still, the contrast upon KMnO_4 staining was more pronounced than for the other staining protocols, applied to mesocarp tissue, using the reagents uranyl acetate, lead citrate, and osmium tetroxide.[158, 164] The achieved contrast allowed for investigations of the cellulose orientation of mesocarp fibers in longitudinal sections (Fig. 19 E, F). This orientation was found to be perpendicular to the longitudinal axis (X), when determined in the center between two pits—radial channels, which serve for intercellular nutrient exchange in the living tissue (Fig. 19 E, F). The anisotropic periodic pattern of stained matrix and unstained cellulose regions in the TEM images becomes particularly visible by directional intensity peaks in reciprocal space, calculated by Fast Fourier Transformation. Azimuthal integration over the inner ring of these diffractograms shows peaks shifted by approx. 90° , compared to the longitudinal direction (Fig. 19 G, H). In immediate vicinity of the pits, cellulose microfibrils were found to show a rotational pattern. It might explain the variation found in wide-angle X-ray scattering patterns, presented in the past [52, 54], as pits occur in large number in mesocarp sclerenchyma fibers.

Although ultrathin sections used for TEM investigations comprise only a fraction of the cell wall thickness, they are still representative. Several longitudinal sections, taken in different positions of the secondary cell wall and also from different samples, gave similar results, when investigated in the TEM. The consistent circumferential pattern in the transverse section of a fiber from the inner mesocarp (Fig. 19 B) also indicates consistent circumferentially deposited cellulose microfibrils over the entire secondary cell wall thickness between lumen (Fig. 19 C) and middle lamella (Fig. 19 D). Together with the LC-PolScope retardance map, the TEM results exemplify the consistency of the perpendicular cellulose orientation with respect to the longitudinal X axis on two levels—widely within the a single fiber itself, but also over the entire mesocarp layer.

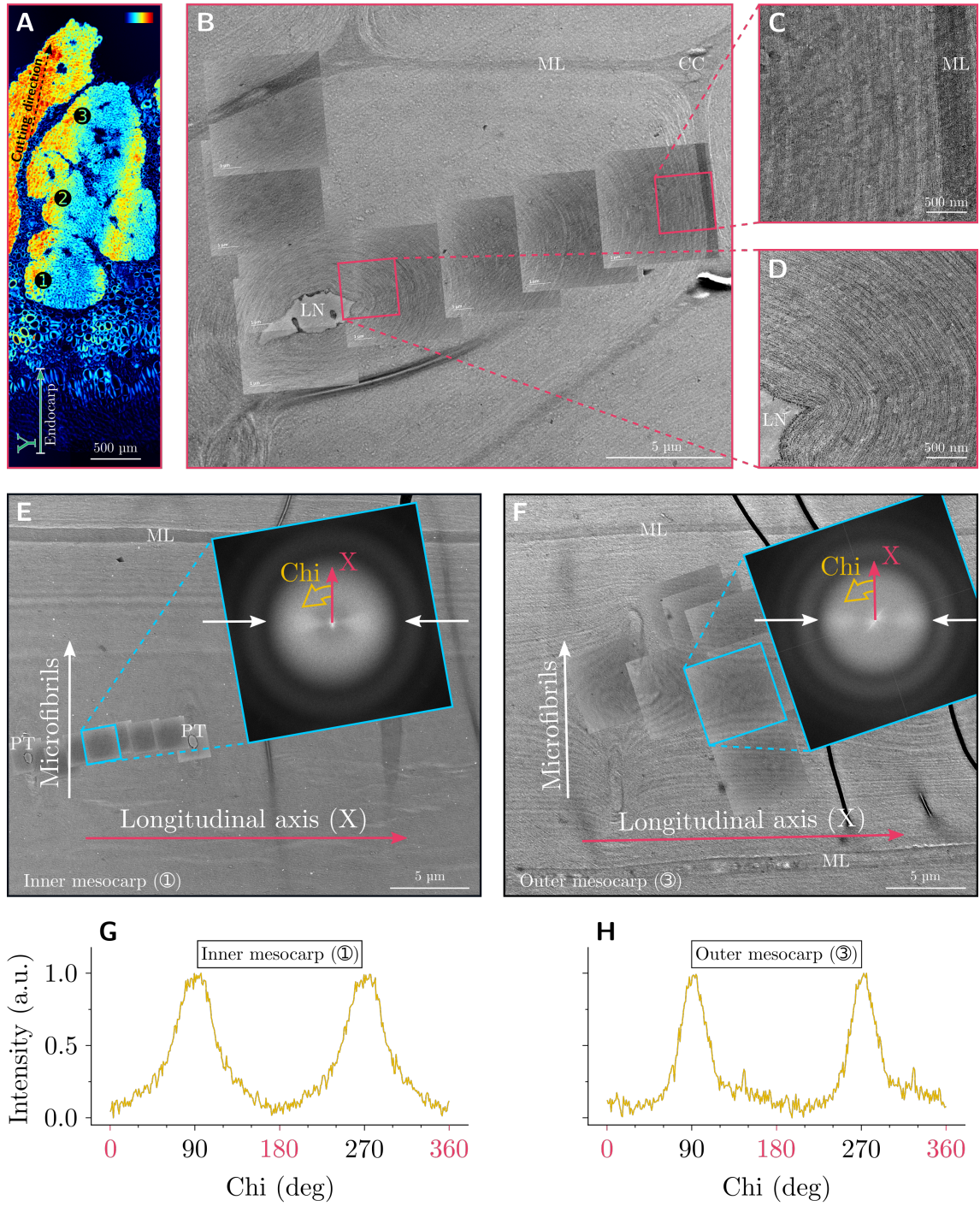


Fig. 19: Ultrastructure of *B. attenuata* mesocarp fibers. A: LC-PolScope retardance map over mesocarp and endocarp. B–D: TEM micrographs of a mesocarp fiber transversal section. B: overview. C: detail close to the middle lamella (ML). D: detail close to the lumen (LN). E, F: TEM micrographs of longitudinal sections: overview, stitched details, and diffractograms. G, H: azimuthal integration of the diffractograms (E, F), representing the cellulose orientation. E, G: inner mesocarp. F, H: outer mesocarp. CC: cell corner. PT: pit.

The ultrastructure of the *B. attenuata* mesocarp resembles cell wall characteristics found in the active layer of pine cones, even though on a lower order of magnitude. Structural features oriented rather perpendicularly to the longitudinal axis of the fiber, were also found in these examples by scanning electron microscopy.[22, 23] Similarly, the strong shift of cellulose tilt angles between endocarp and mesocarp indicates for a superordinate bi-layer structure of the *B. attenuata* pericarp. This finding is in accordance with former studies on *Banksia* follicles.[52, 54] Compared to lignified cells from trees and other arborescent plants, the cellulose orientation perpendicular to the longitudinal axis is remarkable. Reaction tissue of conifers hardly exceeds cellulose tilt angles of 45° , possibly due to its rather static function, compared to the active tissue of a fruit or cone.[94, 97]

Moreover, a subordinate compositional gradient within the thick mesocarp was found. The amount of S lignin units diminishes towards the outer mesocarp (Fig. 18 C). It is likely to cause an increase of the second matrix component of lignified cells in return, the hemicelluloses, as both cellulose orientation found by TEM and the intensity of the cellulose-related Raman peak at 1095 cm^{-1} are uniform over the mesocarp thickness. Changes in lignification can be mechanically relevant, as deformation due to water sorption or loading of the lignified cell wall takes place largely in the amorphous matrix.[110, 201, 209] It is the reason why the cellulose tilt angle has the major affect on the physical properties of lignified tissue, however, plants are able to achieve specific mechanical requirements by changes in the matrix composition.[210]

4.2 Hygromechanical Properties

4.2.1 Hygroscopic Deformation

From maturation over retention until release of the seeds, serotinous *B. attenuata* follicles pass through many cycles of changing environmental conditions over several years in the Mediterranean climate of Southwest Australia.[53] While the follicles remain stable over these multiple moistening cycles as long as they are closed, wetting and drying cycles lead to seed release, after the initial opening was triggered by heat exposure.[72] Since the follicle pericarp consists of layers with different structure and composition, the swelling properties are expected to vary between layers. Knowledge about the effect of wetting on the tissue dimensions, and also on the mechanical properties, is therefore of high concern.

The experimental deformation between wet ($\cong 1$) and dry state at 30 °C (relative humidity of the room between 41.5 % and 56.3 %) of *B. attenuata* pericarp tissue mirrors their structural and chemical characteristics (Fig. 20). The length of endocarp tissue in the longitudinal direction (X) remains almost constant upon drying (Fig. 20 A, Tab. 2, 3). Small longitudinal swelling has also been observed in numerous other plant tissues with small cellulose microfibril angles such as normal mature stem wood of conifers [113, 115, 120, 121] and can be related to the small tilt angle of the stiff cellulose microfibrils in the endocarp, as indicated by the LC-PolScope measurement (Fig. 19 A) and reported previously.[52, 54] In an isotropically swelling matrix, cellulose microfibrils lead to an anisotropic dimensional stabilization in the direction of their polymer chains.[118, 119] At the same time, the endocarp shows a stronger swelling and shrinkage in the transversal directions Y and Z for both site 1 and site 5 samples (Fig. 20 C, D). This shrinkage relation is in accordance with findings for conifer wood, too, where the soft and hygroscopic matrix gains importance on the transversal shrinkage for small cellulose tilt angles.[115, 118–120]

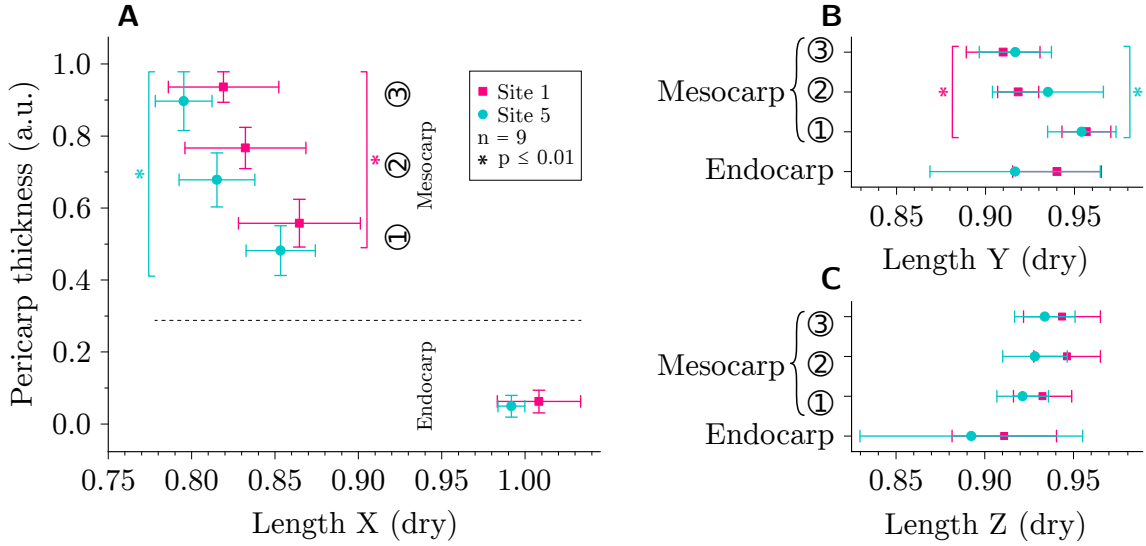


Fig. 20: Hygroscopic deformation of *B. attenuata* mesocarp and endocarp tissue. A: X-axis (longitudinal). B: Z-axis. C: Y-axis. Shown values: arithmetic mean and standard deviation.

Mesocarp tissue, in comparison, shrinks noticeably in the longitudinal direction (X). Compared to the wet state the length of dry outer mesocarp fiber bundles is 0.82 (site 1, arithmetic mean) and 0.80 (site 5, arithmetic mean) (Fig. 20 A). This pronounced longitudinal shrinkage can be related to the high cellulose tilt angles of the mesocarp layers, as shown with LC-PolScope and TEM investigations (Fig. 19). For tree wood, such a relation is documented up to cellulose tilt angles of approx. 45°, however, even the highest tilt angles only cause longitudinal shrinkage lower

than 4 %.[113, 115, 120, 121] Within the mesocarp, the hygroscopic and soft matrix has the major effect on the longitudinal shrinkage, while the stiffness of the cellulose microfibrils is not effective in this direction due to their perpendicular orientation.[118, 119] The extent of this hygroscopic deformation of *B. attenuata* mesocarp fiber bundles is similar to the active sclerenchyma tissue of pine cones, which also shows structural cell wall features perpendicular to the longitudinal fiber axis.[23, 25]

Towards the inner mesocarp, the *B. attenuata* fiber bundles show less shrinkage ($p \leq 0.01$, Kruskal–Wallis–ANOVA, OriginPro 2018). This tendency can be related to compositional changes in the matrix of the lignified tissue, as cellulose tilt angles are similar throughout all regions of the mesocarp (Fig. 19). It is expected that an increase of hydrophobic lignin units, which possibly leads to a loss in the content of hydrophilic hemicelluloses, could cause the difference. A similar relation was found between hardwoods and softwoods.[149] At similar densities, hardwoods showed a larger volumetric shrinkage upon drying, which was related to their higher hemicellulose and lower lignin content, compared to softwoods.[149]

Apparently, the values of site 5 tissue are generally lower than those of site 1. Statistically, this difference can be verified only for the outer mesocarp region on p -level 0.05 (Whitney–Mann–Test, OriginPro2018). These results were obtained from nine different sections, cut from three different follicles of both, site 1 and site 5. A clearer estimation of this effect would be possible by the comparison of more measurements on different follicles. Allocation of the longitudinal deformation values to their actual measurement positions shows a non-linear dependency between shrinkage and normalized pericarp thickness (Fig. 20 A).

Transversal shrinkage of mesocarp tissue, in comparison, is less pronounced than in the longitudinal direction and on average less than for the endocarp, particularly in the Z direction. It is in the range of the transversal shrinkage found in lignin-rich softwood compression tissue.[115, 120] Considering cellulose microfibrils aligned exactly with this plane, these high values might be surprising. However, while small cellulose tilt angles lead to hygroscopic–dimensional stability of the longitudinal fiber axis, a perpendicular–circumferential cellulose orientation can have this effect in the transverse plane only partially. Secondary cell walls are deposited layer-wise.[7, 74] Regardless of microfibril tilt angles, cellulose and matrix compounds alter radially (Fig. 19 B). The hydrophilic matrix therefore maintains hygroscopic deformation of the cell wall in the transverse plane, although circumferential cellulose microfibrils

might limit its extent, which could lead to shrinkage stresses in the cross section. This perspective is supported by transversal shrinkage differences between the three mesocarp regions in the Y direction for both site 1 and site 5 ($p \leq 0.01$, Kruskal–Wallis–ANOVA, OriginPro 2021b, (Fig. 20 B). Decreasing shrinkage from outer to inner mesocarp can be related to the changing proportions of the matrix components, similarly to the longitudinal direction.[149] It is in accordance with findings on lignin–affected transversal shrinkage of spruce wood at homogeneous cellulose orientation.[115] However, it remains obscure, why the increase in lignin units does not reflect on the mesocarp shrinkage in the transversal Z–direction (Fig. 20 C).

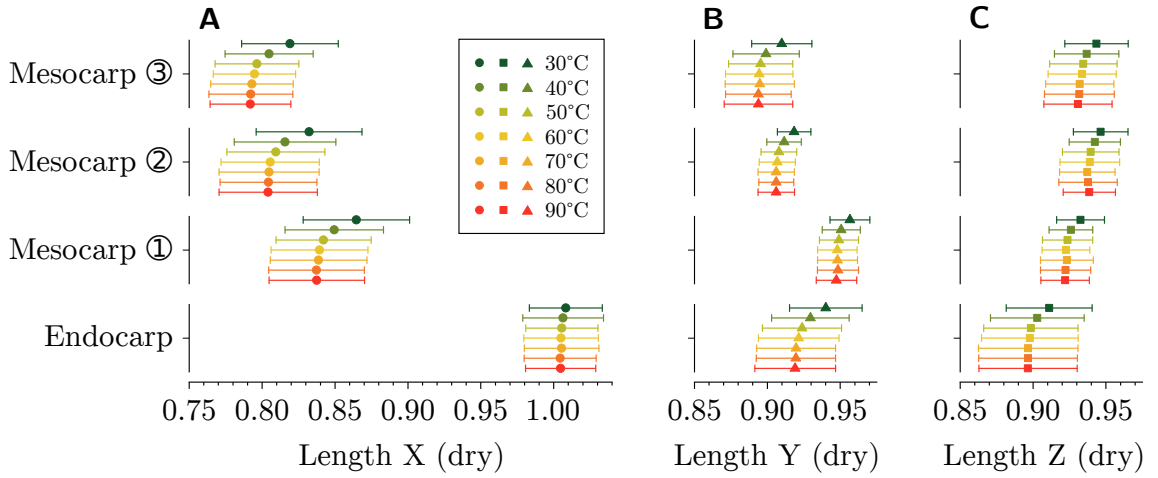


Fig. 21: Deformation of *B. attenuata* site 1 mesocarp and endocarp tissue upon heating in steps of 10 K from 30 °C to 90 °C. A: X–axis (longitudinal). B: Z–axis. C: Y–axis. Shown values: arithmetic mean and standard deviation. $n = 9$.

Stepwise heating of dry sections up to 90 °C affected the tissue deformation partially, as shown exemplarily for site 1 pericarp tissue (Fig. 21, Tab. 2; site 5: Tab. 3). Even though the data quality allows rather for coarse approximations than for clear statements, the longitudinal direction (X) of endocarp tissue appears to remain unaffected by increasing temperatures, especially between 30 °C and 50 °C, whereas mesocarp fiber bundles shrink further. In both transverse directions (Y and Z) these tendencies are even less pronounced and apparently similar in mesocarp and endocarp.

Although these results hardly allow any conclusions to be drawn, the described tendencies match the observations for dry and wet tissue at 30 °C and the explanations given to it. Upon heating the relative humidity around the sample decreased.[211] The moisture content of the lignified fibers established an equilib-

rium with the environmental humidity [108, 212–214]; desorption of water molecules caused further shrinkage.[196, 215, 216] Heating in the dry state at constant room humidity leads to further drying, which amplifies the shrinkage, determined between dry and wet state. The moisture content of the lignified tissue, however, decreases only by less than 4 % between 30 °C and 90 °C, at a relative humidity in the room of approx. 50 %, based on relations found for wood.[108, 213]

Tab. 2: Hygroscopic and hygrothermal deformation of the *B. attenuata* (site 1) pericarp layers (n = 9).

	T (°C)	State	Length (a.u., arithmetic mean \pm standard deviation)			
			Endocarp	Mesocarp inside (①)	Mesocarp middle (②)	Mesocarp outside (③)
X-axis	30	dry	1.008 \pm 0.025	0.865 \pm 0.037	0.832 \pm 0.036	0.819 \pm 0.03
	40	dry	1.006 \pm 0.028	0.849 \pm 0.034	0.816 \pm 0.035	0.805 \pm 0.03
	50	dry	1.006 \pm 0.025	0.842 \pm 0.033	0.809 \pm 0.034	0.796 \pm 0.03
	60	dry	1.005 \pm 0.026	0.839 \pm 0.033	0.806 \pm 0.034	0.795 \pm 0.03
	70	dry	1.005 \pm 0.026	0.839 \pm 0.033	0.805 \pm 0.034	0.793 \pm 0.03
	80	dry	1.004 \pm 0.025	0.837 \pm 0.033	0.804 \pm 0.033	0.792 \pm 0.03
	90	dry	1.005 \pm 0.024	0.838 \pm 0.033	0.804 \pm 0.034	0.792 \pm 0.03
	30	wet	1.000 \pm 0.000	1.000 \pm 0.000	1.000 \pm 0.000	1.000 \pm 0.00
Y-axis	30	dry	0.940 \pm 0.025	0.957 \pm 0.014	0.918 \pm 0.012	0.910 \pm 0.02
	40	dry	0.930 \pm 0.027	0.951 \pm 0.013	0.912 \pm 0.012	0.899 \pm 0.02
	50	dry	0.924 \pm 0.027	0.949 \pm 0.013	0.908 \pm 0.012	0.895 \pm 0.02
	60	dry	0.921 \pm 0.028	0.948 \pm 0.014	0.907 \pm 0.012	0.894 \pm 0.02
	70	dry	0.920 \pm 0.027	0.948 \pm 0.014	0.906 \pm 0.012	0.895 \pm 0.02
	80	dry	0.920 \pm 0.027	0.948 \pm 0.014	0.906 \pm 0.012	0.894 \pm 0.02
	90	dry	0.919 \pm 0.028	0.947 \pm 0.014	0.906 \pm 0.012	0.894 \pm 0.02
	30	wet	1.000 \pm 0.000	1.000 \pm 0.000	1.000 \pm 0.000	1.000 \pm 0.00
Z-axis	30	dry	0.911 \pm 0.029	0.933 \pm 0.016	0.946 \pm 0.019	0.944 \pm 0.02
	40	dry	0.903 \pm 0.032	0.926 \pm 0.015	0.942 \pm 0.018	0.937 \pm 0.02
	50	dry	0.899 \pm 0.032	0.924 \pm 0.017	0.940 \pm 0.019	0.935 \pm 0.02
	60	dry	0.898 \pm 0.033	0.923 \pm 0.016	0.939 \pm 0.020	0.934 \pm 0.02
	70	dry	0.897 \pm 0.034	0.923 \pm 0.018	0.937 \pm 0.019	0.932 \pm 0.02
	80	dry	0.897 \pm 0.034	0.922 \pm 0.017	0.938 \pm 0.020	0.932 \pm 0.02
	90	dry	0.897 \pm 0.034	0.922 \pm 0.017	0.939 \pm 0.018	0.931 \pm 0.02
	30	wet	1.000 \pm 0.000	1.000 \pm 0.000	1.000 \pm 0.000	1.000 \pm 0.00

Tab. 3: Hygroscopic and hygrothermal deformation of the *B. attenuata* (site 5) pericarp layers (n = 9).

	T (°C)	State	Length (a.u., arithmetic mean \pm standard deviation)			
			Endocarp	Mesocarp inside (①)	Mesocarp middle (②)	Mesocarp outside (③)
X-axis	30	dry	0.992 \pm 0.008	0.853 \pm 0.021	0.815 \pm 0.023	0.795 \pm 0.017
	40	dry	0.989 \pm 0.009	0.837 \pm 0.021	0.800 \pm 0.023	0.781 \pm 0.017
	50	dry	0.989 \pm 0.009	0.831 \pm 0.020	0.794 \pm 0.021	0.774 \pm 0.016
	60	dry	0.988 \pm 0.009	0.828 \pm 0.020	0.790 \pm 0.022	0.770 \pm 0.017
	70	dry	0.989 \pm 0.009	0.826 \pm 0.020	0.789 \pm 0.021	0.769 \pm 0.015
	80	dry	0.989 \pm 0.010	0.826 \pm 0.021	0.789 \pm 0.021	0.768 \pm 0.015
	90	dry	0.987 \pm 0.009	0.826 \pm 0.019	0.788 \pm 0.022	0.768 \pm 0.016
	30	wet	1.000 \pm 0.000	1.000 \pm 0.000	1.000 \pm 0.000	1.000 \pm 0.000
Y-axis	30	dry	0.917 \pm 0.048	0.954 \pm 0.019	0.935 \pm 0.031	0.917 \pm 0.020
	40	dry	0.908 \pm 0.050	0.950 \pm 0.019	0.928 \pm 0.031	0.917 \pm 0.033
	50	dry	0.903 \pm 0.050	0.948 \pm 0.019	0.925 \pm 0.031	0.914 \pm 0.034
	60	dry	0.902 \pm 0.052	0.948 \pm 0.020	0.924 \pm 0.032	0.914 \pm 0.033
	70	dry	0.900 \pm 0.051	0.947 \pm 0.019	0.923 \pm 0.032	0.912 \pm 0.034
	80	dry	0.900 \pm 0.051	0.947 \pm 0.019	0.923 \pm 0.032	0.912 \pm 0.033
	90	dry	0.899 \pm 0.051	0.948 \pm 0.020	0.923 \pm 0.032	0.913 \pm 0.033
	30	wet	1.000 \pm 0.000	1.000 \pm 0.000	1.000 \pm 0.000	1.000 \pm 0.000
Z-axis	30	dry	0.892 \pm 0.063	0.921 \pm 0.015	0.928 \pm 0.018	0.934 \pm 0.017
	40	dry	0.885 \pm 0.066	0.916 \pm 0.012	0.920 \pm 0.019	0.928 \pm 0.019
	50	dry	0.881 \pm 0.067	0.912 \pm 0.014	0.917 \pm 0.020	0.926 \pm 0.020
	60	dry	0.879 \pm 0.066	0.909 \pm 0.015	0.916 \pm 0.020	0.925 \pm 0.021
	70	dry	0.878 \pm 0.067	0.908 \pm 0.015	0.916 \pm 0.019	0.923 \pm 0.020
	80	dry	0.877 \pm 0.067	0.909 \pm 0.016	0.916 \pm 0.021	0.924 \pm 0.018
	90	dry	0.878 \pm 0.068	0.908 \pm 0.015	0.916 \pm 0.021	0.926 \pm 0.021
	30	wet	1.000 \pm 0.000	1.000 \pm 0.000	1.000 \pm 0.000	1.000 \pm 0.000

4.2.2 Tensile Stiffness

As expected by the shift of cellulose orientation between endocarp and mesocarp [52, 54], which is known to have a major effect on wood mechanics [97, 178], these tissue regions are different in terms of their mechanical properties, additionally to their characteristic hygroscopic deformation. Endocarp samples show an average tensile stiffness of 4.7 GPa in the dry state and 1.4 GPa in the wet state (Fig. 22, Tab. 4).

These values are higher than those of spruce branch compression wood (Fig. 22) and of poplar wood (dry state only).[217] Tensile tests of tissue strips might give different results than single fiber tests, as the stress distribution can vary on the sample surfaces, and cell walls might be incomplete due to cutting.[218] Consequently, the values of both approaches are not comparable, as can be seen by the example of spruce branch compression wood. The present stiffness values (Fig. 22, upper part), measured by means of tissue strips, is significantly lower than values for single fibers of spruce branch compression wood, found in the literature.[97]

Compared to tensile tests of conifer wood on two different length scales—above and below the method used in the present work—the stiffness of dry endocarp tissue is surprisingly low.[97, 219] It is similar to the values for the highest cellulose tilt angles recorded.[97, 219] Endocarp cellulose tilt angles, however, appear to be lower, based on wide-angle X-ray scattering [52, 54] and thus, a higher stiffness would be expected.[97, 178] One of the mentioned endocarp scattering patterns, however, is explicitly assigned to fibers close to

the inner cavity of the follicle.[52] Possibly, the cellulose tilt angles of endocarp fibers and their lignification are inconsistent over the layer thickness, as the retardation of polarized light (Fig. 19 A) and histological stainings indicate (Fig. 18 A, B). Both affect the mechanical properties of lignified tissue.[97, 150, 178, 210, 220] Conclusively, the tensile stiffness measured by means of endocarp tissue strips might contain various fiber properties. Structural–mechanical inhomogeneities within the endocarp could also explain the large variation of the data. Compared to the mesocarp and spruce branch compression wood the standard deviation is high, even for the low stiffness of wet tested endocarp (Fig. 22 A, Tab. 4).

Within the mesocarp, the tensile stiffness is similar between inner and outer fiber bundles. In the dry state, the average values of these regions are between 1.3 GPa and 1.5 GPa. In the wet state, the stiffness is significantly lower with average values between 70 MPa and 100 MPa. Mesocarp stiffness in both dry and wet state largely

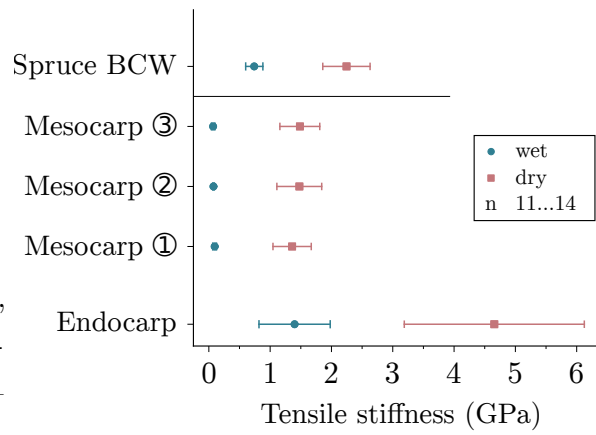


Fig. 22: Tensile stiffness of the *B. attenuata* pericarp layers and spruce branch compression wood (spruce BCW). Shown values: arithmetic mean and standard deviation.

undercut the known properties of lignified fibers found in wood, even those of reaction wood in spruce branches, irrespective of the different experimental approach of single fiber tests.[97] The microfibril orientation perpendicular to the longitudinal axis turns the stiffening effect of the cellulose into the transversal plane of the fibers. The tensile behavior of these fibers mirrors the properties of the lignified matrix, conclusively. Perpendicular to the cellulose orientation, the cell wall mechanics are dominated by the tensile properties of the hemicelluloses [92], which is more affected by moisture than lignin and cellulose.[100, 102, 103, 110] This explains, why the mesocarp stiffness is lower than the stiffness of lignin alone in both dry and wet state.[97, 102] It represents the mechanical properties of the hemicelluloses, where the dry stiffness is lower and the wet stiffness higher than literature values: 2 GPa and 20 MPa, respectively.[100] In contrast to increasing longitudinal shrinkage from inner to outer mesocarp fiber bundles (Fig. 20 A) the consistent tensile stiffness across these tissue regions is surprising. The changes of lignin S-unit proportions (Fig. 18) do not affect the mechanical properties, as measured in this experiment. Either this could be caused by the variation of the data, which makes stiffness differences insignificant. Or the observed compositional changes are too small to affect the tensile stiffness.

Tab. 4: Tensile stiffness of the *B. attenuata* (site 2) pericarp layers.

State	Tensile stiffness (MPa, arithmetic mean \pm standard deviation)												n
	Endocarp			Mesocarp inside (①)			Mesocarp middle (②)			Mesocarp outside (③)			
dry	4657	\pm	1468	1359	\pm	311	1477	\pm	366	1486	\pm	325	11–14
wet	1399	\pm	581	96	\pm	29	77	\pm	13	72	\pm	28	10–12

Even though the modulus-reduction in lignified cells upon wetting is well described, the stiffness loss for *B. attenuata* endocarp and meoscarp tissue is remarkable.[94, 219] Regardless the tensile test of tissue strips, which might average differences in the properties of single fibers, it illustrates a highly flexible structure when wet, which stiffens upon drying. In contrast to the chemical composition (Fig. 18) and to the hygroscopic deformation (Fig. 20), the tensile stiffness is constant over the entire thickness of the mesocarp.

4.2.3 Indentation Modulus and Hardness

Nanoindentation measurements draw a more detailed picture of the mechanics of the *B. attenuata* pericarp, as it allows to probe defined regions of a sample. It can

reveal differences in mechanical properties between neighboring cell walls or within layers. Although the indentation modulus does not represent the elastic modulus of a material, as it contains proportions of shear moduli, for example [221], it shows a dependency on the cellulose tilt angle of lignified cells.[192, 222] Moreover, the indentation hardness can give insights into the properties of the matrix compounds of such fibers.[192] Both cellulose orientation (Fig. 19) and chemical composition (Fig. 18) vary within the *B. attenuata* pericarp, which affects the nanoindentation data.

Indentation moduli (Fig. 23 A, Tab. 5) of dry mesocarp fibers show values ranging from 6.1 GPa to 8.8 GPa. Related to the three regions, inner, middle, and outer mesocarp, used in the experiments before, the average values of the fiber bundles are between 7.45 GPa and 7.89 GPa, however, differences between these tissue regions are not statistically significant in the dry state, measured on three different samples.

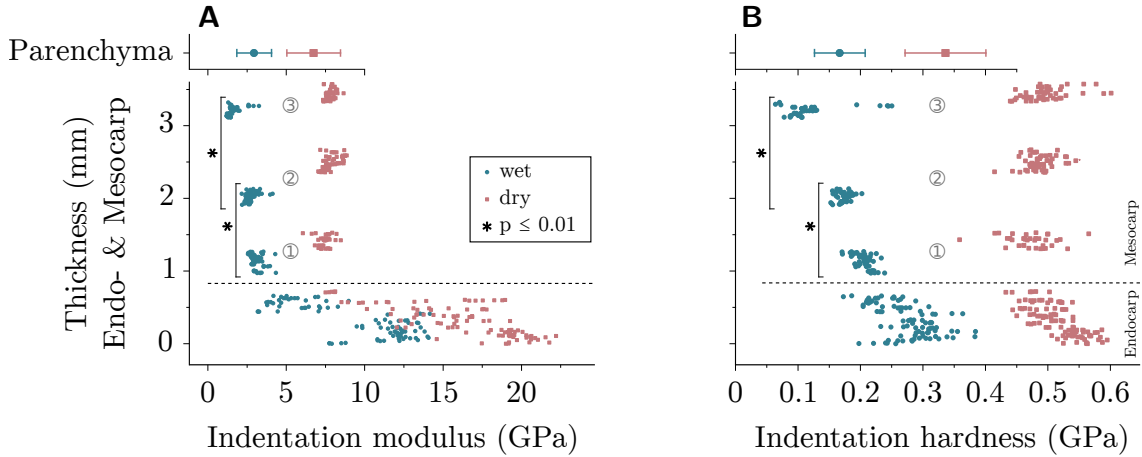


Fig. 23: Indentation properties of *B. attenuata* mesocarp and endocarp. A: reduced nanoindentation modulus (representative data set). B: nanoindentation hardness (representative data sets).

In comparison, reduced indentation moduli in the wet state decrease significantly ($p \leq 0.01$, Mann–Whitney–U–Test, calculated with Origin Pro 2018) from an average value of 3.12 GPa in the inner mesocarp over 2.75 GPa in the middle of the layer to 1.66 GPa in the outer mesocarp (Fig. 23 A, Tab. 5). Similarly the indentation hardness of wet samples significantly decreases from inner mesocarp (average 0.21 GPa) over a fiber bundle in the center of the layer (average 0.17 GPa), to outer mesocarp (average 0.12 GPa, Fig. 23 B, Tab. 5). In the dry state, the hardness of all mesocarp fiber bundles is uniform with averages between 0.48 GPa (inner mesocarp) and 0.49 GPa (outer mesocarp).

Indentation moduli of dry mesocarp cells, loaded along the longitudinal axis (X), are similar to those of conifer wood cell walls loaded at a high cellulose microfibril angle by tilting the sample with respect to the indentation axis.[223] Moreover, the experimental data of the mesocarp fibers confirm modeled values for dry lignified fibers with high cellulose tilt angle.[223] This model describes anisotropic indentation of lignified cell walls, taking into account the different mechanical properties of the cell wall components and the influence of the cellulose tilt angle.[221] The decrease of mesocarp indentation moduli due to wetting is more pronounced than assumed for the highest moisture contents by the model.[221] From inner to outer mesocarp, the indentation modulus decreases further, resulting in an increasing difference to the dry moduli, consistent over all mesocarp fiber bundles (Fig. 23 A). It is in accordance with diminishing lignin proportion towards outer mesocarp fiber bundles (Fig. 18) and moreover indicates for an increasing amount of hemicelluloses, in return.[100, 102, 103, 191] In the dry state, hemicelluloses can show an elastic modulus similar to lignin.[100, 102, 103] Moistening reduces the elastic modulus of hemicelluloses significantly, by approx. two orders of magnitude, in contrast to the rather hydrophobic lignin.[100, 102, 103] Therefore, a higher lignin proportion is likely to lead to a smaller modulus reduction by wetting in the inner mesocarp. Increasing proportions of hemicellulose provide a similar stiffness to outer mesocarp regions in the dry state, in contrast to a sole lignin reduction, which would cause decreasing moduli in both wet and dry state.[191] Moreover, an increasing amount of hemicelluloses enables for a more drastic flexibilization of outer mesocarp fiber bundles in the wet state [103], in contrast to altered ratios of the lignin units, which would not affect the mechanical properties of lignified cell walls.[217] Compared to the reduction of indentation modulus of spruce adult wood upon wetting, the differences determined for *B. attenuata* mesocarp are rather low, possibly due to high cellulose tilt angles, compared to approx. 10° of the spruce fibers.[190]

The indentation hardness of the mesocarp shows a similar relation between dry and wet state from inner to outer fiber bundles (Fig. 23 B, Tab. 5). In the dry state, the indentation hardness is consistent over the thickness of the mesocarp, whereas it decreases from inner to outer mesocarp regions when wet. Like the indentation modulus, the hardness is affected by changes in the matrix of lignified cell walls, too, which already were found affecting the indentation modulus (Fig. 23 A).[224] The combination of both modulus and hardness draws the picture of a *B. attenuata* mesocarp, which is particularly flexible and soft in the outer regions, where larger longitudinal hygroscopic deformation occurs (Fig. 20 A). This dependency broadens

the insights gained by the tensile tests (Fig. 22), where no differences were found between mesocarp tissue regions. It moreover fits the gradual increase of longitudinal hygroscopic shrinkage (Fig. 20 A), related to compositional changes of the matrix (Fig. 18). Upon drying, however, the entire mesocarp from inner to outer fiber bundles becomes homogeneously hardened and stiffened (Fig. 23). This relationship is essential for seed retention and release of serotinous *Banksia* follicles, as will be discussed below.

Parenchyma tissue in between mesocarp fiber bundles shows indentation properties in the same order of magnitude like mesocarp sclerenchyma (Fig. 23). While hardness and reduced modulus of these cell walls are lower in the dry state, their mechanical properties in the wet state are similar to the fibrous tissue. However, the parenchyma is mechanically less relevant than the mesocarp fiber bundles. Its effective resilience can be estimated lower due to its thin cell walls.[7] Upon the hygroscopic tissue shrinkage (Fig. 20) it can absorb stresses by deformation in between the sclerenchyma tissue regions.

Endocarp fibers show a large variety of nanoindentation moduli with lower values in the wet than in the dry state (Fig. 23 A, Tab. 5). Near the edge of the endocarp towards the parenchymatic intermediate layer and the mesocarp, indentation moduli reach down to the values of the most inner mesocarp fiber bundle: 7.5 GPa for dry and 3.2 GPa for wet tissue. These values increase strongly towards the inner edge of the pericarp with highest values for cells near the seed cavity: 22.2 GPa in the dry and 14.2 GPa in the wet state. The indentation hardness of endocarp tissue develops respectively—from minima at the endocarp–mesocarp interface (dry: 0.43 GPa, wet: 0.17 GPa) to maxima at the inner pericarp edge (dry: 0.60 GPa, wet: 0.38 GPa, Fig. 23 B, Tab. 5). Such tendencies could not be observed before by tensile tests of larger tissue strips (section 4.2.2). However, the changes in indentation moduli and hardnesses over the endocarp thickness underpin the assumption, that the comparably low endocarp stiffness and the high deviation, determined by tensile tests, (Fig. 22) reflects a variety of different properties from inner to outer endocarp fibers (section 4.2.2).

Spearman correlation coefficients between the indent's location within the width of the endocarp and the reduced indentation modulus are -0.73 for the dry and -0.62 for the wet state. High indentation moduli can also be found in more outer areas of the endocarp, as well as low moduli occur in more inner regions, too. The

indentation hardness correlates with the location of the indent by a coefficient of -0.74 in the dry state and 0.45 in the wet state (Spearman correlation, calculated with Origin Pro 2021b, $p \ll 0.01$, Fig. 23 B).

The strong decline of indentation moduli over the endocarp towards the interface with the mesocarp is in accordance with observations in the histological results (Fig. 18 A, B) and the LC-PolScope measurement (Fig. 19). High indentation moduli near the edge of the endocarp towards the follicle's inside indicate for higher proportions of cellulose and a small tilt angle of its microfibrils.[190, 222–225] Rapidly decreasing moduli towards the parenchymatic interface with the mesocarp can be caused by a combination of both increasing lignin content (Fig. 18 A, B) and rising cellulose microfibril tilt angle (Fig. 19 A) within the endocarp.[221, 223, 225]

Even though the indentation hardness of endocarp tissue declines in the same manner as the indentation modulus, its reduction towards the parenchymatic interface with the mesocarp is less pronounced (Fig. 23 B). This indicates the cellulose tilt angle to be the major influence on the endocarp gradient, as the cellulose orientation has a strong effect on the indentation modulus, while the hardness is largely influenced by the matrix properties.[192, 222] In contrast, the difference between dry and wet mesocarp hardness is even clearer than the difference between dry and wet modulus—at a constant cellulose tilt angle. It indicates for the shift in matrix composition [192], as the indentation hardness of lignified tissue shows a strong dependency on the wetting state of the cell wall, too.[226]

In terms of the overall *B. attenuata* pericarp mechanics and the follicle opening, the gradual transition between endocarp and mesocarp properties is indispensable. The endocarp is the resistance layer and therefore responsible to counter the shrinkage of the mesocarp longitudinally, in order to cause a deflection of the overall structure. Resistance, however, is mechanically necessary only on the edge of the seed cavity, whereas large stiffness and hardness over the entire endocarp thickness would impede bending. More flexible and softer fibers towards the mesocarp reduce internal stresses between the resistant part of the endocarp and the active fiber bundles of the mesocarp. Gradually decreasing modulus and hardness in the endocarp is therefore essential for both long-term stability and functionality of the pericarp.

Tab. 5: Reduced nanoindentation modulus (E_r) and hardness (H) of the *B. attenuata* (site 2) pericarp layers (one representative sample out of four, arithmetic mean \pm standard deviation / minimum ... maximum).

	State	Endocarp	Mesocarp inside (①)			Mesocarp middle (②)			Mesocarp outside (③)		
E_r (GPa)	dry	7.50 ... 22.20	7.45	\pm	0.45	7.89	\pm	0.51	7.80	\pm	0.29
	wet	3.19 ... 14.16	3.12	\pm	0.40	2.75	\pm	0.39	1.66	\pm	0.47
H (MPa)	dry	433 ... 595	476	\pm	32	486	\pm	23	494	\pm	40
	wet	173 ... 384	206	\pm	14	173	\pm	11	119	\pm	45

4.2.4 Stress Generation and Strain Recovery

Outer mesocarp tissue of *B. attenuata* shows a considerable dimensional response to wetting and drying (section 4.2.1). Moreover, its mechanical properties are affected most of all mesocarp fiber bundles by humidification (section 4.2.3). The environmental conditions of a serotinous follicle change many times over the years between seed maturation, initial follicle opening, and final seed release.[53] Therefore, the response of the outer mesocarp, which is apparently the “most active” of all the pericarp layers, to moisture was investigated in detail. In a tensile test experiment with cyclically changing moistening levels between the wet state and 35 % relative humidity, the dynamic deformation and static stress generation upon drying was precisely measured. The fiber behavior upon drying was of particular interest, as plant cells develop in the wet state, and they dry when disconnected from the plant’s metabolism.[7] The environmental conditions of the experiment were similar to the natural climate in Southwest Australia—conditions which facilitate the *B. attenuata* follicle opening.[54, 72, 197]

Humidity changes led to remarkable longitudinal swelling and shrinkage of outer mesocarp fibers, when allowed to deform unimpededly (Fig. 14, 24 A, 25 A, Tab. 6). Their contraction developed continuously from the wet state over six defined steps of drying to 35 % relative humidity with a max. strain of 0.22 (arithmetic mean; Fig. 25 A, 24 B, steps 1–2, Tab. 6). This maximum shrinkage is similar to the values measured on outer mesocarp tissue sections (Fig. 20 A), however it largely exceeds unimpeded hygroscopic deformation of spruce branch compression wood (Fig. 15). Stepwise drying at fixed maximum length of the unloaded wet state causes drying stresses in the fiber (Fig. 24 A, 25 A), culminating at 40.7 MPa (arithmetic mean; Fig. 25 A, 24 B steps 3–4, Tab. 6) in dry condition at 35 % relative humidity.

Subsequent unloading at the same humidity level releases the strain only partially; the fiber length decreases only to a strain of 0.15 (arithmetic mean; Fig. 24 B steps 4–5, Tab. 6). Further steps of unimpeded hygroscopic deformation upon wetting and drying lead to a length recovery of the fibers. While the strain in wet and dry condition is higher than before the segment of stress generation it approximates its initial value with each cycle of wetting and drying (Fig. 24 B steps 6–11, Tab. 6).

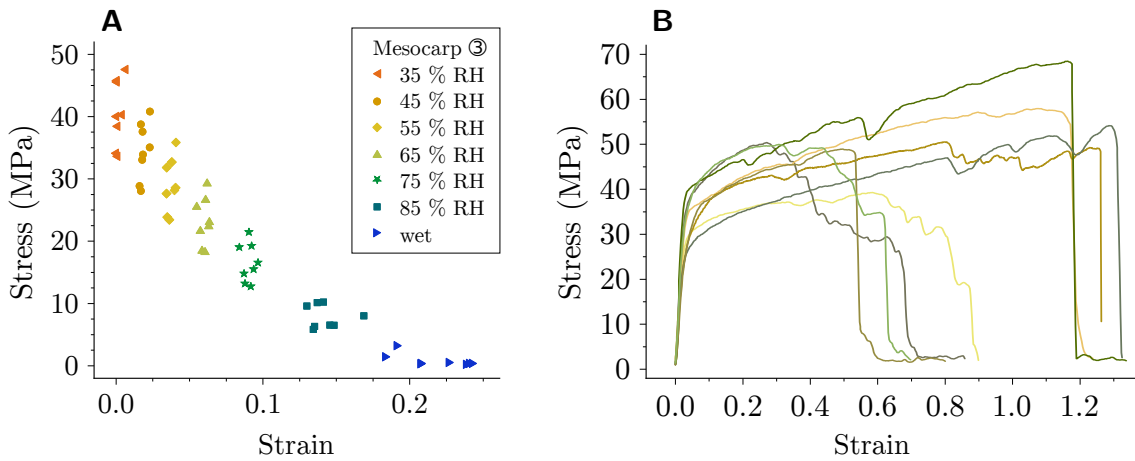


Fig. 25: Stress–strain dependency of *B. attenuata* outer mesocarp ($n = 8$). A: summary of stress and strain from impeded and unimpeded drying. B: final loading at 60 % relative humidity.

Both continuous shrinkage of unimpeded fibers and stress generation at fixed wet length is the result of progressing water desorption upon drying. The water content within a lignified cell wall after disconnection from the plant’s metabolism establishes an equilibrium with the environmental humidity.[107, 108, 213] Decreasing relative humidity leads to desorption of water molecules from hydroxy groups in the matrix and in amorphous cellulose regions.[80, 107, 110, 111, 196] Conversely to adsorption and swelling, matrix and cellulose move closer together upon water desorption, as they link again by more hydrogen bonds, resulting in shrinkage of the cell wall.[80, 110, 111] It leads to the pronounced longitudinal deformation of *B. attenuata* mesocarp fibers, laterally to the cellulose microfibrils (Fig. 19 F).

Upon impeded drying from the wet state, water molecules desorb from hydroxy groups, too. However, the matrix compounds and the cellulose microfibrils are not able to move closer together. Presumably, fewer hydrogen bonds can be established. In consequence, stresses develop. The exact molecular mechanism behind the stress development, and also behind strain retention and recovery after impeded shrinkage,

remains unknown. However, this essential relation is highly relevant, not only for the *B. attenuata* mesocarp stress generation, but also for lignified tissue in general.

This mechanism, observed in single fibers from the outer mesocarp, is fundamentally different from another mechanism plants use to “pull” stems or roots into specific directions.[227] The reaction tissue of deciduous trees relies upon an additional cell wall layer, which contains large proportions of cellulose at small tilt angles.[228–230] In between the cellulose microfibrils of this “gelatinous layer”, small proportions of pectins and hemicelluloses are discontinuously deposited.[227, 231] As the water content decreases, these matrix compounds keep larger spaces in some regions, which cause maturation strain due to microfibrillar bending.[227, 232] The longitudinal deformation of this tension is maximum 1.5 % [228, 230]—a fraction of the longitudinal shrinkage found in *B. attenuata* outer mesocarp fibers. However, the reaction tissue is likely to cause significant stresses, too, as the deformation occurs in the direction of the stiff cellulose microfibrils.[100]

During the final loading at a relative humidity of 60 %, the *B. attenuata* mesocarp fibers show an average stiffness of 1.3 GPa with a standard deviation of 0.2 GPa (Fig. 25 B). This value is in accordance with results from tensile tests of mesocarp tissue strips (section 4.2.2). Even though tests with different sample geometries are usually not directly comparable [218], the elastic properties of such mesocarp fibers seem to be maintained over several cycles of impeded and unimpeded wetting and drying. Stiffness recovery after loading cycles is a known property of lignified fibers, even for stress scenarios beyond the yield point (Fig. 25 B).[201]. There, however, irreversible deformations can occur.[201] A similar relation was found in the spruce tensile tests (Fig. 17 B).

Tab. 6: Hygroscopic deformation and stress generation of *B. attenuata* (site 2) outer mesocarp (③) single fibers (n = 8, arithmetic mean \pm standard deviation).

Mositening state	Stress (MPa)			Strain (a.u.)		
wet	0.87	\pm	1.03	0.217	\pm	0.023
85 % RH	7.91	\pm	1.85	0.143	\pm	0.012
75 % RH	16.58	\pm	3.11	0.090	\pm	0.004
65 % RH	23.13	\pm	3.86	0.060	\pm	0.003
55 % RH	29.01	\pm	4.29	0.037	\pm	0.003
45 % RH	34.51	\pm	4.52	0.019	\pm	0.003
35 % RH	40.68	\pm	5.28	0.002	\pm	0.002

4.3 Numerical Modeling of the Pericarp Deformation

The theoretical model for metal bilayer strips [207] enables a largely simplified curvature calculation based on experimental data. For a first scenario, related to the initial opening of the *B. attenuata* follicle, a small deformation of the active layer results in a curvature of the entire model strip of $r_I^{-1} = 0.024 \text{ mm}^{-1}$. In a second scenario, which is related to the complete opening of the follicle, the deformation of the active layer is changed for a higher value. Consequently, the curvature of the strip increases to $r_{II}^{-1} = 0.084 \text{ mm}^{-1}$.

These bending scenarios are illustrated in Fig. 26. The reciprocal curvature value equals the bending radius for each state, which is $r_I = 41.9 \text{ mm}$ (first scenario), and $r_{II} = 12.0 \text{ mm}$ (second scenario). As the pericarp of each follicle is partly embedded in the cone, the bending radius was only applied to 60 % of the strip's length. For a comparison with the natural system, the related opening steps of *B. attenuata* are displayed by an image series of a longitudinal cut through a follicle (Fig. 26).

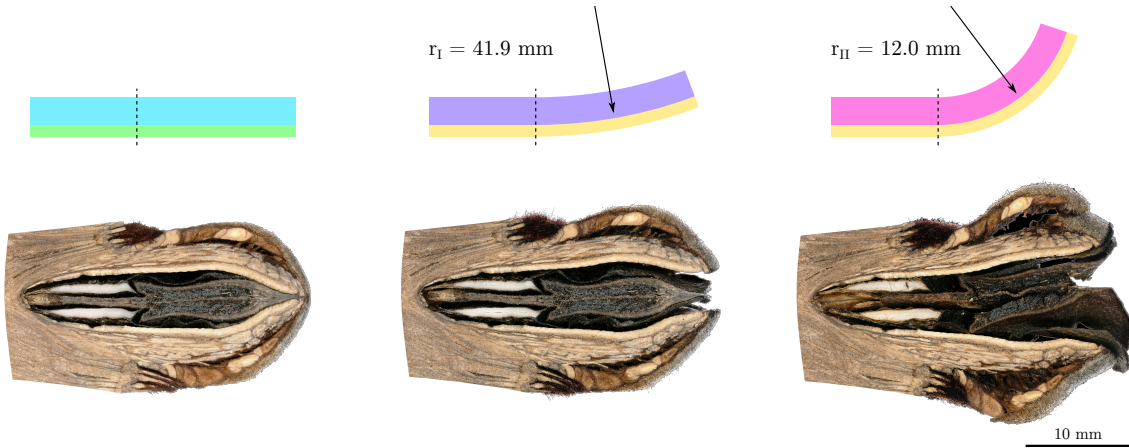


Fig. 26: Comparison between the calculated curvatures and a natural sample of *B. attenuata*. Left: all layers are fully expanded; corresponds to the pericarp at maturation. Middle: partial release of the shrinkage capacity in the active layer causes bending around a large curvature radius (r_I). Right: complete release of the shrinkage capacity reduces the radius of the curvature (r_{II}).

The curvature of the model seems to exceed that of the natural sample in both cases, though. On one hand, the reason for the obvious difference in bending might lay in the simplicity of the straight model beam and its strict bilayered division with a homogeneous modulus and strain rate in the thick active layer, set to the maximum value of the outer mesocarp. In comparison, the *B. attenuata* pericarp shows a distinct curvature and gradual transitions of physical layer properties (Fig. 20, 23).

On the other hand the comparison with cut pericarp valves can be misleading, as the follicle opening of *B. attenuata* follows an asymmetric crack (Fig. 2 C, D), which is hard to display perspectively on one single cut plane. Moreover, the opening relies on an intact fibrous structure, which is clearly damaged in the case shown in Fig. 26.

Conclusions about the *B. attenuata* follicle opening based on this strictly bi-layered model can hardly be drawn. The natural example is more complex in structure and mechanical properties and it is questionable if the calculated bi-layer model would actually remain intact upon bending, if built physically. While the *B. attenuata* pericarp shows gradual property shifts within endocarp and mesocarp, the bi-layer model comprises only two contrary layers, which might delaminate due to interfacial stresses. For a general remark, however, this model should be sufficiently reliable: the two-step strain release (initial partial shortening, followed by complete shortening of the active layer) can be a suitable mechanism for two-step deflection scenarios, as found in *B. attenuata* follicles.

4.4 Follicle Opening Explained by Pericarp Mechanics

The pericarp of *B. attenuata* follicles appears to be functionalized first on a superordinate level due to drastic differences between mesocarp and endocarp, and second on a subordinate level due to gradual property shifts within the layers. On the superordinate level, low cellulose tilt angles in the endocarp cause longitudinal stability. Fibers close to the inner follicle cavity are particularly stiff in order to counter the longitudinal deformation of the mesocarp. The constantly high cellulose tilt angles of mesocarp fibers, in contrast, lead to large longitudinal deformation of the tissue upon drying and cause significant longitudinal shrinkage stresses.

On the subordinate level, the mechanical properties of endocarp cell walls drastically diminish towards the interface with the mesocarp, as nanoindentation showed (Fig. 23). Presumably, this gradual decrease is caused by increasing cellulose tilt angles towards this interface, which are indicated in the LC-PolScope retardance map (Fig. 19 A). This gradient is essential for the bending of the pericarp. A continuously stiff endocarp layer, as assumed based on tensile tests of tissue strips (Fig. 22), would impede the bending to a larger extent. High stiffness is only needed at the edge of the endocarp to counter the longitudinal shrinkage of the mesocarp and to cause pericarp bending instead of longitudinal endocarp compression. Additionally, softer and more flexible endocarp fibers at the interface with the mesocarp can absorb deformation stresses and thus prevent delamination of the structure.

Within the mesocarp, a gradual increase of the longitudinal shrinkage from inner to outer fiber bundles (Fig. 20 A), caused by changes in the matrix composition of the lignified fibers (Fig. 18), increases the bending moment of the pericarp. Moreover, it reduces stresses within the mesocarp and towards the endocarp. Residual stresses can deform thin-walled parenchymatic cells in between fiber bundles and in the thick intermediate layer between mesocarp and endocarp (Fig. 18 A, B).

Indentation properties of mesocarp fibers showed an increasing difference between dry and wet state from inner to outer fiber bundles (Fig. 23). This tendency was related to changes in the matrix composition (Fig. 18). It was interpreted as an increase of flexibilization and softening upon wetting towards the outside of the pericarp, whereas drying leads to homogeneous stiffening and hardening of all mesocarp fiber bundles (Fig. 23). This relation is important for the seed retention of *B. attenuata* follicles beyond the initial opening upon heat exposure, and for the delayed seed release following bushfires.

Cyclic tensile tests of single fibers from the outer mesocarp reveal the mechanical relevance of this water-dependent stiffening and hardening for the *B. attenuata* opening process. The stress generation upon impeded drying from the wet state (Fig. 25 A, 24 B, step 3–4) precisely describes the initial loading of the pericarp valve at maturation, which was anticipated before, based on the strong shift of cellulose tilt angles between endocarp and mesocarp.[52, 54] However, as the tested fibers were dried before, it is only partially possible to compare their hygroscopic shrinkage with the first drying at maturation. After the first drying of lignified cell walls the accessibility of hydroxy groups is limited, compared to the never-dried state.[233] This accessibility can be restored by wetting under vacuum conditions, different from the atmospheric pressure of the present experiment.[233, 234]

At elevated temperatures the mesocarp tissue contracts further against the dimensionally stable endocarp (Fig. 21 A), resulting in a stress increase (Fig. 25 A). It contributes to the initial follicle opening upon heat exposure. Once the follicle opens, these stresses lead only to a partial deflection of the pericarp valves (Fig. 2 B–D). The largest proportion of the mesocarp’s longitudinal contraction potential is retained (Fig. 24 B, step 4–5), as the tissue stiffened and hardened during the impeded drying from the wet state (Fig. 22, 23). Possibly, this effect could be comparable with the “embrittlement” observed for softwood pulp fibers upon restrained drying.[177] However, only its effect on the tensile strength is documented for this material,

while strain retention was not investigated.[177] In the *B. attenuata* follicles, partial contraction of mesocarp fibers causes only little valve deflection (Fig. 2 C). It is the crucial functionality of *B. attenuata* seed protection to inhibit the full release of its motion potential throughout the bushfire. Subsequent wet–dry cycles increase the contraction of single mesocarp fibers in each drying step (Fig. 24 B, step 6–11) due to alternating swelling – shrinking, flexibilization – stiffening, and softening – hardening (Fig. 21 A, 22, 23). In the follicle it causes progressing deflection of the whole pericarp and crack propagation in both the junction and the fracture zone (Fig. 5, 2 C, D) by each drying cycle. Eventually, it leads to seed release, as soon as the gap between both valves is sufficient.

B. attenuata's degree of serotiny depends on the climatic conditions the plants grow in (Fig. 1).[53, 54] These differences of the follicles—higher opening temperatures at hotter growing sites—are related to geometric variations of the pericarp.[54] At the same time, significantly higher longitudinal shrinkage of outer mesocarp at the southernmost growing site 5 (Fig. 20 A) generates higher prestresses (Fig. 25 A) in the less curved pericarp valves.[54] It is likely to facilitate spontaneous follicle opening due to sun exposure in these cooler regions where annual rainfall is higher [54], as the mesocarp contraction and therefore stress generation (Fig. 25 A) increases when heated above 30 °C (Fig. 21). At the northernmost growing site 1 (warmer and drier), the lower longitudinal mesocarp shrinkage (Fig. 20 A) in combination with a more pronounced pericarp curvature [54] generates less stresses upon this hygrothermal drying (Fig. 25 A). Follicles from these regions are able to withstand higher temperatures without opening. Compared to the heat-induced weakening of the endocarp [54], the mesocarp stress increase commences ahead, as the active layer is spatially closer to the heat source. It facilitates the initial opening before the endocarp loses its resistance, particularly upon sudden temperature maxima, like immediate flame exposure in bushfires.

The results of the presented investigations give insights into the mechanical background of the *B. attenuata* follicle opening and shed light on stability and functionality of plant organs in general. Pine cones, mentioned already in the beginning of this work, were found to show a high longitudinal deformation of fibers in the active scale layer upon changes in moisture content [22, 25]. This deformation is likely to cause hygroscopic loading of the fibers in the active layer, similar to *B. attenuata* mesocarp fibers. The high pericarp thickness of *B. attenuata* follicles is partially comparable with the *Ruellia* fruits, mentioned in the beginning. There the presence

of an intermediate layer in between active and resistance layer increases the overall thickness, leads to a higher bending moment and raises the elastic energy of the pericarp, although its mechanical resilience is neglectable.[18] Additionally, it might serve the interfacial stress reduction—a similar function as assumed for the property gradients within endocarp and mesocarp of *B. attenuata*, and the thin-walled parenchymatic tissue in between fiber bundles.

The example of the well studied *Ruellia* fruit opening [18] lets surmise how a detailed modeling of the *B. attenuata* follicle opening could explain the interrelation of structural features and hygromechanical properties, in order to reach concurrent dynamic and static function. While present biomimetic concepts focus predominantly on motion, an extension of these approaches by the characteristic of stability is highly relevant. It can lead to specialized solutions for complex issues, as the long-term retention and two-step release of *Banksia* seeds in fire-prone environments shows. Structural and mechanical background knowledge, like presented in this work, is only the starting point for the transfer of a natural principal into innovative materials.[235–237]

5 Conclusion

Exploring the natural phenomenon of *Banksia*’s seed retention and release from a material’s perspective required comparisons of different hierarchical levels of the follicle valves. Adapted and newly developed methods enabled extensive compositional, structural, and mechanical investigations. The experiments revealed the characteristics behind protectiveness and motion of the pericarp.

The functionalization of *B. attenuata*’s follicles was found to rely on sophisticatedly combined cellulose tilt angles and matrix variations between and within mesocarp and endocarp. It leads to hygroscopic deformation and drying stresses of the active mesocarp against the resistant endocarp, driving seed pod opening and valve deflection. These stresses due to decreasing moisture content could be precisely determined on the level of single fibers.

Moreover, seed retention of *B. attenuata* follicles beyond bushfires and subsequent release after rain could be related to strain retention and recovery of the mesocarp after impeded drying and rewetting. This fundamental principle was found to interact with the large pericarp thickness, which ensures protectiveness of the seeds for

many years. The shrinkage behavior and moisture-dependent mechanical properties are fine-tuned within the layers to prevent delamination and ensure long-term stability.

Considering the large span of functionalization of *Banksia* follicles from the nanometer scale of cellulose microfibrils, up to climatic gradients, hundreds of kilometers long, the exceptional nature of this reproduction strategy becomes apparent. In addition to the broader relations of the *Banksia* seed dispersal, which have been extensively studied in the past, the detailed approach of the present work supplements the understanding of the natural phenomenon of serotiny. Moreover, the relations found for the *B. attenuata* pericarp might be relevant for other thick layer structures found in nature. The characteristics of mesocarp fibers, additionally, lead to more profound insights into the mechanics of lignified cells in general. Ultimately, the present work facilitates biomimetic innovations, based on the principle evolved by *Banksia* plants for life continuation.

References

- [1] Balas, B. and Momsen, J. L. (2014): Attention “blinks” differently for plants and animals. *CBE—Life Sciences Education* 13(3): 437–443. DOI: 10.1187/cbe.14-05-0080.
- [2] Balding, M. and Williams, K. J. H. (2016): Plant blindness and the implications for plant conservation. *Conservation Biology* 30(6): 1192–1199. DOI: 10.1111/cobi.12738.
- [3] Wandersee, J. H. and Schussler, E. E. (1999): Preventing plant blindness. *The American Biology Teacher* 61(2): 82–86. DOI: 10.2307/4450624.
- [4] Giesecke, T. et al. (2019): Postglacial change of the floristic diversity gradient in Europe. *Nature Communications* 10(1): 1–7. DOI: 10.1038/s41467-019-13233-y.
- [5] Feurdean, A. et al. (2013): Tree migration-rates: narrowing the gap between inferred post-glacial rates and projected rates. *PLoS ONE* 8(8). Ed. by Nogues-Bravo, D.: e71797. DOI: 10.1371/journal.pone.0071797.
- [6] Fei, S. et al. (2017): Divergence of species responses to climate change. *Science Advances* 3(5): e1603055. DOI: 10.1126/sciadv.1603055.
- [7] Evert, R. F. (2006): *Esau’s plant anatomy*. 3rd ed. Hoboken: John Wiley & Sons: 601. DOI: 10.1002/0470047380.
- [8] Darwin, C. and Darwin, F. (1880): *The power of movement in plants*. London: J. Murray: 592. DOI: 10.1017/cbo9780511693670.
- [9] Schwendener, S. (1874): *Das mechanische Princip im anatomischen Bau der Monocotylen mit vergleichenden Ausblicken auf die übrigen Pflanzenklassen*. Leipzig: Wilhelm Engelmann: 207.
- [10] Hildebrand, F. (1873): Die Schleuderfrüchte und ihr im anatomischen Bau begründeter Mechanismus. *Jahrbücher für wissenschaftliche Botanik* 9: 235–275.
- [11] Steinbrinck, C. (1906a): Über Schrumpfungs- und Kohäsionsmechanismen von Pflanzen. *Biologisches Centralblatt* 26(20): 657–677.
- [12] — (1906b): Über Schrumpfungs- und Kohäsionsmechanismen von Pflanzen. *Biologisches Centralblatt* 26(21): 721–744.
- [13] Dickinson, M. H. (2000): How animals move: an integrative view. *Science* 288(5463): 100–106. DOI: 10.1126/science.288.5463.100.
- [14] Zimmermann, A. (1883): Über den Zusammenhang zwischen Quellungsfähigkeit und Doppelbrechung. Version 1. *Berichte der Deutschen Botanischen Gesellschaft*: 533–540.
- [15] Zohary, M. and Fahn, A. (1941): Anatomical-carpological observations in some hygrochastic plants of the oriental flora. *Palestine Journal of Botany, Jerusalem Series* 2: 125–131.
- [16] Fahn, A. (1947): Physico-anatomical investigations in the dispersal apparatus of some fruits. *Palestine Journal of Botany, Jerusalem Series* 4: 36–45.

- [17] Tripp, E. A. (2007): Evolutionary relationships within the species-rich genus *Ruellia* (Acanthaceae). *Systematic Botany* 32(3): 628–649. DOI: 10.1600/036364407782250625.
- [18] Witztum, A. and Schulgasser, K. (1995): The mechanics of seed expulsion in acanthaceae. *Journal of Theoretical Biology* 176(4): 531–542. DOI: 10.1006/jtbi.1995.0219.
- [19] Fahn, A. (1990): *Plant anatomy*. 4th ed. Oxford England New York: Pergamon Press: 588.
- [20] Cooper, E. S. et al. (2018): Gyroscopic stabilization minimizes drag on *Ruellia ciliatiflora* seeds. *Journal of The Royal Society Interface* 15(140): 1–7. DOI: 10.1098/rsif.2017.0901.
- [21] Allen, R. and Wardrop, A. B. (1964): The opening and shedding mechanism of the female cones of *Pinus radiata*. *Australian Journal of Botany* 12(2): 125–134. DOI: 10.1071/bt9640125.
- [22] Harlow, W. M., Côté, W. A., and Day, A. C. (1964): The opening mechanism of pine cone scales. *Journal of Forestry* 62(8): 538–540. DOI: 10.1093/jof/62.8.538.
- [23] Dawson, C., Vincent, J. F. V., and Rocca, A.-M. (1997): How pine cones open. *Nature* 390(6661): 668. DOI: 10.1038/37745.
- [24] Losada, J. M., Blanco-Moure, N., and Leslie, A. B. (2019): Not all ‘pine cones’ flex: functional trade-offs and the evolution of seed release mechanisms. *New Phytologist* 222(1): 396–407. DOI: 10.1111/nph.15563.
- [25] Reyssat, E. and Mahadevan, L. (2009): Hygromorphs: from pine cones to biomimetic bilayers. *Journal of the Royal Society Interface* 6(39): 951–957. DOI: 10.1098/rsif.2009.0184.
- [26] Martín-Sanz, R. C. et al. (2016): Disentangling plasticity of serotiny, a key adaptive trait in a Mediterranean conifer. *American Journal of Botany* 103(9): 1582–1591. DOI: 10.3732/ajb.1600199.
- [27] Lamont, B. B. et al. (1991): Canopy seed storage in woody plants. *The Botanical Review* 57(4): 277–317. DOI: 10.1007/bf02858770.
- [28] Cowling, R. M. et al. (1996): Plant diversity in mediterranean-climate regions. *Trends in Ecology & Evolution* 11(9): 362–366. DOI: 10.1016/0169-5347(96)10044-6.
- [29] Evert, R. F. and Eichhorn, S. E. (2013): *Raven Biology of plants*. New York: W.H. Freeman and Company Publishers: 727.
- [30] Kadereit, J. W. et al. (2014): *Strasburger - Lehrbuch der Pflanzenwissenschaften*. 37th ed. Berlin, Heidelberg: Springer Spektrum: 919.
- [31] Martínez-Berdeja, A., Ezcurra, E., and Sanders, A. C. (2015): Delayed seed dispersal in california deserts. *Madroño* 62(1): 21–32. DOI: 10.3120/0024-9637-62.1.21.
- [32] Rundel, P. W. et al. (2018): Fire and plant diversification in mediterranean-climate regions. *Frontiers in Plant Science* 9: 851. DOI: 10.3389/fpls.2018.00851.

- [33] Beaufait, W. R. (1960): Some effects of high temperatures on the cones and seeds of jack pine. *Forest Science* 6(3): 194–199. DOI: 10.1093/forestscience/6.3.194.
- [34] Martín-Sanz, R. C. et al. (2017): Maintenance costs of serotiny in a variably serotinous pine: The role of water supply. *PLOS ONE* 12(7). Ed. by Aravanopoulos, F. A.: e0181648. DOI: 10.1371/journal.pone.0181648.
- [35] Moya, D. et al. (2008): Anatomic basis and insulation of serotinous cones in *Pinus halepensis* Mill. *Trees* 22(4): 511–519. DOI: 10.1007/s00468-008-0211-1.
- [36] Keeley, J. E. and Zedler, P. H. (1998): Evolution of life histories in *Pinus*, in Richardson, D. M. (ed.), *Ecology and biogeography of Pinus*. Cambridge New York, NY, USA: Cambridge University Press: 219–251.
- [37] Tapias, R. et al. (2001): Canopy seed banks in mediterranean pines of south-eastern Spain: a comparison between *Pinus halepensis* Mill., *P. pinaster* Ait., *P. nigra* Arn. and *P. pinea* L. *Journal of Ecology* 89(4): 629–638.
- [38] Shtein, I., Elbaum, R., and Bar-On, B. (2016): The hygroscopic opening of sesame fruits is induced by a functionally graded pericarp architecture. *Frontiers in Plant Science* 7(1501): 1–8. DOI: 10.3389/fpls.2016.01501.
- [39] Abraham, Y. and Elbaum, R. (2013a): Hygroscopic movements in Geraniaceae: the structural variations that are responsible for coiling or bending. *New Phytologist* 199(2): 584–594. DOI: 10.1111/nph.12254.
- [40] Elbaum, R. et al. (2007): The role of wheat awns in the seed dispersal unit. *Science* 316(5826): 884–886. DOI: 10.1126/science.1140097.
- [41] Armon, S. et al. (2011): Geometry and mechanics in the opening of chiral seed pods. *Science* 333(6050): 1726–1730.
- [42] Poppinga, S. et al. (2019): A seed flying like a bullet: ballistic seed dispersal in Chinese witch-hazel (*Hamamelis mollis* OLIV., Hamamelidaceae). *Journal of The Royal Society Interface* 16(157): 20190327. DOI: 10.1098/rsif.2019.0327.
- [43] Cunha, M. P. d. et al. (2020): A soft transporter robot fueled by light. *Advancement of Science* 7(5): 1902842. DOI: 10.1002/advs.201902842.
- [44] Wang, M. et al. (2015): Sensitive humidity-driven reversible and bidirectional bending of nanocellulose thin films as bio-inspired actuation. *Advanced Materials Interfaces* 2(1500080): 1–7. DOI: 10.1002/admi.201500080.
- [45] Gladman, A. S. et al. (2016): Biomimetic 4D printing. *Nature Materials* 15: 413–418. DOI: 10.1038/nmat4544.
- [46] Bechert, S. et al. (2021): Urbach Tower: integrative structural design of a lightweight structure made of self-shaped curved cross-laminated timber. *Structures* 33: 3667–3681. DOI: 10.1016/j.istruc.2021.06.073.
- [47] Rüggeberg, M. and Burgert, I. (2015): Bio-inspired wooden actuators for large scale applications. *PLOS ONE* 10(4): 1–16. DOI: 10.1371/journal.pone.0120718.

- [48] Grönquist, P. et al. (2019): Analysis of hygroscopic self-shaping wood at large scale for curved mass timber structures. *Science Advances* 5(9): eaax1311. DOI: 10.1126/sciadv.aax1311.
- [49] Adriaens, D. (2019): Evomimetics: the biomimetic design thinking 2.0, in Lakhtakia, A., Martín-Palma, R. J., and Knez, M. (eds.), *Bioinspiration, Biomimetics, and Bioreplication IX*. SPIE Smart Structures + Nondestructive Evaluation. Denver: SPIE: 1–13. DOI: 10.1117/12.2514049.
- [50] Cardillo, M. and Pratt, R. (2013): Evolution of a hotspot genus: geographic variation in speciation and extinction rates in *Banksia* (Proteaceae). *BMC Evolutionary Biology* 13(1): 1–11. DOI: 10.1186/1471-2148-13-155.
- [51] Gill, A. M. (1976): Fire and the opening of *Banksia ornata* F. Muell. follicles. *Journal of Australian Botany* 24: 329–335.
- [52] Wardrop, A. B. (1983): The opening mechanism of follicles of some species of *Banksia*. *Australian Journal of Botany* 31: 485–500. DOI: 10.1071/BT9830485.
- [53] Cowling, R. M. and Lamont, B. B. (1985a): Variation in serotiny of three *Banksia* species along a climatic gradient. *Australian Journal of Ecology* 10(3): 345–350. DOI: 10.1111/j.1442-9993.1985.tb00895.x.
- [54] Huss, J. C. et al. (2018a): Climate-dependent heat-triggered opening mechanism of *Banksia* seed pods. *Advanced Science* 5(1700572): 1–13. DOI: 10.1002/advs.201700572.
- [55] George, A. S. (1981): The genus *Banksia* L.f. (Proteaceae). *Nuytsia* 3(3): 239–474.
- [56] Duigou, A. L. et al. (2019): Humidity responsive actuation of bioinspired hygromorph biocomposites (HBC) for adaptive structures. *Composites Part A: Applied Science and Manufacturing* 116: 36–45. DOI: 10.1016/j.compositesa.2018.10.018.
- [57] Correa, D. et al. (2020): 4D pine scale: biomimetic 4D printed autonomous scale and flap structures capable of multi-phase movement. *Philosophical Transactions of the Royal Society A: Mathematical, Physical and Engineering Sciences* 378(2167): 1–18. DOI: 10.1098/rsta.2019.0445.
- [58] Carpenter, R. J. et al. (2010): Leaf fossils of *Banksia* (Proteaceae) from New Zealand: an Australian abroad. *American Journal of Botany* 97(2): 288–297. DOI: 10.3732/ajb.0900199.
- [59] He, T., Lamont, B. L., and Downes, K. S. (2011): *Banksia* born to burn. *New Phytologist* 191(1): 184–196. DOI: 10.1111/j.1469-8137.2011.03663.x.
- [60] *Western Australian herbarium. Florabase – the Western Australian flora* (2021). <https://florabase.dpaw.wa.gov.au/>, accessed: 2021-09-12: Departement of Biodiversity, Conservation and Attractions.
- [61] George, A. S. and Gradner, C. A. (1984): *The Banksia book*. Kenthurst: Kangaroo: 240.
- [62] Wild, A. (1958): The phosphate content of Australian soils. *Australian Journal of Agricultural Research* 9(2): 193–204. DOI: 10.1071/ar9580193.

- [63] He, T. et al. (2016): Evolutionary potential and adaptation of *Banksia attenuata* (Proteaceae) to climate and fire regime in southwestern Australia, a global biodiversity hotspot. *Scientific Reports* 6(26315). DOI: 10.1038/srep26315.
- [64] Walter, H. (1968): Die gemäßigten und arktischen Zonen, in *Die Vegetation der Erde in öko-physiologischer Betrachtung*. Jena: Gustav Fischer Verlag: 1001.
- [65] Taylor, A. and Hopper, S. D. (1988): *The Banksia atlas*. Australian flora and fauna series 8. Canberra: Australian Govt. Publ. Service: 258.
- [66] Fuss, A. M. and Sedgley, M. (1990): Floral initiation and development in relation to the time of flowering in *Banksia coccinea* R.Br and *B. menziesii* R.Br (Proteaceae). *Australian Journal of Botany* 38(5): 487–500. DOI: 10.1071/bt9900487.
- [67] Stock, W. D., Pate, J. S., and Rasins, E. (1991): Seed developmental patterns in *Banksia attenuata* R. Br. and *B. laricina* C. Gardner in relation to mechanical defence costs. *New Phytologist* 117(1): 109–114. DOI: 10.1111/j.1469-8137.1991.tb00950.x.
- [68] Huss, J. C. et al. (2019): Protecting offspring against fire: lessons from *Banksia* seed pods. *Frontiers in Plant Science* 10: 283. DOI: 10.3389/fpls.2019.00283.
- [69] Huss, J. C. et al. (2018b): Temperature-induced self-sealing capability of *Banksia* follicles. *Journal of The Royal Society Interface* 15 (143): 20180190. DOI: 10.1098/rsif.2018.0190.
- [70] Groom, P. and Lamont, B. B. (2015): *Plant life of southwestern Australia. Adaptations for survival. Adaptations for Survival*. Berlin, Boston: Walter de Gruyter: 268.
- [71] Enright, N. J. and Lamont, B. B. (1989): Fire temperatures and follicle-opening requirements in 10 *Banksia* species. *Australian Journal of Ecology* 14(1): 107–113. DOI: 10.1111/j.1442-9993.1989.tb01012.x.
- [72] Cowling, R. M. and Lamont, B. B. (1985b): Seed release in *Banksia*: the role of wet-dry cycles. *Australian Journal of Ecology* 10(2): 169–171. DOI: 10.1111/j.1442-9993.1985.tb00878.x.
- [73] Huss, J. C. and Gierlinger, N. (2021): Functional packaging of seeds. *New Phytologist* 230(6): 2154–2163. DOI: 10.1111/nph.17299.
- [74] Albersheim, P. et al. (2011): *Plant cell walls – from chemistry to biology*. New York: Garland Science: 430.
- [75] Fengel, D. and Wegener, G. (1983): *Wood. Chemistry, ultrastructure, reactions*. De Gruyter: 613. DOI: 10.1515/9783110839654.
- [76] Higuchi, T. (1997): *Biochemistry and molecular biology of wood*. Berlin Heidelberg: Springer: 362. DOI: 10.1007/978-3-642-60469-0.
- [77] Jakob, H. F. et al. (1995): The elementary cellulose fibril in *Picea abies*: comparison of transmission electron microscopy, small-angle X-ray scattering, and wide-angle X-ray scattering results. *Macromolecules* 28(26): 8782–8787. DOI: 10.1021/ma00130a010.

- [78] Andersson, S. et al. (2003): Crystallinity of wood and the size of cellulose crystallites in Norway spruce (*Picea abies*). *Journal of Wood Science* 49(6): 531–537. DOI: 10.1007/s10086-003-0518-x.
- [79] Wagenführ, R. (1999): *Anatomie des Holzes. Strukturanalytik - Identifizierung - Nomenklatur - Mikrotechnologie*. 5th ed. Leinfelden-Echterdingen: 188.
- [80] Zabler, S. et al. (2010): Moisture changes in the plant cell wall force cellulose crystallites to deform. *Journal of Structural Biology* 171(2): 133–141. DOI: 10.1016/j.jsb.2010.04.013.
- [81] Fernandes, A. N. et al. (2011): Nanostructure of cellulose microfibrils in spruce wood. *Proceedings of the National Academy of Sciences* 108(47): 18863–18864. DOI: 10.1073/pnas.1108942108.
- [82] Donaldson, L. (2007): Cellulose microfibril aggregates and their size variation with cell wall type. *Wood Science and Technology* 41(5): 443. DOI: 10.1007/s00226-006-0121-6.
- [83] Lu, Y.-C., Lu, Y., and Fan, X. (2020): Structure and characteristics of lignin, in *Lignin – biosynthesis and transformation for industrial applications*. Ed. by Sharma, S. and Kumar, A. Cham: Springer: 17–75. DOI: 10.1007/978-3-030-40663-9_2.
- [84] Boerjan, W., Ralph, J., and Baucher, M. (2003): Lignin biosynthesis. *Annual Review of Plant Biology* 54(1): 519–546. DOI: 10.1146/annurev.arplant.54.031902.134938.
- [85] Ralph, J., Lapierre, C., and Boerjan, W. (2019): Lignin structure and its engineering. *Current Opinion in Biotechnology* 56: 240–249. DOI: 10.1016/j.copbio.2019.02.019.
- [86] Schuetz, M., Smith, R., and Ellis, B. (2013): Xylem tissue specification, patterning, and differentiation mechanisms. *Journal of Experimental Botany* 64(1): 11–31. DOI: 10.1093/jxb/ers287.
- [87] Chen, W.-J. et al. (2018a): Revealing the topochemistry and structural features of lignin during the growth of *Eucalyptus grandis* \times *Eucalyptus urophylla*. *ACS Sustainable Chemistry & Engineering* 6(7): 9198–9207. DOI: 10.1021/acssuschemeng.8b01542.
- [88] Thybring, E. E. et al. (2020): How much water can wood cell walls hold? A triangulation approach to determine the maximum cell wall moisture content. *PLOS ONE* 15(8). Ed. by Matsakas, L.: e0238319. DOI: 10.1371/journal.pone.0238319.
- [89] Kang, X. et al. (2019): Lignin-polysaccharide interactions in plant secondary cell walls revealed by solid-state NMR. *Nature Communications* 10(1): 1–10. DOI: 10.1038/s41467-018-08252-0.
- [90] Skaar, C. (1988): *Wood-water relations*. Berlin, Heidelberg: Springer: 283. DOI: 10.1007/978-3-642-73683-4.

- [91] Englund, E. T. et al. (2013): A critical discussion of the physics of wood–water interactions. *Wood Science and Technology* 47(1): 141–161. DOI: 10.1007/s00226-012-0514-7.
- [92] Bergander, A. and Salmén, L. (2002): Cell wall properties and their effects on the mechanical properties of fibers. *Journal of Materials Science* 37(1): 151–156. DOI: 10.1023/a:1013115925679.
- [93] Kollmann, F. (1982): *Technologie des Holzes und der Holzwerkstoffe. Erster Band: Anatomie und Pathologie, Chemie, Physik, Elastizität und Festigkeit*. 2nd ed. Berlin, Göttingen, Heidelberg: Springer: 1050.
- [94] Eder, M. et al. (2013): Experimental micromechanical characterisation of wood cell walls. *Wood Science and Technology* 47(1): 163–182. DOI: 10.1007/s00226-012-0515-6.
- [95] Salmén, L. (2018): Wood cell wall structure and organisation in relation to mechanics, in: *Plant biomechanics: from structure to function at multiple scales*. Ed. by Geitmann, A. and Gril, J. Cham: Springer: 3–19. DOI: 10.1007/978-3-319-79099-2_1.
- [96] Berglund, J. et al. (2020): Wood hemicelluloses exert distinct biomechanical contributions to cellulose fibrillar networks. *Nature Communications* 11(1). DOI: 10.1038/s41467-020-18390-z.
- [97] Horbelt, N. et al. (2021): Effects of moisture and cellulose fibril angle on the tensile properties of native single Norway spruce wood fibres. *Wood Science and Technology*. DOI: 10.1007/s00226-021-01315-4.
- [98] Sakurada, I., Nukushina, Y., and Ito, T. (1962): Experimental determination of the elastic modulus of crystalline regions in oriented polymers. *Journal of Polymer Science* 57(165): 651–660. DOI: 10.1002/pol.1962.1205716551.
- [99] Tashiro, K. and Kobayashi, M. (1991): Theoretical evaluation of three-dimensional elastic constants of native and regenerated celluloses: role of hydrogen bonds. *Polymer* 32(8): 1516–1526. DOI: 10.1016/0032-3861(91)90435-1.
- [100] Salmén, L. (2004): Micromechanical understanding of the cell-wall structure. *Comptes Rendus Biologies* 327(9-10): 873–880. DOI: 10.1016/j.crv.2004.03.010.
- [101] Cousins, W. J., Armstrong, R. W., and Robinson, W. H. (1975): Young’s modulus of lignin from a continuous indentation test. *Journal of Materials Science* 10(10): 1655–1658. DOI: 10.1007/bf00554925.
- [102] Cousins, W. J. (1976): Elastic modulus of lignin as related to moisture content. *Wood Science and Technology* 10(1): 9–17. DOI: 10.1007/bf00376380.
- [103] — (1978): Young’s modulus of hemicellulose as related to moisture content. *Wood Science and Technology* 12(3): 161–167. DOI: 10.1007/bf00372862.
- [104] Reiterer, A. et al. (1999): Experimental evidence for a mechanical function of the cellulose microfibril angle in wood cell walls. *Philosophical Magazine A* 79(9): 2173–2184. DOI: 10.1080/01418619908210415.

- [105] Chen, Q.-m. et al. (2007): Micro analytical methods for determination of compression wood content in loblolly pine. *Journal of Wood Chemistry and Technology* 27(3-4): 169–178. DOI: 10.1080/02773810701700810.
- [106] Nanayakkara, B. et al. (2009): Quantitative chemical indicators to assess the gradation of compression wood. *Holzforschung* 63(4): 431–439. DOI: 10.1515/hf.2009.062.
- [107] Zhan, T., Lyu, J., and Eder, M. (2021): In situ observation of shrinking and swelling of normal and compression Chinese fir wood at the tissue, cell and cell wall level. *Wood Science and Technology*. DOI: 10.1007/s00226-021-01321-6.
- [108] Keylwerth, R. and Noack, D. (1964): Die Kammertrocknung von Schnittholz. *Holz als Roh- und Werkstoff* 22(1): 29–36. DOI: 10.1007/bf02627726.
- [109] Xie, Y. et al. (2011): The dynamic water vapour sorption behaviour of natural fibres and kinetic analysis using the parallel exponential kinetics model. *Journal of Materials Science* 46(2): 479–489. DOI: 10.1007/s10853-010-4935-0.
- [110] Kulasinski, K. et al. (2015): Water adsorption in wood microfibril-hemicellulose system: role of the crystalline–amorphous interface. *Biomacromolecules* 16(9): 2972–2978. DOI: 10.1021/acs.biomac.5b00878.
- [111] Chen, M. et al. (2018b): Role of hydrogen bonding in hysteresis observed in sorption-induced swelling of soft nanoporous polymers. *Nature Communications* 9(1): 1–5. DOI: 10.1038/s41467-018-05897-9.
- [112] Kulasinski, K., Derome, D., and Carmeliet, J. (2017): Impact of hydration on the micromechanical properties of the polymer composite structure of wood investigated with atomistic simulations. *Journal of the Mechanics and Physics of Solids* 103: 221–235. DOI: 10.1016/j.jmps.2017.03.016.
- [113] Meylan, B. A. (1972): The influence of microfibril angle on the longitudinal shrinkage-moisture content relationship. *Wood Science and Technology* 6(4): 293–301. DOI: 10.1007/bf00357051.
- [114] Boyd, J. D. (1977): Relationship between fibre morphology and shrinkage of wood. *Wood Science and Technology* 11(1): 3–22. DOI: 10.1007/bf00353597.
- [115] Leonardon, M. et al. (2010): Wood shrinkage: influence of anatomy, cell wall architecture, chemical composition and cambial age. *European Journal of Wood and Wood Products* 68(1): 87–94. DOI: 10.1007/s00107-009-0355-8.
- [116] Derome, D. et al. (2011): Hysteretic swelling of wood at cellular scale probed by phase-contrast X-ray tomography. *Journal of Structural Biology* 173(1): 180–190. DOI: 10.1016/j.jsb.2010.08.011.
- [117] Chen, Q. et al. (2020): Hygroscopic swelling of moso bamboo cells. *Cellulose* 27(2): 611–620. DOI: 10.1007/s10570-019-02833-y.
- [118] Yamamoto, H. et al. (2001): A model of anisotropic swelling and shrinking process of wood. *Wood Science and Technology* 35(1-2): 167–181. DOI: 10.1007/s002260000074.

- [119] Fratzl, P., Elbaum, R., and Burgert, I. (2008): Cellulose fibrils direct plant organ movements. *Faraday Discussions* 139: 275–282. DOI: 10.1039/b716663j.
- [120] Brémaud, I. et al. (2013): Changes in viscoelastic vibrational properties between compression and normal wood: roles of microfibril angle and of lignin. *Holzforschung* 67(1): 75–85. DOI: 10.1515/hf-2011-0186.
- [121] Xu, P. et al. (2008): Longitudinal shrinkage behaviour of compression wood in radiata pine. *Wood Science and Technology* 43(5-6): 423–439. DOI: 10.1007/s00226-008-0228-z.
- [122] Lehringer, C., Gierlinger, N., and Koch, G. (2008): Topochemical investigation on tension wood fibres of *Acer* spp., *Fagus sylvatica* L. and *Quercus robur* L. *Holzforschung* 62 (3): 255–263.
- [123] Fromm, J., ed. (2013): *Cellular aspects of wood formation*. Berlin, Heidelberg: Springer: 260.
- [124] Abraham, Y. et al. (2018): Mapping of cell wall aromatic moieties and their effect on hygroscopic movement in the awns of stork’s bill. *Cellulose* 25(7): 3827–3841. DOI: 10.1007/s10570-018-1852-x.
- [125] Chamberlain, C. J. (1932): *Methods in plant histology*. 5th ed. Chicago: The University of Chicago Press. 416 pp.
- [126] Romeis, B. (2015): *Romeis Mikroskopische Technik*. Ed. by Mulisch, M. and Welsch, U. 19th ed. Heidelberg: Springer Spektrum: 603.
- [127] Mitra, P. P. and Loqué, D. (2014): Histochemical staining of *Arabidopsis thaliana* secondary cell wall elements. *Journal of Visualized Experiments* 87(e51381): 1–11. DOI: 10.3791/51381.
- [128] Wiesner, J. R. von (1878): Note über das Verhalten des Phloroglucins und einiger verwandter Körper zur verholzten Zellmembran, in *Sitzungsberichte der Akademie der Wissenschaften. Mathematisch-naturwissenschaftliche Classe*. 77. Wien: K. K. Hof- und Staatsdruckerei: 60–66.
- [129] Pomar, F., Merino, F., and Ros Barceló, A. (2002): O-4-Linked coniferyl and sinapyl aldehydes in lignifying cell walls are the main targets of the Wiesner (phloroglucinol-HCl) reaction. *Protoplasma* 220: 17–28. DOI: 10.1007/s00709-002-0030-y.
- [130] Vance, C. P., Kirk, T. K., and Sherwood, R. T. (1980): Lignification as a mechanism of disease resistance. *Annual Review of Phytopathology* 18(1): 259–288. DOI: 10.1146/annurev.py.18.090180.001355.
- [131] Mäule, C. (1901): Das Verhalten verholzter Membranen gegen Kaliumpermanganat, eine Holzreaktion neuer Art. Habilitation. Königl. Technische Hochschule Stuttgart: 22.
- [132] Yamashita, D. et al. (2016): Improved Mäule color reaction provides more detailed information on syringyl lignin distribution in hardwood. *Journal of Wood Science* 62(2): 131–137. DOI: 10.1007/s10086-016-1536-9.

- [133] Meshitsuka, G. and Nakano, J. (1978): Studies on the mechanism of lignin color reaction: Mäule color reaction. *Mokuzai Gakkaishi* 24(8): 563–568.
- [134] Iiyama, K. and Pant, R. (1988): The mechanism of the Mäule colour reaction introduction of methylated syringyl nuclei into softwood lignin. *Wood Science and Technology* 22(2): 167–175. DOI: 10.1007/bf00355852.
- [135] Agarwal, U. P. and Ralph, S. A. (1997): FT-Raman spectroscopy of wood: identifying contributions of lignin and carbohydrate polymers in the spectrum of black spruce (*Picea mariana*). *Applied Spectroscopy* 51(11): 1648–1655. DOI: 10.1366/0003702971939316.
- [136] Larsen, K. L. and Barsberg, S. (2010): Theoretical and Raman spectroscopic studies of phenolic lignin model monomers. *The Journal of Physical Chemistry B* 114(23): 8009–8021. DOI: 10.1021/jp1028239.
- [137] Sun, L. et al. (2011): Rapid determination of syringyl: guaiacyl ratios using FT-Raman spectroscopy. *Biotechnology and Bioengineering* 109(3): 647–656. DOI: 10.1002/bit.24348.
- [138] Gierlinger, N. (2017): New insights into plant cell walls by vibrational microspectroscopy. *Applied Spectroscopy Reviews* 53(7): 517–551. DOI: 10.1080/05704928.2017.1363052.
- [139] Nasdala, L. et al. (2004): Raman spectroscopy, in *Spectroscopic methods in mineralogy*. Mineralogical Society of Great Britain and Ireland. Chap. 7: 281–343. DOI: 10.1180/emu-notes.6.7.
- [140] Larkin, P. (2011): *Infrared and Raman spectroscopy*. Saint Louis: Elsevier: 230.
- [141] Smith, E. and Dent, G. (2019): *Modern Raman spectroscopy*. Hoboken: John Wiley & Sons: 241.
- [142] Agarwal, U. (1999): An overview of Raman spectroscopy as applied to lignocellulosic materials, in. *Advances in lignocellulosics characterization*. Ed. by Argyropoulos, D. Atlanta: TAPPI Press: 201–225.
- [143] Gierlinger, N. N., Keplinger, T. T., and Harrington, M. M. (2012): Imaging of plant cell walls by confocal Raman microscopy. *Nature Protocols* 7(9): 1694–1708. DOI: 10.1038/nprot.2012.092.
- [144] Agarwal, U. P. and Atalla, R. H. (1986): In-situ Raman microprobe studies of plant cell walls: Macromolecular organization and compositional variability in the secondary wall of *Picea mariana* (Mill.) B.S.P. *Planta* 169(3): 325–332. DOI: 10.1007/BF00392127.
- [145] Edwards, H., Farwell, D., and Webster, D. (1997): FT Raman microscopy of untreated natural plant fibres. *Spectrochimica Acta Part A: Molecular and Biomolecular Spectroscopy* 53(13): 2383–2392. DOI: 10.1016/s1386-1425(97)00178-9.
- [146] Mateu, B. P., Bock, P., and Gierlinger, N. (2020): Raman imaging of plant cell walls, in *Methods in Molecular Biology*. New York: Springer: 251–295. DOI: 10.1007/978-1-0716-0621-6_15.

- [147] Wiley, J. H. and Atalla, R. H. (1987): Band assignments in the raman spectra of celluloses. *Carbohydrate Research* 160: 113–129. DOI: 10.1016/0008-6215(87)80306-3.
- [148] Gierlinger, N. et al. (2010): Cellulose microfibril orientation of *Picea abies* and its variability at the micron-level determined by Raman imaging. *Journal of Experimental Botany* (2): 587–595.
- [149] Schroeder, H. A. (1972): Shrinking and swelling differences between hardwoods and softwoods. *Wood and Fiber Science* 4(1): 20–25.
- [150] Özparpucu, M. et al. (2017): Unravelling the impact of lignin on cell wall mechanics: a comprehensive study on young poplar trees downregulated for cinnamyl alcohol dehydrogenase (CAD). *Plant Journal* 91(3): 480–490. DOI: 10.1111/tpj.13584.
- [151] Abraham, Y. and Elbaum, R. (2013b): Quantification of microfibril angle in secondary cell walls at subcellular resolution by means of polarized light microscopy. *New Phytologist* 197(3): 1012–1019. DOI: 10.1111/nph.12070.
- [152] Oldenbourg, R. (2004): Polarization microscopy with the LC-PolScope, in Goldman, R. D. and Spector, D. L. (eds.), *Live cell imaging: a laboratory manual*. New York: Cold Spring Harbor: 205–237.
- [153] Eder, M., Lütz-Meindl, U., and Weiss, I. M. (2010): Non-invasive LC-PolScope imaging of biominerals and cell wall anisotropy changes. *Protoplasma* 246(1-4): 49–64. DOI: 10.1007/s00709-010-0124-x.
- [154] Hu, K. et al. (2017): Investigation of the multilayered structure and microfibril angle of different types of bamboo cell walls at the micro/nano level using a LC-PolScope imaging system. *Cellulose* 24(11): 4611–4625. DOI: 10.1007/s10570-017-1447-y.
- [155] Fromm, J. et al. (2003): Lignin distribution in wood cell walls determined by TEM and backscattered SEM techniques. *Journal of Structural Biology* 143(1): 77–84. DOI: 10.1016/S1047-8477(03)00119-9.
- [156] Lehringer, C., Daniel, G., and Schmitt, U. (2009): TEM/FE-SEM studies on tension wood fibres of *Acer* spp., *Fagus sylvatica* L. and *Quercus robur* L. *Wood Science and Technology* 43(7-8): 691–702.
- [157] Zollfrank, C. and Fromm, J. (2009): Ultrastructural development of the softwood cell wall during pyrolysis. *Holzforschung* 63(2): 248–253. DOI: 10.1515/HF.2009.031.
- [158] Lautner, S., Zollfrank, C., and Fromm, J. (2012): Microfibril angle distribution of poplar tension wood. *IAWA Journal* 33(4): 431–439. DOI: 10.1163/22941932-90000105.
- [159] Dykstra, M. J. and Reuss, L. E. (2003): *Biological electron microscopy. Theory, techniques, and troubleshooting*. 2nd ed. Boston: Springer: 534. DOI: 10.1007/978-1-4419-9244-4_13.
- [160] Kohl, H. and Reimer, L. (2008): *Transmission electron microscopy. Physics of Image Formation*. 5th ed. Berlin, Heidelberg: Springer: 587. DOI: 10.1007/978-3-662-21556-2_3.

- [161] Williams, D. B. and Carter, C. B. (2009): *Transmission electron microscopy. A textbook for materials science*. 2nd ed. New York: Springer: 760.
- [162] Geyer, G. (1973): *Ultrahistochemie. Histochemische Arbeitsvorschriften für die Elektronenmikroskopie*. 2nd ed. Stuttgart: Fischer: 478.
- [163] Hayat, M. A. (1981): *Fixation for electron microscopy*. New York: Academic Press: 501.
- [164] — (2000): *Principles and techniques of electron microscopy. Biological Applications*. 4th ed. Cambridge: Cambridge University Press: 543.
- [165] Bland, D. E., Foster, R. C., and Logan, A. F. (1971): The mechanism of permanganate and osmium tetroxide fixation and the distribution of lignin in the cell wall of *Pinus radiata*. *Holzforschung* 25(5): 137–143.
- [166] Donaldson, L. A. (1992): Lignin distribution during latewood formation in *Pinus radiata* D. Don. *IAWA Journal* 13(4): 381–387. DOI: 10.1163/22941932-90001291.
- [167] Kleist, G. and Schmitt, U. (1999): Evidence of accessory compounds in vessel walls of sapelli heartwood (*Entandrophragma cylindricum*) obtained by transmission electron microscopy. *Holz als Roh- und Werkstoff* 57(2): 93–95. DOI: 10.1007/PL00002633.
- [168] Lawn, A. M. (1960): The use of potassium permanganate as an electron-dense stain for sections of tissue embedded in epoxy resin. *The Journal of Cell Biology* 7(1): 197–198.
- [169] Maurer, A. and Fengel, D. (1990): A new process for improving the quality and lignin staining of ultrathin sections from wood tissue. *Holzforschung* 44 (6): 453–460.
- [170] Carter, C. B. and Williams, D. B. (2016): *Transmission electron microscopy. Diffraction, imaging, and spectrometry*. Berlin, Heidelberg: Springer: 518. DOI: 10.1007/978-3-319-26651-0.
- [171] Niemz, P. (1993): *Physik des Holzes und der Holzwerkstoffe*. Leinfelden-Echterdingen: DRW-Verlag: 243.
- [172] Perré, P. and Huber, F. (2007): Measurement of free shrinkage at the tissue level using an optical microscope with an immersion objective: results obtained for douglas fir (*Pseudotsuga menziesii*) and spruce (*Picea abies*). *Annals of Forest Science* 64(3): 255–265. DOI: 10.1051/forest:2007003.
- [173] Mittemeijer, E. J. (2011): *Fundamentals of materials science*. Berlin, Heidelberg: Springer: 594. DOI: 10.1007/978-3-642-10500-5.
- [174] Bolton, W. and Higgins, R. A. (2021): *Materials for engineers and technicians*. 7th ed. London, New York: Routledge: 439.
- [175] Masic, A. et al. (2015): Osmotic pressure induced tensile forces in tendon collagen. *Nature Communications* 6(1): 1–8. DOI: 10.1038/ncomms6942.

- [176] Bertinetti, L. et al. (2015a): Osmotically driven tensile stress in collagen-based mineralized tissues. *Journal of the Mechanical Behavior of Biomedical Materials* 52: 14–21. DOI: 10.1016/j.jmbbm.2015.03.010.
- [177] Jajcinovic, M. et al. (2018): Influence of relative humidity on the strength of hardwood and softwood pulp fibres and fibre to fibre joints. *Cellulose* 25(4): 2681–2690. DOI: 10.1007/s10570-018-1720-8.
- [178] Burgert, I. et al. (2002): A comparison of two techniques for wood fibre isolation – evaluation by tensile tests on single fibres with different microfibril angle. *Plant Biology* 4(1): 9–12. DOI: 10.1055/s-2002-20430.
- [179] Burgert, I. et al. (2003): Microtensile testing of wood fibers combined with video extensometry for efficient strain detection. *Holzforschung* 57(6): 661–664. DOI: 10.1515/HF.2003.099.
- [180] Fischer, W. J. et al. (2012): Testing of individual fiber-fiber joints under biaxial load and simultaneous analysis of deformation. *Nordic Pulp & Paper Research Journal* 27(2): 237–244. DOI: 10.3183/npprj-2012-27-02-p237-244.
- [181] Sedighi-Gilani, M. and Navi, P. (2007): Experimental observations and micromechanical modeling of successive-damaging phenomenon in wood cells’ tensile behavior. *Wood Science and Technology* 41(1): 69–85. DOI: 10.1007/s00226-006-0094-5.
- [182] Wang, G. et al. (2011): Microtension test method for measuring tensile properties of individual cellulosic fibers. *Wood and Fiber Science* 43(3): 251–261.
- [183] Yu, Y. et al. (2011a): An improved microtensile technique for mechanical characterization of short plant fibers: a case study on bamboo fibers. *Journal of Materials Science* 46(3): 739–746. DOI: 10.1007/s10853-010-4806-8.
- [184] Ye, X. et al. (2019): Tensile properties of individual multicellular *Bacillus subtilis* fibers. *Science China Physics, Mechanics & Astronomy* 62(994611). DOI: 10.1007/s11433-019-9393-x.
- [185] Ye, X. et al. (2017): A multiscale material testing system for in situ optical and electron microscopes and its application. *Sensors* 17(8): 1800. DOI: 10.3390/s17081800.
- [186] Ajantiwalay, T. et al. (2020): Towards bridging the experimental length-scale gap for tensile tests on structural materials: lessons learned from an initial assessment of microtensile tests and the path forward. *JOM* 72(1): 113–122. DOI: 10.1007/s11837-019-03897-8.
- [187] Wimmer, R. et al. (1997): Longitudinal hardness and Young’s modulus of spruce tracheid secondary walls using nanoindentation technique. *Wood Science and Technology* 31(2): 131–141. DOI: 10.1007/BF00705928.
- [188] Fischer-Cripps, A. C. (2011): *Nanoindentation*. 3rd ed. New York: Springer: 279.
- [189] Oliver, W. C. and Pharr, G. M. (1992): An improved technique for determining hardness and elastic modulus using load and displacement sensing indentation experiments. *Journal of Materials Research* 7(6): 1564–1583. DOI: 10.1557/JMR.1992.1564.

- [190] Bertinetti, L. et al. (2015b): Characterizing moisture-dependent mechanical properties of organic materials: humidity-controlled static and dynamic nanoindentation of wood cell walls. *Philosophical Magazine* 95(16-18): 1992–1998. DOI: 10.1080/14786435.2014.920544.
- [191] Gindl, W., Gupta, H. S., and Grünwald, C. (2002): Lignification of spruce tracheid secondary cell walls related to longitudinal hardness and modulus of elasticity using nano-indentation. *Canadian Journal of Botany* 80(10): 1029–1033. DOI: 10.1139/b02-091.
- [192] Gindl, W. et al. (2004): Mechanical properties of spruce wood cell walls by nanoindentation. *Applied Physics A* 79(8): 2069–2073. DOI: 10.1007/s00339-004-2864-y.
- [193] Spurr, A. R. (1969): A low-viscosity epoxy resin embedding medium for electron microscopy. *Journal of Ultrastructure Research* 26(1): 31–43. DOI: 10.1016/S0022-5320(69)90033-1.
- [194] Orwoll, R. A. and Arnold, P. A. (2007): Polymer–solvent interaction parameter χ , in *Physical properties of polymers handbook*. New York: Springer: 233–257. DOI: 10.1007/978-0-387-69002-5_14.
- [195] Rosato, D. V., Mattia, D. P. D., and Rosato, D. V. (1991): The structure and basic properties of plastics, in *Designing with plastics and composites: a handbook*. Boston: Springer: 61–123. DOI: 10.1007/978-1-4615-9723-0_2.
- [196] Weichert, L. (1963): Untersuchungen über das Sorption- und Quellungsverhalten von Fichte, Buche und Buchen-Preßvollholz bei Temperaturen zwischen 20° und 100°C. *Holz als Roh- und Werkstoff* 21(8): 290–300. DOI: 10.1007/bf02610962.
- [197] *Climate statistics for Australian locations – summary statistics Eneabba* (2021). http://www.bom.gov.au/climate/averages/tables/cw_008225.shtml, accessed: 2021-08-12: Australian Government, Bureau of Meteorology.
- [198] Burgert, I. et al. (2007): Tensile and compressive stresses in tracheids are induced by swelling based on geometrical constraints of the wood cell. *Planta* 226(4): 981–987. DOI: 10.1007/s00425-007-0544-9.
- [199] Eder, M., Stanzl-Tschegg, S., and Burgert, I. (2008): The fracture behaviour of single wood fibres is governed by geometrical constraints: in situ ESEM studies on three fibre types. *Wood Science and Technology* 42(8): 679–689. DOI: 10.1007/s00226-008-0214-5.
- [200] Olsson, A.-M. et al. (2007): Mechano-sorptive creep in wood fibres. *Wood Science and Technology* 41(1): 59–67. DOI: 10.1007/s00226-006-0086-5.
- [201] Keckes, J. et al. (2003): Cell-wall recovery after irreversible deformation of wood. *Nature Materials* 2(12): 810–813. DOI: 10.1038/nmat1019.
- [202] Takahashi, C. et al. (2004): The creep of wood destabilized by change in moisture content. Part 1: The creep behaviors of wood during and immediately after drying. *Holzforschung* 58(3): 261–267. DOI: 10.1515/hf.2004.040.

- [203] Takahashi, C. et al. (2005): The creep of wood destabilized by change in moisture content. Part 2: The creep behaviors of wood during and immediately after adsorption. *Holzforschung* 59(1): 46–53. DOI: 10.1515/hf.2005.008.
- [204] Kojima, Y. and Yamamoto, H. (2004): Effect of microfibril angle on the longitudinal tensile creep behavior of wood. *Journal of Wood Science* 50(4): 301–306. DOI: 10.1007/s10086-003-0565-3.
- [205] Kojima, Y. and Yamamoto, H. (2005): Effect of moisture content on the longitudinal tensile creep behavior of wood. *Journal of Wood Science* 51(5): 462–467. DOI: 10.1007/s10086-004-0676-5.
- [206] Englund, E. T. and Salmén, L. (2012): Tensile creep and recovery of Norway spruce influenced by temperature and moisture. *Holzforschung* 66(8): 959–965. DOI: 10.1515/hf-2011-0172.
- [207] Timoshenko, S. (1925): Analysis of bi-metal thermostats. *Journal of the Optical Society of America* 11(3): 233–255. DOI: 10.1364/josa.11.000233.
- [208] Agarwal, U. and Terashima, N. (2003): FT-Raman study of dehydrogenation polymer (DHP) lignins, in *Proceedings*. 12th ISWPC International symposium on wood and pulping chemistry. University of Wisconsin-Madison, Dept. of Forest Ecology and Management. Madison, WI: 123–126.
- [209] Fratzl, P., Burgert, I., and Gupta, H. S. (2004): On the role of interface polymers for the mechanics of natural polymeric composites. *Physical Chemistry Chemical Physics* 6(24): 5575–5579. DOI: 10.1039/b411986j.
- [210] Rüggeberg, M. et al. (2008): Stiffness gradients in vascular bundles of the palm *Washingtonia robusta*. *Proceedings of the Royal Society B* 275(1648): 2221–2229. DOI: 10.1098/rspb.2008.0531.
- [211] Baehr, H. D. (2005): *Thermodynamik. Grundlagen und technische Anwendungen*. Berlin, Heidelberg: Springer: 651. DOI: 10.1007/b138786.
- [212] Pidgeon, L. M. and Maass, O. (1930): The adsorption of water by wood. *Journal of the American Chemical Society* 52(3): 1053–1069. DOI: 10.1021/ja01366a033.
- [213] Hawley, L. F. (1931): *Wood-liquid relations*. Technical bulletin 248. US Departement of Agriculture: 1–35.
- [214] Christensen, G. N. and Kelsey, K. E. (1959): Die Geschwindigkeit der Wasserdampfsorption durch Holz. *Holz als Roh- und Werkstoff* 17(5): 178–188. DOI: 10.1007/bf02608810.
- [215] Murata, K. and Masuda, M. (2006): Microscopic observation of transverse swelling of latewood tracheid: effect of macroscopic/mesoscopic structure. *Journal of Wood Science* 52(4): 283–289. DOI: 10.1007/s10086-005-0760-5.
- [216] Patera, A. et al. (2017): Swelling interactions of earlywood and latewood across a growth ring: global and local deformations. *Wood Science and Technology* 52(1): 91–114. DOI: 10.1007/s00226-017-0960-3.

- [217] Özparpucu, M. et al. (2018): The effect of altered lignin composition on mechanical properties of cinnamyl alcohol dehydrogenase (CAD) deficient poplars. *Planta* 247(4): 887–897. DOI: 10.1007/s00425-017-2828-z.
- [218] Onck, P. R., Andrews, E. W., and Gibson, L. J. (2001): Size effects in ductile cellular solids. Part I: modeling. *International Journal of Mechanical Sciences* 43(3): 681–699. DOI: 10.1016/S0020-7403(00)00042-4.
- [219] Wang, H. et al. (2017): The combined effects of initial microfibrillar angle and moisture contents on the tensile mechanical properties and angle alteration of wood foils during tension. *Holzforschung* 71(6): 491–497. DOI: 10.1515/hf-2016-0138.
- [220] Bjurhager, I. et al. (2010): Ultrastructure and mechanical properties of populus wood with reduced lignin content caused by transgenic down-regulation of cinnamate 4-hydroxylase. *Biomacromolecules* 11(9): 2359–2365. DOI: 10.1021/bm100487e.
- [221] Jäger, A. et al. (2011a): The relation between indentation modulus, microfibril angle, and elastic properties of wood cell walls. *Composites Part A: Applied Science and Manufacturing* 42(6): 677–685. DOI: 10.1016/j.compositesa.2011.02.007.
- [222] Tze, W. T. Y. et al. (2007): Nanoindentation of wood cell walls: continuous stiffness and hardness measurements. *Composites Part A: Applied Science and Manufacturing* 38(3): 945–953. DOI: 10.1016/j.compositesa.2006.06.018.
- [223] Jäger, A. et al. (2011b): Identification of stiffness tensor components of wood cell walls by means of nanoindentation. *Composites Part A: Applied Science and Manufacturing* 42(12): 2101–2109. DOI: 10.1016/j.compositesa.2011.09.020.
- [224] Konnerth, J. et al. (2010): Macro- and micro-mechanical properties of red oak wood (*Quercus rubra* L.) treated with hemicellulases. *Holzforschung* 64(4): 447–453. DOI: 10.1515/hf.2010.056.
- [225] Brandt, B. et al. (2010): Micromechanics and ultrastructure of pyrolysed softwood cell walls. *Acta Biomaterialia* 6(11): 4345–4351. DOI: 10.1016/j.actbio.2010.05.026.
- [226] Yu, Y. et al. (2011b): Longitudinal mechanical properties of cell wall of Masson pine (*Pinus massoniana* Lamb) as related to moisture content: a nanoindentation study. *Holzforschung* 65(1): 121–126. DOI: 10.1515/hf.2011.014.
- [227] Gorshkova, T. et al. (2018): Plant ‘muscles’: fibers with a tertiary cell wall. *New Phytologist* 218(1): 66–72. DOI: 10.1111/nph.14997.
- [228] Fang, C.-H. et al. (2008): Growth stresses are highly controlled by the amount of G-layer in poplar tension wood. *IAWA Journal* 29(3): 237–246. DOI: 10.1163/22941932-90000183.
- [229] Clair, B. et al. (2011): Maturation stress generation in poplar tension wood studied by synchrotron radiation microdiffraction. *Plant Physiology* 155(1): 562–570. DOI: 10.1104/pp.110.167270.

- [230] Alm  ras, T. et al. (2020): Evidence and quantitative evaluation of tensile maturation strain in flax phloem through longitudinal splitting. *Botany* 98(1): 9–19. DOI: 10.1139/cjb-2019-0021.
- [231] Ibragimova, N. et al. (2020): Rearrangement of the cellulose-enriched cell wall in flax phloem fibers over the course of the gravitropic reaction. *International Journal of Molecular Sciences* 21(15): 5322. DOI: 10.3390/ijms21155322.
- [232] Mikshina, P. et al. (2013): Cellulosic fibers: role of matrix polysaccharides in structure and function, in *Cellulose - fundamental aspects*. InTech: 91–112. DOI: 10.5772/51941.
- [233] Suchy, M. et al. (2010): Impact of drying on wood ultrastructure observed by deuterium exchange and photoacoustic FT-IR spectroscopy. *Biomacromolecules* 11(2): 515–520. DOI: 10.1021/bm901268j.
- [234] Thybring, E. E., Thygesen, L. G., and Burgert, I. (2017): Hydroxyl accessibility in wood cell walls as affected by drying and re-wetting procedures. *Cellulose* 24(6): 2375–2384. DOI: 10.1007/s10570-017-1278-x.
- [235] Murr, L. E. (2015): *Handbook of materials structures, properties, processing and performance*. Cham, Heidelberg, New York, Dordrecht, London: Springer: 1152. DOI: 10.1007/978-3-319-01815-7_49.
- [236] Cohen, Y. H. and Reich, Y. (2017): *Biomimetic design method for innovation and sustainability*. Cham: Springer: 258. DOI: 10.1007/978-3-319-33997-9_3.
- [237] Nachtigall, W. and Wisser, A. (2015): *Bionics by examples*. Cham, Heidelberg, New York, Dordrecht, London: Springer: 325. DOI: 10.1007/978-3-319-05858-0_14.

Figures

1	Specifics of <i>Banksia attenuata</i> R.Br.	5
2	Reproduction system of <i>B. attenuata</i>	6
3	Structural formulae of the lignin building blocks.	8
4	Structure of lignified cells	9
5	Alignment and fiber bundle directionality of a follicle	11
6	Anatomy of <i>B. attenuata</i> follicles	12
7	Evaluation of the Raman results	19
8	Determination of the hygrothermal deformation	22
9	Tensile test sample and experimental background	23
10	Nanoindentation sample and experimental background	24
11	Sample holder for hygro-tensile-cycles	27
12	Force offset at the end of the experiment.	28
13	Schematic circuit diagram of the conditioned tensile setup	30
14	Humidity-tensile-cycles of a single outer mesocarp fiber	32
15	Creep experiment of <i>Picea abies</i> branch compression wood fibers . . .	37
16	Creep experiment of <i>P. abies</i> stem compression wood fibers	38
17	Creep experiment of <i>P. abies</i> normal wood fibers, final loading	39
18	Compositional changes within <i>B. attenuata</i> mesocarp	42
19	Ultrastructure of <i>B. attenuata</i> mesocarp fibers	45
20	Hygroscopic deformation of <i>B. attenuata</i> pericarp tissue	47
21	Deformation of <i>B. attenuata</i> pericarp tissue upon heating	49
22	Tensile stiffness of the <i>B. attenuata</i> pericarp layers	52
23	Indentation properties of <i>B. attenuata</i> mesocarp and endocarp	54
24	Stress generation and strain recovery of <i>B. attenuata</i> mesocarp fibers	59
25	Stress-strain dependency of <i>B. attenuata</i> outer mesocarp	60
26	Calculated curvatures and natural sample	62

Tables

1 Raman peak intensities of *B. attenuata* (site 2) mesocarp 43

2 Hygroscopic deformation of the *B. attenuata* (site 1) pericarp layers . 50

3 Hygroscopic deformation of the *B. attenuata* (site 5) pericarp layers . 51

4 Tensile stiffness of the *B. attenuata* (site 2) pericarp layers 53

5 Nanoindentation results of the *B. attenuata* (site 2) pericarp layers . 58

6 Hygroscopic deformation and stress generation of outer mesocarp . . 61

Equations

1 Curvature proportion of a bi-metal strip [207] 40

2 Curvature proportion of a *Banksia* pericarp valve 40